A theoretical study of the effect of electron delocalization on electron transfer reactions in small organic molecules

by

Stefan Lambert Koning

submitted in fulfilment of the requirements for the degree

Master of Science

Supervisor: Doctor Jurgens Hendrik de Lange

Chemistry Department
Faculty of Natural & Agricultural Sciences
University of Pretoria
8 January 2022

© University of Pretoria

Declaration

I hereby declare that the work contained within this thesis is my own. It is being submitted for the degree Master of Science (Chemistry) at the University of Pretoria, and has not been submitted before for any degree or examination at any other institution.

Date: 2022-01-08

© University of Pretoria

Summary

The ionization potential and electron attachment energy are fundamental properties of molecules and is core to a range of physical processes such as those in photovoltaics, electrochemistry, spectroscopy, etc. Ionization energies are therefore properties worthwhile to have delicate control over for the purpose of finetuning molecules for specific goals. Here we have brought it to light that there are relationships between ionization energies and electron populations of small organic electron donors and acceptors. Electron population data was gathered with FALDI. For the electron donors Ph-XR_2, where X = N or P and R = H, Me, Et or Pr, it was found that as the delocalization between phenyl and substituted group increases, the ionization potential decreases (electron removal becomes easier). For the acceptors Ph-RNO, where R = none, CH_2, C_2H_4, or C_2H_2, as delocalization between phenyl and substituent increases electron attachment energy decreases further (electron attachment became more spontaneous). Furthermore, for these acceptor molecules, as phenyl ring electron population increases, electron attachment becomes less spontaneous. For acceptor molecules Ph-X, where X = F, Cl or Br, as the phenyl electron population increased, electron attachment became easier. All these relationships were near perfectly linear. This is the first time, to our knowledge, that such a link is found between ionization energies and electron populations. Also, physical phenomena such as conjugation, hyperconjugation, lone-pair electron resonance and Bent's rule could be recovered and quantified with FALDI. Lastly, four donor-acceptor interfaces were built from donors Ph-NH_2 and Ph-NPr_2 and from acceptors Ph-NO and Ph-C_2H_4NO, to simulate the heterojunction in an organic photovoltaics. Marcus theory was implemented to successfully calculate forward (in presence and absence of light) and reverse charge transfer rates which are some of the factors that influence the efficiency of a solar cell. The quickest rate was two orders of magnitude faster than second best at 8.40E+13 e^-/s for interface [Ph-NH_2–Ph-C_2H_4NO]. The rates were decomposed into the coupling potential and thermodynamic driving force to find the origin of such a vast difference. This revealed that a greater transition dipole moment (on which the coupling potential is dependent) of the electronic transition caused this interface to completely excel in charge transfer relative to the others. FALDI analyses were performed on the interfaces to attempt to complete the chain between the chemistry of the molecules and the rate constants – in this case transition moment, therefore. There is good indication that the transition moment is linked to the FALDI terms, suggesting that all information about the transition moment is contained in them. FALDI therefore shows great potential for a new way of calculating the transition moment.

© University of Pretoria

Outputs of this project

1. Article to be published with title "A theoretical framework to study the relationship between electron delocalization and ionization potential in organic electron donors". In this thesis it is contained in Chapter 3.
2. Potentially publishable work on the electron attachment energy of small organic donors and their electronic structure – Chapter 4.
3. Potentially publishable work on the rate of electron transfer in a donor-acceptor interface – Chapter 5.
4. Python program that aligns two randomly oriented molecules parallel to each other, based on user selected molecular planes and specified separation distance. The coordinates used as input can be obtained from *.com* files or *.log* files and the output is easily converted to a usable Gaussian input file.
5. Python program that calculates the change in Coulombic energy (ΔE_{col}) between two molecules using initial and final coordinates and atomic charges as input.

© University of Pretoria

Table of Contents Page

Chapter 1. Introduction 1

Overview of Organic Solar Cells 1
Electron transfer rates 4
Quantum chemical modelling 6
Aims and objectives 8
Thesis Outline 8
References 8

Chapter 2. Theoretical Background 10

Introduction 10
An overview of Density Functional Theory 10
Solving the Schrödinger Equation 10
Electron Density and Electron Correlation 12
Principles of Density Functional Theory 14
TD-DFT 17
Basis Sets 17
An overview of the FALDI density decomposition scheme 18
DAFH Density Decomposition 18
FALDI Density Decomposition 20
Exclusively Localized FALDI distributions 22
Marcus Theory 24
References 32

Chapter 3. A theoretical framework to study the relationship between electron delocalization and ionization potential in organic electron donors 34

Abstract 34
Introduction 34
Theoretical Background 37
Computational Methods 40
Results and Discussion 40
Fragmentation Scheme 41
Ionization Potentials 41
IP vs Interfragment *deloc*-ED 43
Analysis of (de)localization patterns in Ph-NR_2 46
Analysis of Ground state (de)localization patterns in Ph-XR_2 49
Ionization Analysis 51
Conclusion 53
Acknowledgements 55
Conflict of Interest 55
References 55

© University of Pretoria

Chapter 4. Electron density, delocalization, and electron attachment of organic electron acceptors 59

Introduction 59
Computational Methods 62
Results and Discussion 62
Fragmentation Scheme 63
Electron Affinities 64
EA vs Interfragment *deloc*-ED 65
Analysis of Ground State (de)localization patterns in Ph-X 67
Analysis of Ground State (de)localization patterns in Ph-RNO 68
Phenyl electron population vs Electron affinity and Ionization Analysis 72
Conclusion 77
References 78

Chapter 5. Tuneability of theoretically predicted charge-separation rate constants in organic solar cell interfaces 81

Introduction 81
Theoretical Background 82
Computational Methods 85
Strategy for calculating electron transfer rate constants 86
Results and Discussion 89
Decomposition of the Driving force 97
Rate constant vs IP and EA 98
ED comparison of individual and interface moieties 100
Conclusion and discussion 100
References 102

Chapter 6. Conclusions 104

References 109

Supplementary Information 110

© University of Pretoria

List of Figures

Page

Chapter 2. Theoretical Background

Figure 2.1. The rate constant as a function of both the reorganization energy as well as the change in Gibbs free energy. 26

Figure 2.2. Potential energy wells for neutral and non-excited state, neutral donor excited state and the cationic donor anionic acceptor charge separated state. Parameters used in the Marcus equation are visually illustrated here. 28

Figure 2.3. Example of how two molecules are aligned by the algorithm. 30

Figure 2.4. Hypothetical case of charge transfer. 31

Chapter 3. A theoretical framework to study the relationship between electron delocalization and ionization potential in organic electron donors

Scheme 3.1. Small organic electron donors utilized, with fragmentation schemes indicated. 41

Figure 3.1. Isosurfaces of the interfragment *deloc*–ED distributions of the GS and the change thereof upon ionization. 43

Figure 3.2. IP vs interfragment deloc–ED for the GS and cationic state of Ph-NR2. 44

Figure 3.3. IP vs interfragment deloc-ED for the GS and cationic state of Ph-PR2. 44

Chapter 4. A theoretical framework to study the tuneability of electron density and delocalization in organic electron acceptors

Scheme 4.1. Small organic electron acceptors utilized, with fragmentation schemes indicated. 63

© University of Pretoria

Figure 4.1. Isosurfaces of the interfragment deloc-ED of the GS and the change thereof upon ionization. 65

Figure 4.2. EA vs interfragment deloc–ED for the GS and anionic state of Ph-X. 66

Figure 4.3. EA vs interfragment deloc–ED for the GS and anionic state of Ph-RNO. 66

Figure 4.4. EA vs Total electron count on Ph for the GS and anionic state of Ph-X. 74

Figure 4.5. EA vs Total electron count on Ph for the GS and anionic state of Ph-RNO. 74

Chapter 5. Tuneability of theoretically predicted charge-separation rate constants in organic solar cell interfaces

Figure 5.1. The rate constant as a function of both the reorganization energy as well as the change in Gibbs free energy. 83

Figure 5.2. Potential energy wells for neutral and non-excited state, neutral donor excited state and the cationic donor anionic acceptor charge separated state. Parameters used in the Marcus equation are visually illustrated here. 84

Figure 5.3. Interface [NH2-NO] donor excited state (ES3) and CT state (ES2). 87

Figure 5.4. Ph-NH2 and Ph-NO individual and interface MOs corresponding to ESs in Figure 5.3. 88

Figure 5.5. FALDI fragmentation scheme used 89

Figure 5.6. Interface geometries. ES-opt geometries used for donors and GS-opt for acceptors. 90

Figure 5.7. Change of ED due to charge transfer. (A justification for combining ΔLI(D) & ΔLI(A) and ΔDI(D,D) & ΔDI(A,A) in the same isosurfaces is provided in the SI – see Figure S5.1). 93

© University of Pretoria

Figure 5.8. ED change upon charge transfer for [D *-A] interfaces. 94

Figure 5.9. Rate constant of interfaces (a) and (b) as a function of IP_D and EA_A. Arrows indicate actual rates for the actual IPD and EAA; 4.27E+11 e-/s and 8.40E+13 e-/s for interfaces (a) and (b), respectively. 99

List of Tables

Page

Chapter 3. A theoretical framework to study the relationship between electron delocalization and ionization potential in organic electron donors

Table 3.1. Calculated IPs and some experimental IPs of the model-molecules. 41

Table 3.2. Electron population per fragment for Ph-NR2 molecules. 45

Table 3.3. Inter-fragment delocalized density for Ph-NR2 molecules. 47

Table 3.4. Electron population change from X = N to P for Ph-XR2 molecules. 50

Table 3.5. Inter-fragment delocalized density change from X = N to P for Ph-XR2 molecules. 51

Table 3.6. Change in ED on the indicated fragment ($\Delta_{ion}N(\mathcal{F})$) when an electron is removed from the molecule (static geometry). 52

Table 3.7. Inter-fragment delocalized density change upon ionization for Ph-XR_2 molecules. 53

Chapter 4. A theoretical framework to study the tuneability of electron density and delocalization in organic electron acceptors

Table 4.1. Calculated EAs of the small organic acceptors. 64

Table 4.2. Electron population per fragment for Ph-X molecules in ground state. 67

Table 4.3. Electron population per fragment for Ph-RNO molecules in ground state. 70

Table 4.4. Inter-fragment delocalized density for Ph-RNO molecules in ground state. 71

Table 4.5. Electron population change upon electron attachment for Ph-X molecules. 75

© University of Pretoria

Table 4.6. Electron population change upon electron attachment for Ph-RNO molecules 76

Table 4.7. Inter-fragment delocalized density change upon electron attachment for Ph-RNO molecules 76

Chapter 5. Tuneability of theoretically predicted charge-separation rate constants in organic solar cell interfaces

Table 5.1. Charge separation (k_{CS}, k_{CS}*) and recombination (k_{CR}) rate constants. 90

Table 5.2. Decomposed [$\mathcal{D}$ *-$\mathcal{A}$] charge transfer rate constants. 91

Table 5.3. [$\mathcal{D}$*-$\mathcal{A}$] ED change upon charge transfer – FALDI results. 92

Table 5.4. Scaling the rate constants with actual number of electrons transferred. 92

Table 5.5. Decomposition of coupling potential 96

Table 5.6. Decomposition of Driving Force 97

Table 5.7. Analysis of the inverted region of interface (a) 98

© University of Pretoria

List of Abbreviations

IP	ionization potential
EA	electron affinity or electron attachment energy (used interchangeably)
GS-opt	ground state optimized
ES-opt	excited state optimized (usually most relevant excited state)
cat-opt	cationic state optimized
an-opt	anionic state optimized
DI	delocalization index
LI	localized index
PCE	power conversion efficiency
PSC	polymer solar cell
OSC	organic solar cell
PV	photovoltaic
BHJ	bulk heterojunction
HOMO	highest occupied molecular orbital
LUMO	lowest unoccupied molecular orbital
QTAIM	quantum theory of atoms in molecules
FALDI	fragment, atomic, localized, delocalized and interatomic
DFT	density functional theory
TD-DFT	time dependent density functional theory
SPC	single point calculation
CT	charge transfer
GS	ground state
ES	excited state

© University of Pretoria

Ph	phenyl
$\mathcal{D}$	electron donor moiety
$\mathcal{A}$	electron acceptor moiety
[$\mathcal{D}$*-$\mathcal{A}$]	excited donor-acceptor interface
ED	electron density
$\mathcal{F}_1$	fragment one (context dependent)
QCT	quantum chemical topology

© University of Pretoria

Chapter 1 – Introduction

With fossil fuels being a finite resource and impacting environments across the globe, utilizing alternative energy sources on a large scale is inevitable. There are multiple sources of energy independent on fossil fuels. Some of these are nuclear power, wind power, solar energy, hydro power, etc. Each of these has its own advantages and disadvantages, therefore each has its own role to play in the global fossil-fuel-independency effort. Thus, each of these technologies deserves to be developed and optimized to its fullest.

In this work we investigate predictive tools for development in solar energy technology, specifically organic solar cells. Recently, a lot of attention was given to non-fullerene organic solar cells (OSCs).[1] Organic semiconductors have several advantages such as being flexible, low-cost, easy to manufacture, light weight[2] and can be more environmentally friendly.[3] These are important characteristics to consider, however, the efficiencies of OSCs are not yet at the acceptable level to allow these to be a reasonable choice over those with higher power conversion efficiencies (PCEs). Organic solar cell efficiencies range around the 20 % mark[4] while Si (crystalline) and GaAs (thin film) ranges up to 25.6 % and 28.8 % efficient, respectively.[3] Clearly, OSCs are still lacking behind.

However, an ever-greater PCE should not be the sole purpose of the pursuit of better photovoltaic (PV) devices. It should not be neglected that cheap, manufacturable through low energy input and highly stable devices should also be of high priority. The ultimate goal remains for the technology to be commercially viable[1] as well as reduce energy demand of society (although academic curiosity could be a viable driving force as well).

The energy economics of a solar cell is therefore important – the energy required to produce the solar cell should be greatly compensated for by the energy it will capture throughout its lifetime.[2] In the manufacturing process of silicon based solar cells, silicon ore are melted at temperatures exceeding 1400 ºC to create the silicon wafers. Its manufacturing process therefore requires a tremendous amount of energy which is harvested from fossil fuels in most cases. The solar cell produced by this process will therefore only be energy neutral when the energy required to manufacture it is recaptured by the solar cell over its lifetime. This is but one example of how green energy solutions are not always as environmentally friendly as advertised. With respect to photovoltaics, the solution to the global energy problem is therefore not as simple as producing the most efficient solar cell. Each kind of solar cell technology should, ideally, be fully explored to find the solution that is optimal in each aspect of viability

© University of Pretoria

to fit our needs. In this work our aim is towards making progress in knowledge in the field of the less efficient organic solar cells.

Overview of organic solar cells

An OSC, usually made up of an electron donor and acceptor material, functions by the absorption of a solar photon by the light harvesting component, causing an electron-hole pair (exciton) to form (either or both the donor or acceptor moiety can be light harvesting[5]). The exciton migrates through the bulk of the organic material towards the donor-acceptor interface where charge dissociation occurs – this is the separation of the electron and its hole. Within their lifetime these created charges need to be transported away from the interface to their respective electrodes, which often requires some driving force[2]. When collected at the electrodes it can be used in a circuit.

Organic molecules can be implemented through a bilayer heterojunction or bulk heterojunction. In the former the donor and acceptor phase is distinctly separated whereas in the latter the phases are blended. When blended the donor acceptor contact surface area is immensely increases compared to a bilayer heterojunction. This creates more surface area for charge transfer but also shortens the average distance the exciton needs to migrate, reducing the chance of it relaxing and being lost. Hence, bulk heterojunction (BHJ) solar cells have shown to be significantly more efficient. An example of this is a solar cell consisting of MDMO-PPV polymer as donor and PCBM as acceptor, by which the power conversion efficiency was significantly increases due to the BHJ.[6],[7] In such a blend, photoinduced charge transfer occurs on a time scale of 45 fs, whilst photoluminescence happens around 1 ns.[8] Therefore, charge separation is much more favoured than the relaxation of the exciton, and thus increasing cell efficiency.

There is a plethora of viable donors (and after recently, acceptors as well) that can be implemented for the use in organic photovoltaic (OPV) devices. Polyphenylenevinylenes (PPVs) and polythiophenes (PTs) are important representations of hole-conducting donor-type semiconducting polymers.[2],[9] With most polymers having band gaps higher than 2 eV, only about 30% of solar photons can be absorbed (a band gap of 1.1 eV can absorb 77%). This is somewhat compensated for by the high absorption coefficient of organic materials which allows very thin films to be used – 200 nm thickness is enough to absorb most in its absorption range.[2] From these absorbed solar photons it is estimated that only 10% of excitons generated by photoexcitations lead to free charge carries in conjugated polymers.[10] Therefore, lower

© University of Pretoria

band gap polymers and more efficient charge separation are important pathways to more efficient organic solar cells.

As electron acceptors, fullerene derivatives (such as $PC_{60}BM$) have been used in the vast majority of BHJ solar cells. Fullerene possess a high electron affinity and good electron mobility.[11] Many of its advantageous properties are based on the 3D-conjugated cage structure characteristic to these molecules. E.g. the lowest occupied molecular orbitals (LUMOs) are delocalized across the entire buckyball surface, allowing isotropic and efficient electron transport.[12] The isotropic conjugated system also allows π-π interaction which leads to small scale aggregation of the acceptors within the bulk heterojunction mix.[13] This helps to control the nanomorphology which is important as the exciton diffusion length is then at the order of 10 nm.[2] Another property that makes fullerene derivatives good at charge separation is the low lying (0.2 - 0.4 eV) excited states in their anions. These states are responsible for a tenfold increase in the rate of charge separation with the recombination rate remaining unaffected. It is hypothesized that because of this, the Marcus inverted region[14] is not observed for the fullerenes as the electron can be transferred to the higher anionic excited states. These higher states thus provides an alternative pathway where $-\Delta G$ is smaller and therefore bypasses the inverted region.[15] The inverted region will be elaborated on later.

However, this same 3D cage structure also gives the most significant drawbacks of fullerene acceptors. The symmetric nature of the molecule gives rise to highly symmetric wavefunctions leading to forbidden optical transitions. It is therefore dependant on donor polymer excitation, limiting the maximum potential efficiency.[7] Also, with the LUMO delocalized on the surface of the cage, the tunability of the already suboptimum absorption spectrum is difficult. This adds to limiting the potential efficiency. Furthermore, as the open circuit voltage (V_{OC}) in organic solar cells is determined by the difference in energy between the HOMO of the donor and the LUMO of the acceptor, the ability to tune the acceptor's LUMO is critical for optimum solar cell performance.[1] The most efficient derivatives of fullerene are also very expensive.[15] In the past few years significant effort were given to development of non-fullerene acceptor (NFA) alternatives. Already a multitude of promising small molecule candidates to replace fullerene were presented, which demonstrates great potential beyond fullerene. These alternatives to fullerene-based acceptors have drawn new light to organic photovoltaics.[1]

Clearly there are several parameters that impacts the efficiency of OPV devices. Here the focus will be on the efficiency of charge separation at the donor acceptor interface. It is vital

© University of Pretoria

that the charge separation process occurs efficiently as this is one of the many critical variables responsible for a solar cell to be effective.[16] It is also important that the charge recombination is at a minimum.[5] A quantifiable parameter describing this is the rate of electron transfer.

Electron transfer rates

The Nobel Prize winning theory that quantify the rate of charge separation is Marcus theory.[17] This is described by the equation;

$$k = \sqrt{\frac{4\pi^3}{h^2 \lambda k_B T}} |V_{DA}|^2 e^{-\frac{(\Delta G^0 + \lambda)^2}{4\lambda k_B T}} \quad (1.1)$$

Here, k is the rate of electron transfer from the donor to the acceptor (charge separation, k_{CS}) or from the already charged acceptor to the already discharged donor (charge recombination, k_{CR}). h is Planck's constant, λ is the recombination energy – the energy required to rearrange the atoms in the molecules from the initial to final geometry when the electronic state of the molecule is kept constant (this can neither be negative nor zero). k_B is Boltzmann's constant, T is the temperature in Kelvin and ΔG^0 is the change in Gibbs free energy of the reaction. Lastly, V_{DA} is the electronic coupling – the energy associated with the electronic interaction between the initial and final state of charge transfer. The three variables which are species specific are λ, V_{DA} and ΔG^0.

In this work we are interested in developing design principles which will allow intended finetuning (rational design) of these parameters to ultimately design donor-acceptor pairs highly efficient at the charge separation process. For this we need an intrinsic understanding of the underlying chemical principles that govern them. Different chemical and structural features alter the physical properties of molecules by changing their electronic structure. Molecular electronic structures are complex quantum systems for which there are many developments attempting to describe it. We here give an overview on current theory of electron structure.

Lewis structures is one of the first concepts that describes the role of electrons in a molecule. However, this construct is very limited in that it does not describe delocalization, as all electrons are considered localized in a bond ('first-order' interactions) or on an atom (core electrons and lone pairs). It does not describe the underlying quantum nature of molecules which are intrinsically delocalized quantum objects. Incorporating delocalization into the Lewis structure approach can be seen as a 'second-order' correction of this description as the quantum nature is then accounted for (however, a correction is only necessary when starting

© University of Pretoria

with an incomplete description). These delocalization interactions are classified into three types of ubiquitous effects: conjugation, hyperconjugation and σ-conjugation. Conjugation is essentially some form and degree of delocalization, thus giving a full description and quantification of the one will describe and quantify the other. However, quantification of delocalization has never been a simple task. In past research there were numerous attempts to describe and quantify (hyper)conjugation.[18]

The concept of conjugation is familiar and need no introduction, however hyperconjugation is less heard of. Here follows a short overview of current theory on hyperconjugation as compiled in a recent review by Alabugin et al. The IUPAC definition for hyperconjugation is the interaction of σ- and π-orbitals.[18] Within the classification of hyperconjugation there is different types. There are sacrificial and isovalent. In short, in the resonance description of sacrificial hyperconjugation, one of the resonance structures present one bond less than that of the Lewis formula. In isovalent hyperconjugation all resonance structures have the same number of bonds. Then there is positive, negative and neutral hyperconjugation. The case where a filled σ-orbital donates into a π*- or unfilled p-type orbital is positive hyperconjugation. Interactions of filled π- or p-orbitals with σ*-orbitals is referred to as negative hyperconjugation. With neutral hyperconjugation there is no dominating effect thus donor and acceptor interactions are balanced. There are also different patterns of hyperconjugation which involves varying configurations of geometry and orbitals of the interaction in space. For a more elaborate explanation of each type the reader is referred to the recent review on hyperconjugation.[18]

With that said, hyperconjugation seems well defined and discrete. But it needs to be added that the distinction between conjugation and hyperconjugation is in reality nothing more than artificial – they describe the same fundamental phenomena and only differ in the participation of σ- and or π- orbitals.[18] With this being true, there cannot be assigned a discrete label and description to each interaction. Therefore, despite the qualitatively defined types mentioned, hyperconjugation really is a poorly defined range in a continuum of interactions of which 'normal' conjugation is also part of. This presents a challenge as no discrete label can be assigned to every delocalizing interaction within a molecule. Quantification of the delocalization seems more logical.

A significant amount of research attempts to quantify the phenomena of (hyper)conjugation (delocalization therefore) using geometry, energy, and magnetic criteria.[19] A way by which

© University of Pretoria

the stabilizing effect of (hyper)conjugation in terms of energy is studied, is by means of isodesmic reactions (possibly hypothetical reactions) – this can be done experimentally or computationally.[20,21] It measures the energy change upon a reaction in which there is, ideally, no change in hybridization, no change in the number and type of bonds (i.e. number of sp^3-sp^3 and sp^3-sp^2 (etc.) bonds should be equal before and after the reaction) and negligible change in steric and electrostatic effects. Any change in energy can therefore be assigned to the effect of (hyper)conjugation.[18] Due to all restrictions, this method cannot be applied to any system which is an obvious drawback since few systems will satisfy these requirements. Another way is by means of wavefunction analysis. Here the difference in energy between the state in which the delocalized interaction is absent (diabatic state) and the full state (adiabatic state) is computed. This, again, should give the energy only associated with delocalization and thereby leading to a means of quantifying it. The biggest challenge with this is to define the correct localized state to serve as the reference point.

Quantum Chemical Modelling

There are three wavefunction analysis approaches to disassemble the delocalized interactions; NBO (Natural Bond Orbital) analysis,[22] EDA (Energy Decomposition Analysis)[23] and the BLW (Block-Localized Wavefunction) method.[24] Each of these compare the full wavefunction with the hypothetical localized construct.[18] However, NBO analysis and the BLW method have some drawbacks and they do not agree upon the origin of the anomeric effect.[19] EDA, on the other hand, does provide a method to quantify conjugation.[23]

Furthermore, there are other methods by which information about the delocalization can be obtained. ACID (anisotropy of the induced current density) investigates electron current when an external electric field is applied. It is especially good at analysing aromaticity and its representations can detect and display even weak delocalization due to conjugation and hyperconjugation, etc.[25] It provides an intuitive way to represent the nature of the ring current in cyclic aromatic and non-aromatic systems. A drawback of this method is that it cannot be implemented in eminent quantum chemical software.[19] Also, it is claimed that "delocalization and aromaticity are virtual concepts, which cannot be measured directly experimentally".[25]

QTAIM (Quantum Theory of Atoms In Molecules), and ELF (Electron Localization Function) provide quantitative information highly useful for more detailed interpretations for electron delocalization and have been extensively used to investigate it.[25,26] Although, QTAIM fails to give a distribution throughout space of the ED associated with an atom. Instead,

© University of Pretoria

QTAIM limits the ED to an atomic basin and thus does not allow delocalization, or at least the quantification of it.

With all these tools at hand it is still admitted that the quantification of conjugation and hyperconjugation is rather challenging.[19] It was concluded by some authors[26] that there is no measure of aromaticity that can be applied universally. With aromaticity being a special case of delocalization (and more readily analysed due to geometric, energetic and magnetic properties) it should be clear that there is no measure of delocalization that can be applied universally. Furthermore, most visualization methods for delocalization offer only quantitative information.[25]

As it is the clearest seen in aromatics, delocalization largely impacts the physical properties of a molecule. As we shall see in this work, the degree of delocalization is key in order to tune properties such as the ionization potential and electron affinity. Altering hyperconjugation can therefore also be a useful tool for finetuning a molecule. The stereo-electronic nature of hyperconjugation presents additional ways for control over reactivity and stability.[18] I.e. hyperconjugative effects can be switched on and off through conformational changes.[18,19] For large systems (thin films) the extent of system conjugation plays a role in the lifetime of the excited state – a property critical for chromophores.[27] Naturally, this has direct implications on the performance of OPV devices.

In theoretical chemistry research, Quantum Chemical Topology (QCT)[28] is an emerging field which aims to predict and explain chemical phenomena through topological analysis of various fields. Among these fields the electron density distribution is the most explored. For the analysis of the electronic structure we here implement the recently developed QCT approach; Fragment, Atomic, Localized, Delocalized and Interatomic (FALDI) electron density decomposition scheme.[29–32] In contrast to the mentioned techniques, FALDI presents a way to separate the total electron density into localized and delocalized electron distributions. These can then be quantified and visualized in an atomistic manner, allowing non-local electron correlation effects to be recovered. This is extremely useful for isolating the effect that one atom or fragment has on the electronic structure and allows to study the reorganization thereof due to transitioning to another electronic state. It succeeds in recovering basic chemistry theory without inducing it, such as delocalization of a lone pair or conjugation. It therefore presents an intriguing approach to study the intricacies of systems such as delocalization and all its

© University of Pretoria

peculiarities. It is therefore promising for revealing the origin of the physical properties of a system.

Aims and objectives

This study is the first investigation and application of FALDI on electron transfer reactions. As such, the primary aim of this study is one of feasibility – is FALDI, in its current development, a viable tool to study intermolecular electron transfer reactions in small organic molecules? Technical challenges, numerical stability and consistency of FALDI results will also be investigated.

In addition to feasibility, this study also aims to provide some novel insight to the role of electron delocalization within electron transfer reactions. While the data sets investigated within this work is not large enough to draw wide-reaching conclusions from, we aim to provide some initial detail in an otherwise vague area of the discipline.

Thesis Outline

A detailed description of Marcus theory, FALDI and other computational methods used is provided in Chapter 2. To calculate rate constants and to implement FALDI, a set of small organic donors and acceptors were selected. In Chapter 3 the donors' ionization potentials are analysed with the FALDI results. Similarly, in Chapter 4 the acceptors' electron affinity are investigated. The purpose of these chapters is to first understand the individual characteristics of the donor and acceptor moieties before using them in an interface configuration. This assists in deciphering what kind of donors and acceptors behave in what way in an interface. Then in Chapter 5 various donor-acceptor interfaces were constructed for which electron transfer rates could be calculated. The rates of these interfaces are then compared to find the origin of their differences. In Chapter 6 we conclude.

References

[1] A. Wadsworth, M. Moser, A. Marks, M. S. Little, N. Gasparini, C. J. Brabec, D. Baran, I. McCulloch, *Chem. Soc. Rev.* **2019**, *48*, 1596–1625.
[2] S. Günes, H. Neugebauer, N. S. Sariciftci, *Chem. Rev.* **2007**, *107*, 1324–1338.
[3] S. Zhang, L. Ye, H. Zhang, J. Hou, *Mater. Today* **2016**, *19*, 533–543.
[4] Z. Zheng, O. M. Awartani, B. Gautam, D. Liu, Y. Qin, W. Li, A. Bataller, K. Gundogdu, H. Ade, J. Hou, *Adv. Mater.* **2017**, *29*, 1604241.
[5] V. Lemaur, M. Steel, D. Beljonne, J. L. Brédas, J. Cornil, *J. Am. Chem. Soc.* **2005**, *127*, 6077–6086.
[6] S. E. Shaheen, C. J. Brabec, N. S. Sariciftci, F. ; Padinger, T. ; Fromherz, J. C. Hummelen, *Appl. Phys. Lett.* **2001**, *78*, 841–843.

© University of Pretoria

[7] M. Wienk, J. Kroon, W. Verhees, J. Knol, J. Hummelen, P. van Hal, R. Janssen, *Angew. Chemie* **2003**, *115*, 3493–3497.
[8] C. J. Brabec, G. Zerza, G. Cerullo, D. Silvestri, S. Luzzati, J. C. Sariciftci, *Chem. Phys. Lett.* **2018**, *340*, 232–236.
[9] T. Liu, A. Troisi, *J. Phys. Chem. C* **2011**, *115*, 2406–2415.
[10] P. Barbeitas Miranda, *Artic. Phys. Rev. B* **2001**, *64*, DOI 10.1103/PhysRevB.64.081201.
[11] V. D. Mihailetchi, H. Xie, B. De Boer, L. J. A. Koster, P. W. M. Blom, *Adv. Funct. Mater.* **2006**, *16*, 699–708.
[12] Y. He, Y. L.-P. chemistry chemical physics, undefined 2011, *pubs.rsc.org* **n.d.**
[13] X. Yang, J. Loos, S. C. Veenstra, W. J. H. Verhees, M. M. Wienk, J. M. Kroon, M. A. J. Michels, R. A. J. Janssen, *Nano Lett.* **2005**, *5*, 579–583.
[14] R. A. Marcus, *Rev. Mod. Phys.* **1993**, *65*, 599–610.
[15] T. Liu, A. Troisi, *Adv. Mater.* **2013**, *25*, 1038–1041.
[16] M. Glatthaar, M. Riede, N. Keegan, K. Sylvester-Hvid, B. Zimmermann, M. Niggemann, A. Hinsch, A. Gombert, *Sol. Energy Mater. Sol. Cells* **2007**, *91*, 390–393.
[17] M. Chou, C. Creutz, N. Sutin, *J. Am. Chem. Soc.* **1977**, *99*, 5615–5623.
[18] I. V. Alabugin, G. dos Passos Gomes, M. A. Abdo, *Wiley Interdiscip. Rev. Comput. Mol. Sci.* **2019**, *9*, DOI 10.1002/wcms.1389.
[19] J. F. Gonthier, S. N. Steinmann, M. D. Wodrich, C. Corminboeuf, *Chem. Soc. Rev.* **2012**, *41*, 4671–4687.
[20] S. E. Wheeler, K. N. Houk, P. V. R. Schleyer, W. D. Allen, *J. Am. Chem. Soc.* **2009**, *131*, 2547–2560.
[21] M. D. Wodrich, C. S. Wannere, Y. Mo, P. D. Jarowski, K. N. Houk, P. Von Ragué Schleyer, *Chem. - A Eur. J.* **2007**, *13*, 7731–7744.
[22] F. Weinhold, C. R. Landis, E. D. Glendening, *Int. Rev. Phys. Chem.* **2016**, *35*, 399–440.
[23] L. Zhao, M. von Hopffgarten, D. M. Andrada, G. Frenking, *Wiley Interdiscip. Rev. Comput. Mol. Sci.* **2018**, *8*, DOI 10.1002/wcms.1345.
[24] Y. Mo, L. Song, Y. Lin, *J. Phys. Chem. A* **2007**, *111*, 8291–8301.
[25] P. von Ragué Schleyer, *Chem. Rev.* **2005**, *105*, 3433–3435.
[26] J. Poater, M. Duran, M. Solà, B. Silvi, **2005**, DOI 10.1021/cr030085x.
[27] U. Rant, U. Scherf, M. Rehahn, P. Galda, J. B.-S. metals, undefined 2002, *Elsevier* **n.d.**
[28] P. L. A. Popelier, S. Bond, *Springer* **2016**, *170*, 71–118.
[29] I. Cukrowski, D. M. E. van Niekerk, J. H. de Lange, *Struct. Chem.* **2017**, *28*, 1429–1444.
[30] J. H. de Lange, I. Cukrowski, *J. Comput. Chem.* **2018**, *39*, 1517–1530.
[31] J. H. de Lange, D. M. E. van Niekerk, I. Cukrowski, *J. Comput. Chem.* **2018**, *39*, 973–985.
[32] J. H. de Lange, I. Cukrowski, *J. Comput. Chem.* **2017**, *38*, 981–997.

© University of Pretoria

Chapter 2: Theoretical Background

Introduction

The results presented in this work are fully theoretical, utilizing modern quantum chemistry and electronic structure methods. Specifically, molecular wavefunctions and electron density distributions were produced using Density Functional Theory (DFT) to determine the electronic structure of many-body systems, whereas the Fragment, Atomic, Localized, Delocalized and Interatomic (FALDI) density decomposition scheme was primarily used for analysis. This Chapter provides a brief overview of the central concepts of both DFT and FALDI, as well as related concepts critical to either computational quantum chemistry or this study, such as basis sets and time-dependent DFT. Finally, a brief overview of Marcus theory is also provided as a model for electron-transfer processes.

An overview of Density Functional Theory

Solving the Schrödinger Equation

While not an *ab initio* method per se, DFT can provide highly accurate atomic and molecular properties through selection and application of a series of *functionals,* where a functional is defined as a function of a function. For DFT, the functionals are described by the spatially dependant electron density, hence the name *Density Functional Theory*. For the background on DFT covered here, the textbook "*A Chemist's Guide to Density Functional Theory*" by Wolfram Koch and Max C. Holthausen[1] was primarily consulted unless indicated otherwise.

We start out with the Schrödinger equation for a system of N electrons and M nuclei. This equation governs the wavefunction which contains all information about the molecular system. The Schrödinger equation is expressed as:

$$\hat{H}\Psi_a = \left[-\frac{1}{2}\sum_{i=1}^{N}\nabla_i^2 - \frac{1}{2}\sum_{A=1}^{M}\frac{1}{M_A}\nabla_A^2 - \sum_{i=1}^{N}\sum_{A=1}^{M}\frac{Z_A}{r_{iA}} + \sum_{i=1}^{N}\sum_{j>i}^{N}\frac{1}{r_{ij}} + \sum_{A=1}^{M}\sum_{B>A}^{M}\frac{Z_A Z_B}{R_{AB}} \right]\Psi_a = E_a\Psi_a \quad (2.1)$$

where $\hat{H}$ is the Hamiltonian operator, Ψ_a is the wave function describing the state with energy E_a, the first two bracket terms are the kinetic energy operators of the electrons and nuclei, the middel term the electron-nucleus interaction and the last two terms are the electron-electron and nucleus-nucleus repulsion operators. M_A is the mass of nucleus A, Z_A is the nuclear charge of nucleus A, r_{iA} is the spatial separation between electron i and nucleus A, r_{ij} the distance between electron i and j and R_{AB} the distance between nucleus A and B. Finally, the Laplacian

© University of Pretoria

operator ∇^2 is the sum of the differential (2^{nd} partial derivatives) operators in cartesian coordinates. Note that the system of atomic units is used in this representation of the Schrödinger equation – all constants are omitted, the mass of the nuclei are represented as multiples of the mass of an electron and the charge as multiples of the elementary charge. This minimizes computational cost by omitting the necessary numerical precision to deal with extremely small physical constants.

To solve eqn. 2.1 using iterative methods is difficult and computationally costly for all but the simplest molecular systems, due to the massive degrees of freedom imparted by both nuclear and electronic spin-spatial coordinates. To simplify it, the Born-Oppenheimer approximation is employed. This approximation entails that, since the nuclei are significantly more massive than the electrons, their velocities will be negligible compared to those of the electrons. The nuclei's velocities are therefore assumed to be zero. As a result, the kinetic energy term of the nuclei falls away and the nucleus-nucleus term becomes constant (for the specific system) leaving a static external potential through which the electrons move. From this a static electronic state is obtained and is described by the wavefunction that satisfies the time-independent Schrödinger equation. The Hamiltonian in eqn. 2.1 is therefore left with only the kinetic energy of the electron, the electron-nucleus and electron-electron interaction terms. The dependent variables in the equation reduces to three spatial and one spin coordinate of each electron (to a maximum of $4N$ variables).

Due to the electron-electron interaction term, eqn. 2.1 is still a many-body problem and cannot be separated into simpler single-body equations (the electron-electron potential energy depends on the simultaneous coordinates of two electrons). This does not allow the Schrödinger equation to be solved directly to find the true wavefunction, except for one-electron (hydrogenic) systems. It is therefore solved iteratively in which case the variational principle is evoked. This principle is one of the main mathematical concepts enabling the field of quantum chemistry. The variational principle states that the energy of any trail wavefunction is always lower bound by the true, observable energy. Therefore, any changes made to the approximate wavefunction lowers the molecular energy will result in a wavefunction that provides a more accurate description of reality. These incremental steps can then be repeated until the change in energy is minimized. In many DFT approaches, variational freedom lies in the coefficients of a linear basis set constructed as a Slater Determinant to ensure an antisymmetric wavefunction.

© University of Pretoria

Electron density and electron correlation

The electron density is an important quantity in chemical modelling and is central in DFT. The spin-independent electron density can be obtained directly from the electronic (Born-Oppenheimer) wavefunction:

$$\rho(\vec{r}) = N \int \dots \int |\Psi(\vec{x}_1, \vec{x}_2, \dots, \vec{x}_N)|^2 ds_1 d\vec{x}_2 \dots ds_N d\vec{x}_N \quad (2.2)$$

Eqn. 2.2. calculates the probability of finding any of the N electrons of the system in the volume element $d\vec{r}$ with arbitrary spin while the rest of the electrons can assume any spin and position. The square of the wavefunction is integrated over all spin coordinates and all spatial coordinates except one, such that $\rho(\vec{r})$ is a function of only three spatial variables. Furthermore, it is scaled by N, so integrating $\rho(\vec{r})$ over all space (asking how many electrons can be found in all space) results in N electrons, assuming that the wavefunction is square-normalized to unity.

Due to the particle-wave duality, electrons are highly correlated particles and exhibit many non-local properties. The electron density described by Eqn 2.2. contains no information on the electron-electron correlation in a many-electron system and we have to turn to the second-order pair density, $\rho_2(\vec{x}_1, \vec{x}_2)$. The spin-dependent pair density gives the probability of simultaneously finding two electrons of specific spin in volume elements $d\vec{r}_1$ and $d\vec{r}_2$ simultaneously, while all other electrons can assume any spin and position. This is represented by the equation:

$$\rho_2(\vec{x}_1, \vec{x}_2) = N(N-1) \int \dots \int |\Psi(\vec{x}_1, \vec{x}_2, \dots, \vec{x}_N)|^2 d\vec{x}_3 \dots d\vec{x}_N \quad (2.3)$$

This is a very important quantity as it contains all the information about electron correlation and electron dynamics in a molecular system. For instance, the Pauli Exclusion Principle dictates that the integrated pair-density of two electrons with parallel spin and identical spatial distributions be zero. The pair-density between electrons with parallel spin therefore accounts for Fermi- or spin-related electron correlation. However, the spin-independent pair-density is expected to be zero for two electrons at the same spatial position, $\rho_2(\vec{r}_1, \vec{r}_1) = 0$. Therefore, the pair-density between electrons of any spin accounts for Coulomb- or electrostatic electron correlation. The spin-independent pair density can also be given in terms of the 1st-order electron density:

© University of Pretoria

$$\rho_2(\vec{r}_1,\vec{r}_2) = \rho(\vec{r}_1)\rho(\vec{r}_2)[1 + f(\vec{r}_1,\vec{r}_2)] \tag{2.4}$$

where $f(\vec{r}_1,\vec{r}_2)$ is the correlation factor which accounts for the Fermi and Coulomb correlation as well as the normalization (which also takes care of electron self-interaction). In the completely uncorrelated case $f(\vec{r}_1,\vec{r}_2) = 0$. This introduces the problem that the unphysical self-interaction is now not taken care of anymore and the pair density will integrate to N^2 instead of N(N-1).

To further explore the effects of electron correlation on chemical systems, we now introduce the conditional probability which gives the probability of finding an electron at $\vec{r}_2$ if it is known that there is an electron present at $\vec{r}_1$ already:

$$\Omega(\vec{r}_2;\vec{r}_1) = \frac{\rho_2(\vec{r}_1,\vec{r}_2)}{\rho(\vec{r}_1)} \tag{2.5}$$

This integrates over the entire system to N – 1; containing all electrons except the reference electron at $\vec{r}_1$. The difference between the conditional probability and the completely uncorrelated probability of finding an electron at $\vec{r}_2$ gives the effect brought about by Fermi correlation, Coulomb correlation and the correction for self-interaction. As these correlation effects always results in electron density being depleted, this difference is termed the exchange-correlation hole:

$$h_{XC}(\vec{r}_1;\vec{r}_2) = \frac{\rho_2(\vec{r}_1,\vec{r}_2)}{\rho(\vec{r}_1)} - \rho(\vec{r}_2) = \rho(\vec{r}_2)\, f(\vec{r}_1,\vec{r}_2) \tag{2.6}$$

The exchange-correlation hole describes the degree to which electrons are excluded at $\vec{r}_2$ due to an electron travelling through $\vec{r}_1$. An important result of eqn. 2.6 is that over all space it integrates to –1, thus exactly one electron is excluded throughout space due to the reference electron at $\vec{r}_1$. Eqn. 2.6 can be separated into two components: the Fermi hole and the Coulomb hole.

The Fermi hole, which is a result of the antisymmetry of the wavefunction, is the exclusion of electron density at $\vec{r}_2$ due to a same spin reference electron at $\vec{r}_1$. Just like the total hole, the Fermi hole integrates to –1 and is negative or zero everywhere:

$$\int h_X(\vec{r}_1;\vec{r}_2)d\vec{r}_2 = -1 \tag{2.7}$$

Apart from the same spin correlation, the Fermi hole also takes care of the self-interaction due to it integrating to –1. Generally, as $\vec{r}_2$ approaches $\vec{r}_1$, the Fermi hole approaches $-\rho(\vec{r}_1)$,

© University of Pretoria

indicating predominant locality of the Fermi hole. However, electrons with parallel spins are highly correlated in chemical systems, and in particular in covalently-bound chemical structures or systems with high degrees of conjugation. In these cases, the Fermi hole is often highly delocalized over multiple centres and displays significant non-local character.

The Coulomb hole describes the degree to which an electron is excluded at $\vec{r}_2$ due only to the *charge* of the reference electron at $\vec{r}_1$. The Coulomb hole must then integrate to zero when considering that the total and the Fermi hole both integrates to –1:

$$\int h_C(\vec{r}_1;\vec{r}_2)d\vec{r}_2 = 0 \tag{2.8}$$

The Coulomb hole can therefore not be negative everywhere as it is not zero everywhere. It will be the most negative near the position of the reference electron but at some point further away, it will be positive. This makes physical sense: with the probe electron at $\vec{r}_1$, away from some nuclei near $\vec{r}_2$, the electron at $\vec{r}_2$ will be more strongly attracted to the region around the nuclei near $\vec{r}_2$ as these are now less shielded. In this case $h_C(\vec{r}_1;\vec{r}_2)$ will therefore be positive in the region of $\vec{r}_2$. Again, the Coulomb hole displays significant non-local character despite its seemingly "classical electrostatic" nature.

The combined exchange-correlation hole provides very useful insights into correlated electronic distributions. However, the electron hole can also be interpreted as the degree to which a reference electron at $\vec{r}_1$ is *delocalized* at $\vec{r}_2$, since the 1st-order electron density at $\vec{r}_2$ remains constant regardless of the presence of an electron at $\vec{r}_1$. This is a particularly useful interpretation that we will utilize later in this chapter.

Principles of Density Functional Theory

We have shown that the function of the electron density can be obtained from the wavefunction in eqn. 2.2, but this can also be reversed. The wavefunction can also be determined from the electron density, meaning that the wavefunction can be described as a functional of the electron density. This has the wonderful implication that all physical (Dirac) observables are functionals of the electron density; again, hence the name *Density Functional Theory*. So, in DFT we replace the N-electron wavefunction, which depends on the 3N spatial variables as well as the N spin coordinates, with the much simpler spin-independent electron density which only depends on 3 spatial variables.

© University of Pretoria

The first example where a density functional was used to calculate the energy of a system was in the Thomas-Fermi model, which initially assumed a uniform electron gas. The most important result here was that it was achieved by only using the electron density. At that time, it was not yet clear whether it is physically justifiable to do this and there were some major problems with the accuracy of the results. Nevertheless, this served as an important steppingstone to further develop the theory.

After the Thomas-Fermi model was the appearance of the Hohenberg-Kohn theorems. The first of these theorems indicated that a unique mapping between ground state electron density and ground state energy exists. This allowed the construction of a rigorous many-body theory using the electron density as the fundamental quantity. It did not give a method of how the energy functional should be constructed but gave confirmation that the Thomas-Fermi model – which asserts that only the electron density is required to extract all properties of a system – is indeed physically sound. This confirmation sparked the enthusiasm for fully developing the theory. Not long after this contribution of Hohenberg and Kohn, Kohn and Sham developed an approach for accurately minimizing the molecular energy functional.

Most of the problems with direct density functionals (like that of Thomas-Fermi) are connected to the way the kinetic energy is determined. The relationship between the spatial density distribution and the velocity of the electrons is not that trivial. To alleviate this, Kohn and Sham introduced the concept of a non-interacting reference system – a fictitious system that can be described to good accuracy, including the kinetic energy. In such a system the 'electrons' still behave like fermions but does not show any Coulomb correlation. Here it is not a problem to find the kinetic energy, which is attributable to the wavefunction being represented as a Slater determinant of orbitals – orbital-based approaches perform better in this respect. This leaves only a small part of the system to be approximated, which can be performed iteratively using approximate forms of the energy functionals.

From the Hohenberg-Kohn theorems, the ground state energy can be calculated variationally as

$$E_0 = \min_{\rho \to N} \left(F[\rho(\vec{r})] + \int \rho(\vec{r}) V_{Ne} d\vec{r} \right) \tag{2.9}$$

which minimizes the energy (calculated as a functional of the electron density) by varying the density distribution. V_{Ne} is the electron-nuclear attractive potential due to the nuclei (stationary within the Born-Oppenheimer approximation) and $F[\rho(\vec{r})]$ is defined as

© University of Pretoria

$$F[\rho(\vec{r})] = T_S[\rho(\vec{r})] + J[\rho(\vec{r})] + E_{XC}[\rho(\vec{r})] \tag{2.10}$$

where T_S is the exact kinetic energy of the non-interacting reference system which has the same electron density as the real system. Of course, $T_S \neq T$, the true kinetic energy. J is the electron-electron potential energy and E_{XC} is the exchange-correlation energy which is the sum of the remainder of the kinetic energy (not included in T_S) and the non-classical electrostatic contribution. It is the term that contains everything about our system that is unknown, yet the exact form of the E_{XC} functional itself is also not (yet) known. However, by virtue of the second Hohenberg-Kohn Theorem, the exact form of the E_{XC} functional will minimize the energy to the exact ground state energy.

The terms of eqn. 2.9 can be written in terms of 1-electron functions (known as "Kohn-Sham Orbitals" and henceforth referred to as only "orbitals") and combined in the form of a Slater determinant. So, we now apply the variational principle to eqn. 2.9 to find the orbitals that minimizes the energy under the condition that the orbitals are all orthonormal:

$$\left(-\frac{1}{2}\nabla^2 + \left[\int \frac{\rho(\vec{r}_2)}{r_{12}}\,d\vec{r}_2 + V_{XC}(\vec{r}_1) - \sum_A^M \frac{Z_A}{r_{1A}}\right]\right)\Phi_i = \varepsilon_i \Phi_i \tag{2.11}$$

where the terms in the square brackets is the effective potential through which the electrons move and Φ_i is the i^{th} orbital of the Slater determinant. To connect our artificial system to reality, the effective potential is chosen such that the electron density, resulting from the summation of the moduli of the squared orbitals, equals the density of the ground state of our target system. The entire rounded bracket in eqn. 2.11 is the one electron Kohn-Sham operator. The $V_{XC}(\vec{r}_1)$ term is the potential due to the exchange-correlation energy E_{XC}. It is not known what the explicit form of this term is hence it is only written as

$$V_{XC} \equiv \frac{\delta E_{XC}}{\delta \rho} \tag{2.12}$$

The approximations made in DFT only appears when deciding how the terms V_{XC} and E_{XC} should be represented. This is a central goal in DFT; to find better and better approximations for them. Other than that, the Kohn-Sham approach briefly described so far is exact.

To date, a large number of different E_{XC} functionals have been proposed based on numerous methodologies, such as empirical and experimental approaches as well as parameterizations based on high level *ab initio* calculations. Some functionals were developed for a specialized subset of chemical, while others are generalized. In particular, Becke's 3-parameter exchange

© University of Pretoria

functional combined with Lee, Young and Parr's correlation functional (B3LYP) is a popular generalized functional that can reproduce large sets of physical properties of both organic and inorganic compounds reasonably well; as a result, it is primarily used in this work. B3LYP is also a *hybrid* functional, in that it combines a proportion of exact *ab initio* exchange correlation (calculated by Hartree-Fock theory) with parameterized DFT Coulumb correlation.

TD-DFT

Time-dependent DFT (TD-DFT) allows for the calculation of excitation states. It is an extension to DFT with analogous computational and conceptual foundations. It is based on the Runge-Gross theorem which is the time-dependent analogue of the Hohenberg-Kohn theorem: the time-dependent wavefunction is shown to be equivalent to the time-dependent electron density and an effective potential is derived for a fictitious non-interacting reference system which returns the same density of the real system. It is considerably more accurate than CIS (Configuration Interaction Singles – a post-HF method for solving the Schrödinger equation), as it is using a density functional that includes electron correlation. In this project TD-DFT was a useful tool for finding the excitation states of molecules and extract all relevant information. It was used with the hybrid exchange-correlation functional named CAM-B3LYP – a functional that combines the hybrid qualities of B3LYP with a long-range correction which allows it to perform well with charge transfer excitations.[2]

Basis Sets

Each Kohn-Sham orbital is constructed as a linear combination of basis functions. The complete set of basis functions is therefore a set of real mathematical functions available to construct a wavefunction or orbitals to model a molecular system, such that the result is a superposition of these functions, each weighted by some coefficient. While an infinite basis set is required to provide enough variability to fully minimize molecular energy variationally, truncated basis sets are used out of computational necessity. There are numerous basis sets – each containing a specific set of functions to allow all kinds of shapes and properties to be modelled. For each project, a different basis set might be more ideal – the more elaborate the basis set the more computationally expensive it will be.

The basis set used in this project is aug-cc-pVDZ. That is short for augmented, correlation-consistent polarized, valence, double-zeta. In particular, aug-cc-pVDZ belongs to the relatively modern family of 'correlation consistent' basis functions designed to be used with high-level *ab initio* or DFT calculations, and consists of a large number of Gaussian functions. The

© University of Pretoria

'augmented' prefix adds diffuse low-amplitude long-range functions to allow description of long-range dispersion interactions. 'Polarized' means the basis set includes polarization functions (e.g. a set of p-type functions for every s-type function). 'Valence Double Zeta' – indicates a doubling of available functions to increase variability, but restricted to valence-shell electrons for reduced computational cost.[3]

An overview of the FALDI density decomposition scheme

For the goal of this project – to fully understand what chemistry gives large charge transfer rates and why – it is desirable to have a scheme that can decompose the electron density into digestible results. That is why we made use of the FALDI electron density decomposition scheme. This scheme makes use of concepts of the Domain Averaged Fermi-hole (DAFH) analysis[4],[5] and real-space definitions of atoms-in-molecules from the Quantum Theory of Atoms in Molecules (QTAIM)[6] to decompose the electron density into fragment, atomic, localized, delocalized, intra- and interatomic contributions.[7–10] FALDI is a recently developed in-house technique, and will be discussed in detail below.

DAFH density decomposition

DAFH analysis utilizes the Fermi and Coulomb electron holes, as averaged over atomic basins, in order to provide insightful information on the real-space distribution of an atom's electronic population. The DAFH equation[4],[5] gives the distribution of the electron density across 3D space at $\vec{r}_2$, found on average, in the domain Ω_i:

$$g_i(\vec{r}_2) = -\int_{\Omega i} \rho(\vec{r}_1)\, h_{XC}(\vec{r}_1;\vec{r}_2)\mathrm{d}\vec{r}_1 \qquad (2.13)$$

where Ω_i is a region of space occupied by atom *i* as defined by QTAIM atomic basins. The integrated term here is the exchange-correlation hole produced by a probe electron at $\vec{r}_1$, scaled by the electron density at the same coordinate. As mentioned before, $h_{XC}(\vec{r}_1;\vec{r}_2)$ can be interpreted as a measure of the degree to which an electron at $\vec{r}_1$ is delocalized at $\vec{r}_2$. If $\vec{r}_1$ is then integrated over some domain Ω_i as is done in eqn. 2.13, it then gives a distribution of the average electrons in Ω_i is delocalized through space (I.e. the rest of the molecule). This considers the correlated movements of electrons as it includes $h_{XC}(\vec{r}_1;\vec{r}_2)$. It is an extremely useful tool to investigate molecular delocalization and FALDI is built upon this concept.

Here are few properties of the DAFH equation which should aid in giving a more intuitive understanding of it.

© University of Pretoria

1. Integrating $g_i(\vec{r})$ over all space gives the electron population in the domain Ω_i:

$$N(\Omega_i) = \int_{\Omega i} \rho(\vec{r})d\vec{r} = \int_{-\infty}^{\infty} g_i(\vec{r})d\vec{r} \tag{2.14}$$

Therefore, $g_i(\vec{r})$ does not necessarily account for all electron density in the domain Ω_i (in fact it very rarely does), meaning that other domains' ED can be delocalized into domain Ω_i to make up the full ED as described by $\rho(\vec{r})$:

$$\rho(\vec{r}) = \sum_i g_i(\vec{r}) \tag{2.15}$$

If the ED in Ω_i is not delocalized at all then:

$$\int_{\Omega i} \rho(\vec{r})d\vec{r} = \int_{\Omega i} g_i(\vec{r})d\vec{r} \tag{2.16}$$

and $g_i(\vec{r}) = 0$ for all $\vec{r} \notin \Omega_i$.

2. Integration of $g_i(\vec{r})$ over the same basin Ω_i provides the QTAIM-defined localization index (LI) – the number of electrons localized to Ω_i:

$$\lambda(i) = \int_{\Omega i} g_i(\vec{r})d\vec{r} \tag{2.17}$$

3. Integration of $g_i(\vec{r})$ over a different basin, e.g. atom *j*, Ω_j, plus the integration of $g_j(\vec{r})$ over Ω_i gives the QTAIM-defined delocalization index (DI):

$$\delta(i,j) = \int_{\Omega j} g_i(\vec{r})d\vec{r} + \int_{\Omega i} g_j(\vec{r})d\vec{r} \tag{2.18}$$

where the QTAIM-defined DI is the magnitude of exchange of the electrons in the basin of atom *i* with those in the basin of atom *j*. It can be shown that the two summed terms in eqn. 2.18 are in fact equal, therefore only one of the terms gives half the DI.

4. From the previous properties it follows that the electron population of Ω_i can be written as:

$$N(\Omega_i) = \int_{\Omega i} g_i(\vec{r})d\vec{r} + \sum_{j \neq i}^{M-1} \int_{\Omega j} g_i(\vec{r})d\vec{r} \tag{2.19}$$

where M is then number of basins defined in the molecule. This allows the electron count of Ω_i to be decomposed into the localized (ED found on average in Ω_i) and delocalized (ED found on average in other basins but is delocalized onto Ω_i) contributions.

© University of Pretoria

To calculate $g_i(\vec{r})$ as proposed in eqn. 2.13 is ideal but very time consuming as it requires the full reduced two-electron matrix. However, it is approximated in this work using the Müller approximation:[11],[12]

$$g_i(\vec{r}) = \sum_{ab} \sqrt{\nu_a}\sqrt{\nu_b}\chi_a^*(\vec{r})\chi_b(\vec{r})S_{ab}^i \tag{2.20}$$

where χ_a and χ_b are molecular (Kohn-Sham) orbitals with occupancies ν_a and ν_b and $\mathbf{S}^i$ is the atomic overlap matrix (AOM) of atom *i*:

$$S_{ab}^i = \int_{\Omega i} \chi_a^*(\vec{r})\chi_b(\vec{r})d\vec{r} \tag{2.21}$$

The AOM provides information on how a MO or MO-pair contributes to the ED of atom *i*. This provides us with yet another way of expressing the electron count in some basin Ω_i as the sum of the diagonal elements, each weighted by its own occupancy:

$$N(\Omega_i) = \sum_a \nu_a S_{aa}^i \tag{2.22}$$

The off-diagonal terms of $\mathbf{S}^i$ gives important information about constructive and destructive interference of the MOs regarding basin Ω_i of atom *i*.

FALDI density decomposition

The DAFH function, $g_i(\vec{r})$, as calculated in eqn. 2.20, provides molecular-wide distribution of *atomic* electron populations and inherently includes electrons localized to the atomic basin or delocalized over another atomic basin. FALDI provides real-space, molecular-wide distributions of these localized and delocalized electrons. Therefore, FALDI provides a highly granular and exhaustive decomposition of the electron density at any given coordinate $\vec{r}$ into various contributions. These are the ED contribution of a molecular fragment, *frag-ED*, the ED contribution of an atom, *atom-ED*, the ED contribution of electrons localized on some atom, *loc-ED*, and the ED contribution of electrons delocalized across some atom pair, *deloc-ED*.

Atom-ED is the same as the DAFH function, $g_i(\vec{r})$, thus its properties and computations are the same as already discussed. *Frag-ED*, $g_{\{F\}}(\vec{r})$, is the sum of *atom-ED* distributions corresponding to a specified molecular fragment:

$$g_{\{F\}}(\vec{r}) = \sum_f g_f(\vec{r}) \tag{2.23}$$

© University of Pretoria

where *f* runs over all atomic basins of the atoms in fragment F. Naturally, this gives the contribution of the electrons, on average found on the fragment, at $\vec{r}$.

Loc-ED provides a spatial distribution of the ED counted towards the QTAIM-defined LI, which is the *atom-ED*, $g_i(\vec{r})$, integrated over its own basin Ω_i (Eqn. 2.17). This localized ED distribution of atom *i* is defined as:

$$L_i(\vec{r}) = \sum_{ab}^{N} \sqrt{\nu_a}\sqrt{\nu_b}\chi_a^*(\vec{r})\chi_b(\vec{r})(\mathbf{S}^i\mathbf{S}^i)_{ab} \tag{2.24}$$

This gives the contribution to the total ED at $\vec{r}$ due to electrons localized in Ω_i. When $L_i(\vec{r})$ is integrated over all space, the QTAIM-defined LI for atom *i* is recovered. Recalling eqn. 2.17, this can be represented as:

$$\lambda(i) = \int_{-\infty}^{\infty} L_i(\vec{r})d\vec{r} = \int_{\Omega i} g_i(\vec{r})d\vec{r} \tag{2.25}$$

Analogously, *deloc-ED* gives a spatial distribution of the QTAIM-defined DI between atom *i* and *j*, which is twice $g_i(\vec{r})$ integrated over basin Ω_j. This delocalized ED distribution between atom *i* and atom *j* is defined as:

$$D_{ij}(\vec{r}) = \sum_{ab}^{N} \sqrt{\nu_a}\sqrt{\nu_b}\,\chi_a^*(\vec{r})\chi_b(\vec{r})(\mathbf{S}^i\mathbf{S}^j + \mathbf{S}^j\mathbf{S}^i)_{ab} \tag{2.26}$$

This gives the contribution to the total ED at $\vec{r}$ due to electrons delocalized between Ω_i and Ω_j. When $D_{ij}(\vec{r})$ is integrated over all space, the QTAIM-defined DI for atom *i* and *j* is recovered. Recalling eqn. 2.18, this can be represented as:

$$\delta(i,j) = \int_{-\infty}^{\infty} D_{ij}(\vec{r})d\vec{r} = \int_{\Omega j} g_i(\vec{r})d\vec{r} + \int_{\Omega i} g_j(\vec{r})d\vec{r} \tag{2.27}$$

Through the *loc-ED* and *deloc-ED* terms, the *atom-ED* can be perfectly decomposed into 1-body and 2-body contributions as:

$$g_i(\vec{r}) = L_i(\vec{r}) + \frac{1}{2}\sum_{j\neq i}^{M-1} D_{ij}(\vec{r}) \tag{2.28}$$

where the half of the sum of DI terms are taken since $\int_{\Omega j} g_i(\vec{r})d\vec{r} = \int_{\Omega i} g_j(\vec{r})d\vec{r}$. *Frag-ED* can therefore also be decomposed into an ED distribution for electrons localized to their basins and

© University of Pretoria

one that shows the ED distribution delocalized between different fragments. And finally, the total ED can be decomposed into localized and delocalized contributions:

$$\rho(\vec{r}) = \sum_{i}^{M} L_i(\vec{r}) + \frac{1}{2}\sum_{i}^{M}\sum_{j\neq i}^{M-1} D_{ij}(\vec{r}) \tag{2.29}$$

where M is again the number of basins in the molecule.

Exclusively Localized FALDI distributions

The movement of electrons within a molecule is often imagined as weighted contributions of several resonance structures – such a pictorial representation can be applied here as well. Considering a simple covalent bond, eqn. 2.26 gives the electron distribution of the resonance structure where the electrons are shared equally between two atoms. Likewise, eqn. 2.24 gives the distribution of the resonance structure that describes the case where the electrons are only found on one of the atoms. This might seem to be a perfectly fine approach to take, but there are inherent problems with it as will become clear when the distributions are visualised; The isosurface of the ED distribution of $L_i(\vec{r})$ (eqn. 2.24) is delocalized towards other atoms, thus cannot be a realistic representation of the electrons only localized to atom *i*. This also means that there is delocalized ED contained in $L_i(\vec{r})$ that should really be accounted for by $D_{ij}(\vec{r})$. This problem is mitigated by the Localized-Overlap algorithm (FALDI-LO)[6] and here follows a description how it is achieved.

The goal is to correct $L_i(\vec{r})$ and $D_{ij}(\vec{r})$ exactly where it fails based on whether each of its components are physically sound or not. To do this we need to redefine $L_i(\vec{r})$ and $D_{ij}(\vec{r})$ as linear combinations of sub-components. Therefore, the first step is to convert $L_i(\vec{r})$ and $D_{ij}(\vec{r})$ into a set of orthogonal functions termed *natural density functions* (NDFs). This is accomplished by diagonalizing the matrices $\mathbf{S}^i\mathbf{S}^i$ and $\mathbf{S}^i\mathbf{S}^j$ ($\mathbf{S}^i\mathbf{S}^j \equiv \mathbf{S}^i\mathbf{S}^j + \mathbf{S}^j\mathbf{S}^i$) from eqn. 2.24 and 2.26, respectively, through a unitary transformation matrix, $\mathbf{U}^{ix}$, of which the columns are eigenvectors associated with $\mathbf{S}^i\mathbf{S}^x$. From the matrix elements of $\mathbf{U}^{ix}$ and $\mathbf{S}^i\mathbf{S}^x$, the occupations, n_α^{ix}, of the NDFs are calculated (n_α^{ij} is the occupation of NDF α of the ED distribution delocalized between atom *i* and *j*. If *j* = *i*, it gives the occupation of a *loc-ED* NDF). *Loc-ED* and *deloc-ED* is reconstructed as a sum of NDFs. *Loc-ED* is constructed as follows:

$$L_i(\vec{r}) = \sum_{\alpha} n_\alpha^{ii}\left[\varphi_\alpha^{ii}(\vec{r})\right]^2 \tag{2.30}$$

© University of Pretoria

where $\varphi(\vec{r})$ is a *Doman Natural Orbtial*:

$$\varphi_{\alpha}^{ii}(\vec{r}) = \sum_{b}^{N_{MO}} \chi_{b}(\vec{r}) U_{b\alpha}^{ii} \tag{2.31}$$

and N_{MO} is the number of MOs in the system. The sum of the occupations in eqn. 2.30 gives the QTAIM-defined LI. Analogously, the *deloc-ED* is defined as

$$D_{ij}(\vec{r}) = \sum_{\alpha} n_{\alpha}^{ij} \left[\varphi_{\alpha}^{ij}(\vec{r})\right]^2 \tag{2.32}$$

with the sum of these occupations giving the QTAIM-defined DI.

Now that $L_i(\vec{r})$ and $D_{ij}(\vec{r})$ is defined as a linear combination of NDFs, the next step is to measure the degree of overlap between all localized NDFs (*loc-NDFs*). Specifically, due to the diagonalization of $\mathbf{S}^{i}\mathbf{S}^{i}$, *loc*-NDFs of the same atomic basin will have net zero overlap; the same is not true, however, of *loc*–NDFs between different atomic basins. The total Localized Overlap (LO) of *loc*–NDFs of atom α and all other *loc*-NDFs of the molecule is calculated as,

$$LO(L_i^{\alpha}) = \sum_{x \neq i}^{M_{Atoms}} \sum_{\beta} s(L_i^{\alpha}, L_x^{\beta}) \tag{2.33}$$

where $s(L_i^{\alpha}, L_x^{\beta})$ is the overlap between the α^{th} NDF of the *loc-ED* of atom *i* and the β^{th} NDF of that of atom *x*. The localized overlap function, $LO(L_i^{\alpha})$, therefore gives the number of electrons in the indicated NDF that is not really localized to atom *i*. This quantity is then used to correct the occupation of a particular NDF:

$$n'^{ii}_{\alpha} = n_{\alpha}^{ii} - LO(L_i^{\alpha}) \tag{2.34}$$

such that n'^{ii}_{α} is the LO-free occupation. In the case where $n_{\alpha}^{ii} < LO(L_i^{\alpha})$, $n'^{ii}_{\alpha} = 0$. The corrected occupations can then be substituted into eqn. 2.30 to give the LO-free *loc-ED* distribution:

$$L'_i(\vec{r}) = \sum_{\alpha} n'^{ii}_{\alpha} \left[\varphi_{\alpha}^{ii}(\vec{r})\right]^2 \tag{2.35}$$

When eqn. 2.35 is integrated over all space, the LO-free LI, $\lambda_{LO-free}(i)$, is obtained.

The overlap between the *loc-NDFs* of atoms *i* and *j* should then be added to the *deloc-NDF* of this atom-pair to give the corrected *deloc-ED* distribution. The occupations are adjusted as a fraction of $(n_{\alpha}^{ii} - n'^{ii}_{\alpha})$:

© University of Pretoria

$$n'\left(L_i^{\alpha} \rightarrow D_{ij}^{\gamma}\right) = w'(L_i^{\alpha}, D_{ij}^{\gamma})(n_{\alpha}^{ii} - n'^{ii}_{\alpha}) \quad (2.36)$$

where $n'\left(L_i^{\alpha} \rightarrow D_{ij}^{\gamma}\right)$ is the adjusted occupation of the γ^{th} *deloc-NDF* of atom-pair *i-j*, and $w'(L_i^{\alpha}, D_{ij}^{\gamma})$ is the weighting factor specific to it. After this adjustment, the LO-free *deloc-ED* distribution in terms of NDFs becomes:

$$D'_{ij}(\vec{r}) = \sum_{\gamma} n_{\gamma}^{ij}\left[\varphi_{\gamma}^{ij}(\vec{r})\right]^2 + \sum_{\gamma}\sum_{\alpha}\{n'\left(L_i^{\alpha} \rightarrow D_{ij}^{\gamma}\right)\left[\varphi_{\alpha}^{ii}(\vec{r})\right]^2 + n'\left(L_i^{\alpha} \rightarrow D_{ij}^{\gamma}\right)\left[\varphi_{\alpha}^{jj}(\vec{r})\right]^2\} \quad (2.37)$$

which when integrated over all space gives the LO-free DI, $\delta_{LO-free}(i,j)$. It should be noted that this DI is interpreted as the number of electrons shared between atom *i* and *j*. It is therefore not the bond order between these two atoms as is assumed in QTAIM of the QTAIM-defined DI.

After this procedure, the fraction of any MO that contributes to the LI of two or more atoms will be corrected – removed from the relevant *loc-ED* distribution and added to the relevant *deloc-ED* distribution. When eqn. 2.35 is visualised, the ED will now be strictly localized to some atom and should not show delocalization towards others. $L'_i(\vec{r})$ does therefore not provide a lot of information as the distributions mostly show the core electrons, however it can be useful for studying lone pair electrons. Furthermore, $D'_{ij}(\vec{r})$ is now invaluable as this now gives a more physically sound approximation to the *deloc-ED* distribution, therefore can quantitatively show effects of different chemistry in molecules. It is these two terms implemented on our hand-picked molecular fragments that makes up the FALDI results used in this study.

Marcus Theory

A central theme of this work, as well as future research based on this work, is that of modelling electron transfer processes. Nobel laureate Rudolph Marcus' theory[13],[14] allows for the predictive quantification of electron transfer rates and is described by the equation

$$k = \sqrt{\frac{4\pi^3}{h^2\lambda k_B T}}|V_{DA}|^2 e^{-\frac{(\Delta G^0+\lambda)^2}{4\lambda k_B T}} \quad (2.38)$$

Here *k* is the rate of electron transfer from the donor to the acceptor (charge separation, k_{CS}) or from the already charged acceptor to the already discharged donor (charge recombination, k_{CR}). *h* is Planck's constant, λ is the recombination energy which can neither be negative nor zero (energy required to rearrange the atoms in the molecules from the initial to final geometry when

© University of Pretoria

the electronic state of the molecule is kept constant), k_B is Boltzmann's constant, T is the temperature in Kelvin, V_{DA} is the electronic coupling between donor $\mathcal{D}$ and acceptor $\mathcal{A}$ of the initial and final state and ΔG^0 is the change in Gibbs free energy of the reaction. This theory suggests that it is not as simple to look at the HOMO and LUMO of the donor and acceptor to determine its efficiency. Eqn. 2.38 is also known as the Marcus equation.

Marcus theory holds when applied to electron transfer between species where there is no formation or dissociation of bonds.[15] Therefore, the two species do not undergo significant structural changes and thus retains their individuality, thereby allowing for convenient calculation of the parameters used in the Marcus equation. The species dependent parameters in eqn. 2.38 are: i) the change in the Gibbs free energy, ΔG^0, ii) the reorganization energy, λ, and iii) the coupling potential, V_{DA}. Each of these parameters play an important role in determining the rate of electron transfer, yet chemical structure-property relationships for these factors are far and few between. The in-depth investigation and interpretation of these parameters are therefore of great importance in this work.

The structure of eqn. 2.38 may look somewhat familiar – it closely resembles the Arrhenius equation:

$$k = Ae^{-\frac{E_a}{k_B T}} \tag{2.39}$$

which describes the rate of a chemical reaction; thus, the Marcus equation is simply an analogue for the rate of electron transfer. Comparing eqn. 2.38 and 2.39, we can deduce that $\Delta G^{\ddagger} = \frac{(\Delta G^0+\lambda)^2}{4\lambda}$ resembles the activation energy of the process and $\sqrt{\frac{4\pi^3}{h^2\lambda k_B T}}|V_{DA}|^2$ resembles the pre-exponential factor which gives k in units of electrons per second (e^-/s). In contrast to the Arrhenius equation, the Marcus equation does not have a constant pre-exponential factor as it is dependent on the temperature, reorganization energy and the coupling and therefore more closely resembles a modified Arrhenius equation.[16]

A remarkable result of the Marcus equation is the so called 'inverted region'. By considering most reactions' ΔG^0 value, we can tell how spontaneous and therefore at what rate it will happen. A very negative ΔG^0 would suggest a large rate constant and a less negative ΔG^0 a small one as the energetic driving force will then not be as great.[17] However, electron transfer rates described by Marcus theory behaves differently. When carefully considering eqn. 2.38,

© University of Pretoria

there must be an optimal value of ΔG^0 for a given system. To be more specific, $-\Delta G^0$ should equal λ or at least be close to it for optimum transfer rates – if not, the rate suffers as a result. This is best illustrated in Figure 1 which gives the rate constant as a function of ΔG^0 and λ. From this it is clear that for some reorganization energy λ there exists an optimal value of ΔG^0 that will result in the maximum rate constant. The region left to the maximum on the red line is the inverted region of ΔG^0 – the more negative ΔG^0 becomes in this region, the slower the rate of electron transfer will be.

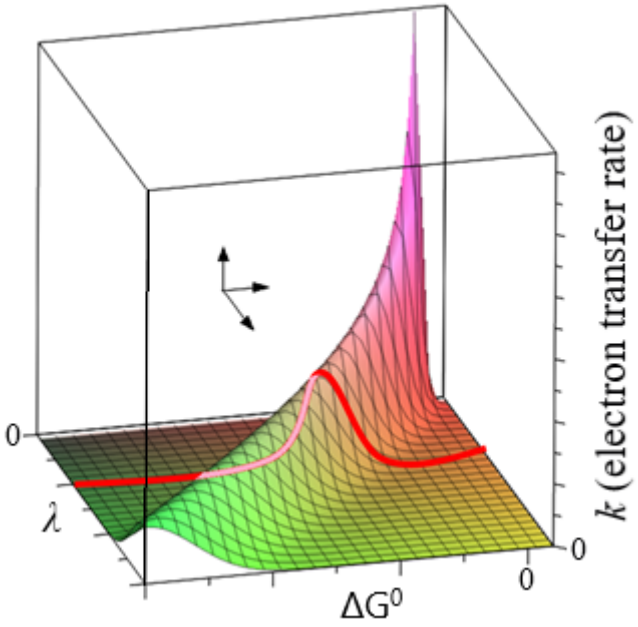

Figure 2.1. The rate constant as a function of both the reorganization energy as well as the change in Gibbs free energy, for constant temperature T=298 K.

While all of the species-dependent parameters in the Marcus equation can be calculated from first principles with a suitable multi-determinant wavefunction, exact determination requires a full nuclear and electronic wavefunction, i.e. non-adiabatic approaches. These approaches are computationally unfeasible for the molecular sizes of systems studied in this work, which is modelled with an adiabatic Born-Oppenheimer (BO) approach. Nevertheless, various methods have been reported in literature to approximate the parameters of the Marcus equation in terms of physical properties of different BO surface, e.g. ground, excited or ionic states of donor and acceptor molecules at various geometries. The specific approach used in this work to calculate Marcus equation parameters is described below.

The energetic driving force of the electron transfer reaction, ΔG^0, can be estimated as follows:[18]

© University of Pretoria

$$\Delta G^0 = (E_{D+} - E_{D*}) + (E_{A-} - E_A) + \Delta E_{col} \tag{2.40}$$

where $(E_{D+} - E_{D*})$ is the ionization potential (IP) of the donor, $(E_{A-} - E_A)$ is the negative of the electron affinity (EA) of the acceptor and ΔE_{col} is the change in total coulombic potential energy at the donor-acceptor interface, before and after electron transfer. It is assumed that the donor is excited by a photon and thereby E_{D*} is the energy for the initial excited state of the donor, thus the IP in eqn. 2.40 is the energy required to ionize the *excited* donor. If the rate constant is calculated when no photoexcitation took place, E_{D*} is simply replaced with E_D – the ground state donor energy. ΔE_{col} is the change in the Coulombic repulsion energy between the shielded nuclear charges in the donor and that in the acceptor and is calculated as:

$$\Delta E_{col} = \sum_{D+}\sum_{A-} \frac{(q_{D+}q_{A-})}{r_{D+A-}} - \sum_{D*}\sum_{A} \frac{(q_{D*}q_{A})}{r_{D*A}} \tag{2.41}$$

where q is the atomic charge as calculated by QTAIM and r is the internuclear distance. Here the energy will be given in atomic units.

The reorganization energy, λ, is the energy required to change the geometry of the molecules from the optimum geometry of the one state to that of the other state while electronically the state remains the same. λ is calculated here as the average of $\lambda_{[D*A]}$ and $\lambda_{[D+A-]}$,

$$\lambda_i = \frac{\lambda_{[D*A]} + \lambda_{[D+A-]}}{2} \tag{2.42}$$

where $\lambda_{[D*A]}$ is the difference in energy of the reactants (prior to charge transfer) at the product (charge transfer state) geometry and the reactants at their optimum geometry, and $\lambda_{[D+A-]}$ is the difference in energy of the products at reactant geometry and the products at optimal geometry:[19]

$$\lambda_{[D*A]} = \left(E_{D*(+)} + E_{A(-)}\right) - (E_{D*} + E_A) \tag{2.43}$$

and analogously for $\lambda_{[D+A-]}$. Figure 2 showing the energy-geometry curves of the different states explains this more elegantly. The terms $E_{D*(+)}$ and $E_{A(-)}$ are the energy of the excited donor at the cationic optimized geometry and of the neutral acceptor at anionic optimized geometry, respectively. Note that if the BO surfaces describing the different electronic states have identical curvature, it is expected that $\lambda_{[D*A]} = \lambda_{[D+A-]}$. However, such distributions are very unlikely for complex, asymmetric organic molecules and hence the average of $\lambda_{[D*A]}$ and $\lambda_{[D+A-]}$ is necessary.

© University of Pretoria

The reorganization energy has two components, the internal, λ_i, describing the geometrical changes of the donor and acceptor molecules themselves, and the external component, λ_e, describing the geometrical changes of the donor and acceptor's response to the environment.[18],[20] Here, only the internal reorganization energy is used to approximate the true reorganization energy. The external reorganization energy should be accounted for if there is a solvent effect or when the there is some solid phase effect such as a crystal lattice in which the donor and acceptor is packed. As the modelling done here is mainly to gain a qualitative understanding of isolated interface systems, accounting for λ_e is beyond the scope of this project and the modelling is thus essentially done in gas phase. The subscript i will therefore be dropped when referring to the reorganization energy.

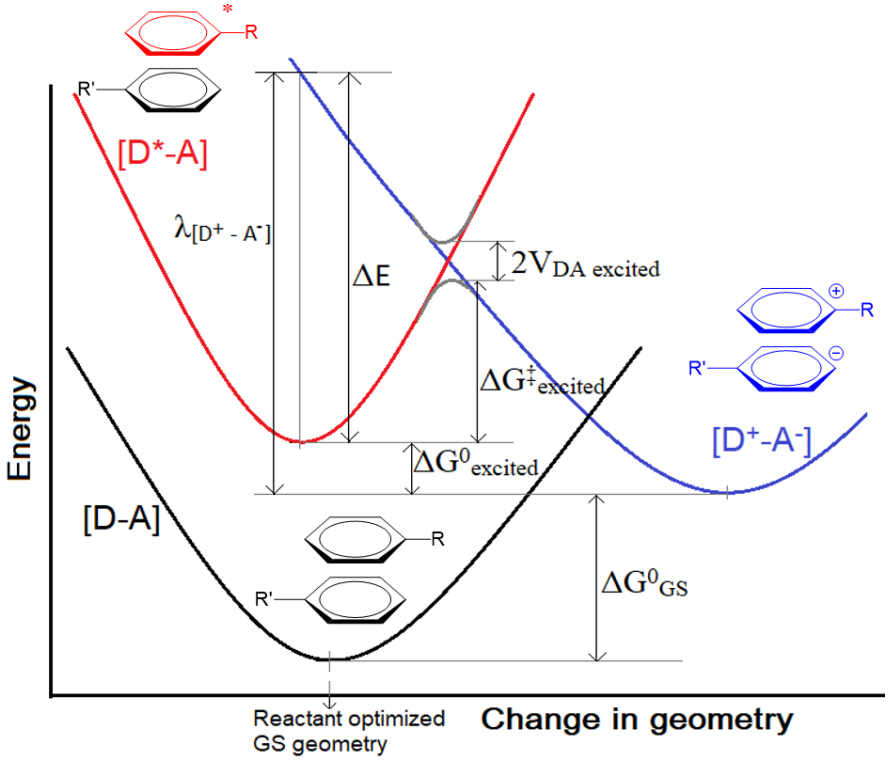

Figure 2.2. Potential energy wells for neutral and non-excited state ([$\mathcal{D}$-$\mathcal{A}$], black), neutral donor excited state ([$\mathcal{D}$*-$\mathcal{A}$], red) and the cationic donor anionic acceptor charge separated state ([$\mathcal{D}^+$-$\mathcal{A}^-$], blue). Parameters used in the Marcus equation are visually illustrated here.

The coupling potential, V_{DA}, gives the energy due to the electronic coupling of the donor and acceptor interface between the initial and final state (see Figure 2). Due to the spatial dependence of the coupling, it is strongly influenced by the relative spatial orientation of the donor and acceptor.[18] It is also dependent on the solvent effects or the external environment

© University of Pretoria

in which the system is. However, our modelling is done in gas phase thus this effect will not be accounted for. V_{DA} is calculated as the electronic overlap of the initial and final electronic states and can therefore be written as

$$V_{DA} = \int \Psi^*_{[D*A]} \Psi_{[D+A-]} d\tau. \tag{2.44}$$

Notably, however, is that V_{DA} is calculated at the exact transition state between reactants and products. If the excited state wavefunction of the donor is to a great extent (>80%) described by a single transition (i.e. $HOMO_D \rightarrow LUMO_D$), the coupling can be approximated as that between $LUMO_D$ and $LUMO_A$ (assuming $LUMO_A$ is the MO accepting the electron).[18] But generally, solving eqn. 2.44 directly is challenging and usually requires non-adiabatic procedures to find the exact transition state. However, various approximations of V_{DA} have been developed, and the popular generalized Mulliken-Hush (GMH) approximation[21],[22] is employed in this work. The GMH approximation relates V_{DA} to the dipole-moment differences and coupling between the reactant and product states:

$$V_{DA} = \frac{\mu_{tr} \Delta E}{\sqrt{\Delta\mu^2 + 4{\mu_{tr}}^2}} \tag{2.45}$$

where μ_{tr} is the transition dipole-moment from initial to final state, $\Delta\mu$ is the change in stationary dipole moment and ΔE is the difference in the electronic energy between the initial and final state (also known as the vertical excitation energy). The transition dipole moment is defined as

$$\vec{\mu}_{tr} = \int \Psi^*_f \hat{\boldsymbol{\mu}} \Psi_i d\tau \tag{2.46}$$

with Ψ_i and Ψ_f representing the initial and final state, respectively, and $\hat{\boldsymbol{\mu}}$ is the electric dipole moment operator.

Eqn. 2.45 allows for accurate calculation of V_{DA} in many types of systems, independent of geometrical constraints, symmetry, or number of interacting states, and at the convenience of only requiring adiabatic state parameters.[19],[23]

Since dipoles are vector quantities, their use in eqn. 2.45 are as follows; $\vec{\mu}_{tr}$ is projected onto $\Delta\vec{\mu}$ after which the magnitude is calculated – this scalar quantity is then used for μ_{tr}. For

© University of Pretoria

$\Delta\mu$, the magnitude of $\Delta\vec{\mu}$ is used. Since V_{DA} is squared in the Marcus equation, the rate constant is not sensitive towards the order of calculation of V_{DA}.

To ensure that the calculation of V_{DA} in the GMH approximation is not overly dependent on the orientation between the two molecules in the interface, it can be averaged over different relative orientations.[18] However, that is a labour-intensive task especially for multiple interfaces. To ensure consistency in the results of V_{DA}, the interfaces were constructed in a mathematically exact way by means of an in-house algorithm developed during this project: On each molecule three atoms are selected (A1, A2 and A3 and B1, B2 and B3 for molecule A and B, respectively). These are selected by the user knowing that the two planes that passes through these two sets of atoms will be aligned parallel in the end. From the spatial coordinates of these atoms, a mathematical expression is obtained for each plane in space that cuts through the three coordinates – plane A for A1, A2 and A3 and similarly for plane B. Plane A is then rotated parallel to B and then shifted in space such that A1 and B1 share the same coordinate. Thereafter, plane A is rotated about the axis perpendicular to the planes and that passes through the coordinate of A1 and B1. The rotation is performed with the constraint to minimize the distance between A3 and B3. The planes are then separated apart the desired distance (in all interfaces that will be considered here, the distance was set to 4 Å). All mathematical operations performed on A1 –A3 are performed on the rest of the atoms in molecule A as well. The result is two molecules separated in a mathematically perfect fashion and the result is shown in Figure 3.

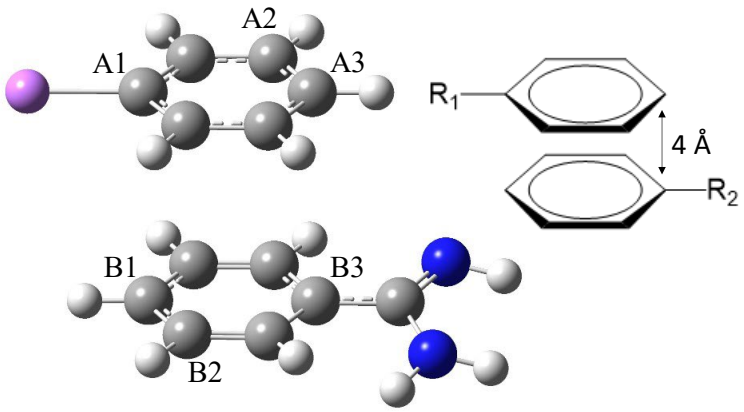

Figure 2.3. Example of how two molecules are aligned by the algorithm.

© University of Pretoria

There are alternative ways proposed for calculating the electronic coupling. These are energy level splitting,[24] fragment charge difference[25] and constrained DFT.[25] Investigation of these methodologies are, however, outside of the scope of this work.

The quantities ΔG^0, λ and V_{DA} are conveniently visualised with the energy-geometry diagram in Figure 2. Here, each energy-well is the diabatic (imaginary and thus non-interacting) representation of an electronic state. The energy of the state is given at some geometry which is varied along the x-axis via a single virtual geometry coordinate.

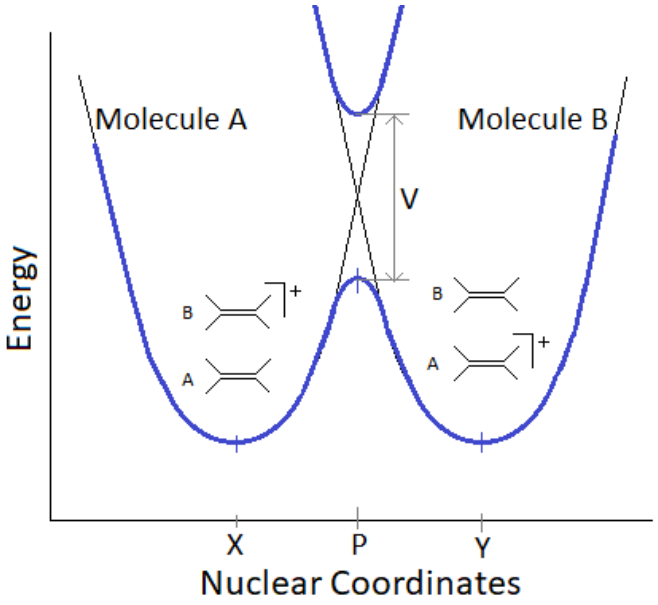

Figure 2.4

To aid in the understanding of diabatic, adiabatic and non-adiabatic states we consider Figure 4. In adiabatic states there is strong electronic coupling between the two molecules. The Born-Oppenheimer approximation is therefore considered valid as the effect of nuclear vibrational modes is overshadowed by the coupling, resulting in these modes to have little effect on the charge transfer.

To obtain the potential energy curve in blue as in Figure 4, the nuclear geometry of one of the molecules is changed manually (in this case molecule A), while the geometry of the other molecule is left free to adjust to any changes of electronic energy and structure. In this case molecule A and B are the exact same moiety hence the symmetry, however their initial and final states differ – molecule A starts in the state that B ends up in. The two potential energy wells labelled molecule A and B represents the energy of the state located on molecule A and B, respectively, both as a function of the nuclear geometry of molecule A.

© University of Pretoria

We assume the C-C bond is elongated in A thus pulling the molecule apart. This will correspond to starting from nuclear coordinate X and moving towards Y. During this process, at every infinitesimally small step taken, molecule B, which is free to rearrange, will be optimized and the potential energy of the system will be calculated assuming the Born-Oppenheimer (B-O) approximation – this gives rise to the blue energy curve. As molecule A is stretched an electron that is participating in the double bond is being destabilised and thus the potential energy increases as we move towards coordinate Y. As this continues the electron in A is destabilised more and more until it is more favourable for it to jump to molecule B where it can be stabilised as this molecule's geometry is free to change. This electron jump occurs as the geometry crosses the point P. This jump is only possible when there is coupling between the electronic states of the two molecules. Furthermore, note that the potential energy curve does not follow the exact path of that of the individual molecules (equivalent to non-interacting molecules) near the point of intersection around coordinate P. This is a result of the coupling between the molecules which allows a lower system energy. And naturally, the stronger the coupling is the lower the energy at coordinate P will be.

In this adiabatic case it is very reasonable to assume that the lower curve will be followed 100% of the time since there is a large energy gap between the upper and lower curve. Although in non-adiabatic cases where the coupling is weak, the occurrences is distributed between these two energy curves. This is because of nuclear vibrations starting to become prominent due to the low electronic coupling. In this case it is no longer correct to consider full B-O treatment. Instead, a single most relevant vibrational mode is considered while all other modes are still getting B-O treatment. In such a case of weak interaction, from Fermi's Golden rule, the electron transfer rate is predicted to be proportional to $|V_{DA}|$[19,26–28].

Furthermore, the system is diabatic when there is no coupling between molecules at all. In this case there is zero probability that the electron can jump to the other molecule and thus the potential energy will simply keep increasing – the diabatic curve will be followed.

References

[1] W. Koch, M. C. Holthausen, *A Chemist's Guide to Density Functional Theory*, Wiley-VCH, **2001**.

[2] T. Yanai, D. P. Tew, N. C. Handy, *Chem. Phys. Lett.* **2004**, *393*, 51–57.

[3] T. H. Dunning, *J. Chem. Phys.* **1998**, *90*, 1007.

© University of Pretoria

[4] R. Ponec, *J. Math. Chem.* **1997**, *21*, 323–333.

[5] R. Ponec, *J. Math. Chem.* **1998**, *23*, 85–103.

[6] R. Bader, T. Nguyen-Dang, *Adv. Quantum Chem.* **1981**, *14*, 63–124.

[7] J. H. de Lange, I. Cukrowski, *J. Comput. Chem.* **2018**, *39*, 1517–1530.

[8] I. Cukrowski, D. M. E. van Niekerk, J. H. de Lange, *Struct. Chem.* **2017**, *28*, 1429–1444.

[9] J. H. de Lange, D. M. E. van Niekerk, I. Cukrowski, *J. Comput. Chem.* **2018**, *39*, 973–985.

[10] J. H. de Lange, I. Cukrowski, *J. Comput. Chem.* **2017**, *38*, 981–997.

[11] D. L. Cooper, J. H. de Lange, R. Ponec, *Theor. Chem. Acc.* **2020**, *139*, 1–14.

[12] J. Cioslowski, *Int. J. Quantum Chem.* **1990**, *38*, 015–028.

[13] M. Chou, C. Creutz, N. Sutin, *J. Am. Chem. Soc.* **1977**, *99*, 5615–5623.

[14] R. A. Marcus, *Rev. Mod. Phys.* **1993**, *65*, 599–610.

[15] Q. Wang, Y. Li, P. Song, R. Su, F. Ma, Y. Yang, **n.d.**, DOI 10.3390/polym9120692.

[16] R. L. Du, K. Wu, D. A. Xu, C. Y. Chao, L. Zhang, X. D. Du, *Fuel Process. Technol.* **2016**, *148*, 295–301.

[17] H. Zhou, Y. Wang, F. Wei, D. Wang, Z. Wang, *Appl. Catal. A Gen.* **2008**, *348*, 135–141.

[18] T. Liu, A. Troisi, *J. Phys. Chem. C* **2011**, *115*, 2406–2415.

[19] P. Song, Y. Li, F. Ma, T. Pullerits, M. Sun, *J. Phys. Chem. C* **2013**, *117*, 15879–15889.

[20] T. Liu, A. Troisi, *Adv. Mater.* **2013**, *25*, 1038–1041.

[21] J. Zheng, Y. K. Kang, M. J. Therien, D. N. Beratan, *J. Am. Chem. Soc.* **2005**, *127*, 11303–11310.

[22] R. J. Cave, M. D. Newton, *Chem. Phys. Lett.* **1996**, *249*, 15–19.

[23] Y. Zhao, W. Liang, *Chem. Soc. Rev.* **2012**, *41*, 1075–1087.

[24] A. A. Voityuk, N. Rösch, *J. Chem. Phys.* **2002**, *117*, 5607–5616.

[25] Q. Wu, T. Van Voorhis, *Phys. Rev. A - At. Mol. Opt. Phys.* **2005**, *72*, DOI 10.1103/PhysRevA.72.024502.

[26] G. Horowitz, *Adv. Mater.* **1998**, *10*, 365–377.

[27] R. Marcus, N. S.-B. et B. A. (BBA)-R. on, undefined 1985, *Elsevier* **n.d.**

[28] M. D. Newton, N. Sutin, *Annu. Rev. Phys. Chem.* **1984**, *35*, 437–480.

© University of Pretoria

Chapter 3 – A theoretical framework to study the relationship between electron delocalization and ionization potential in organic electron donors

Stefan L. Koning, Jurgens H. de Lange*

Department of Chemistry, Faculty of Natural and Agricultural Sciences, University of Pretoria, Lynnwood Road, Hatfield, Pretoria 0002, South Africa

*Correspondence to: Jurgens de Lange

E-mail: jurgens.delange@up.ac.za

Abstract

Ionization potentials (IPs) is a fundamental and ubiquitous chemical concept, and the specific tuneability of IPs is important in the design of novel materials involving electron transfers. Beyond investigation of frontier molecular orbitals, interpreting and quantifying IPs in terms of chemical concepts – such as electron delocalization and resonance – can be difficult for complex molecules. In this theoretical case study, we apply the recently developed Fragment, Atomic, Localized, Delocalized and Interatomic (FALDI) density decomposition scheme to the problem of IPs in a series of small, aromatic molecules. We have found strong correlations of IPs and inter-fragment electron delocalization between a phenyl group and pnictogenic functional groups, suggesting that IPs decrease as electron delocalization increase. FALDI allows for exact quantification and visualization of electron (de)localization in an atomistic manner, thereby allowing us to trace the origin of IP changes to a hyperconjugative mechanism.

Keywords: Ionization potentials; electron transport; electron delocalization; quantum chemistry; FALDI

Introduction

The ionization potential (IP) of an atom or molecule – defined as the energy required to remove an electron from it – is a central parameter dictating a wide range of physical and chemical processes. It is an intricate part of photovoltaics[1], electrochemistry[2], spectroscopy[3],

© University of Pretoria

nucleophilicity[4], electron transfer mechanics[5], etc. It is therefore an entity worthwhile to have fine control over to meet optimal requirements for various physical systems.

Trends of atoms' IPs across the periodic table are well-established and taught at undergraduate level. For molecules, however, understanding the relationship between molecular and electronic structure and a molecule's IP is considerably more difficult. Even the well-known Koopman's theorem[6] which relates the IP of a molecule to the eigenvalue of the highest occupied molecular orbital (HOMO) in a set of canonical molecular orbitals (MOs) – cannot provide adequate *chemical* information regarding trends of molecular IPs. Rather, interpretation of IPs in terms of frontier MOs delegates the task to that of interpreting MOs, which becomes exceedingly difficult and fraught with misinterpretations as molecular complexity grows.[7–9]

Quantum Chemical Topology (QCT)[10] is an emerging field of theoretical chemical research which aims to explain and predict chemical phenomena through the topological analysis of various fields, with the electron density distribution, $\rho(\mathbf{r})$, as the most explored field. In this paper we apply a recently developed QCT approach towards explaining the origin of the ionization potential of organic molecules. It is proposed that a close correlation between electron delocalization and the ionization potential of organic molecules exists. To our knowledge, this has never been demonstrated before. Specifically, we will investigate a series of organic molecules which classically is expected to exhibit increasingly larger degrees of electron delocalization due to conjugative and hyperconjugative effects.

For dealing with electron delocalization, we first provide a brief background on the electronic structure of a molecule, as obtained from a recent review[11]. Lewis structures was one of the first concepts describing the role of electrons in a molecule. This construct is very limited in that it does not describe delocalization, as all electrons are considered localized in a bond ('first-order' interactions) or on an atom (core electrons and lone pairs). It does not describe the underlying quantum nature of molecules which are intrinsically delocalized quantum objects. Incorporating delocalization into the Lewis structure approach can be seen as a 'second-order' correction of this description as the quantum nature is then accounted for (however, a correction is only necessary when starting with an incomplete description). The delocalization interactions are classified into three types of ubiquitous effects: conjugation, hyperconjugation and σ-conjugation. Conjugation is essentially some form and degree of

© University of Pretoria

delocalization, thus giving a full description and quantification of the one will therefore describe and quantify the other.

The concept of conjugation is familiar and need no introduction, however hyperconjugation is less heard of. The IUPAC definition for hyperconjugation is the interaction of σ- and π-orbitals.[11] Within the classification of hyperconjugation there are various types, from which it appears as if hyperconjugation is well defined with discrete classifications within itself (for a more elaborate explanation of each type the reader is referred to the recent review on hyperconjugation[11]). However, the distinction between conjugation and hyperconjugation is in reality nothing more than artificial – they describe the same fundamental phenomena and only differ in the participation of σ- and or π- orbitals.[11] Therefore, despite these qualitatively defined types, hyperconjugation and all of its classifications really is a poorly defined range in a continuum of interactions of which 'normal' conjugation is also part of. This presents a challenge as there cannot be assigned a discrete label to each delocalizing interaction within a molecule, as is regularly done in classical chemistry. Quantification of delocalization seems more logical, but this has never been a simple task.

In past research there were numerous attempts to describe and quantify (hyper)conjugation (delocalization therefore) using geometry, energy, and magnetic criteria[12–19]. Most of these tools have significant shortcomings and with them all at hand it is still admitted that the quantification of (hyper)conjugation is rather challenging.[12] It was concluded by some authors[19] that there is no measure of aromaticity that can be applied universally. With aromaticity being a special case of delocalization (and more readily analysed due to geometric, energetic, and magnetic properties) it should be clear that there is no measure of delocalization that can readily be applied to any system. This problem stems from the inherent philosophical differences the holistic nature of the electronic wavefunction and the reductionist construction of the molecular structure hypothesis.[20][21]

With electron delocalization hard to quantify it is not surprising that there are few cases in literature where a correlation between delocalization and physical properties are established. With that said, we here implement the recently developed Fragment, Atomic, Localized, Delocalized and Interatomic (FALDI) electron density decomposition scheme. FALDI can quantify and visualize electron (de)localization in an atomistic manner, thereby recovering non-local electron correlation effects stemming from the molecular-wide wavefunction in a typically chemical, reductionist construction. It is extremely useful for isolating the effect that

© University of Pretoria

one atom or fragment has on the electronic structure of a molecule and allows to study the rearrangement thereof after ionization. It presents an intriguing approach to study the intricacies of systems such as delocalization and all its peculiarities and is therefore ideal for revealing the origin of physical properties of a molecule such as the ionization potential.

Theoretical Background

The Fragment, Atomic, Localized, Delocalized and Interatomic (FALDI) density decomposition scheme[22–25] provides the contributions arising from various atom- or fragment-(de)localized electrons to any coordinate **r**. In this manner, FALDI presents an atomistic investigation of an electronic structure whilst still retaining the holistic, molecular-wide nature of the wavefunction.

FALDI builds on concepts introduced by Domain Average Fermi Holes (DAFH) by Ponec and co-workers.[26–28] It primarily uses atomic basins as defined by the Quantum Theory of Atoms in Molecules (QTAIM),[29] as well as the Müller approximation[30] to define pseudo-second order electron density distributions. A short description of some of the various FALDI terms follows below.

The contribution to the electron density (ED) at **r** of the electrons found, on average, within an atomic basin Ω_A is known as an *atom*–ED distribution,

$$g_A(\mathbf{r}) = \sum_{ij} \sqrt{\nu_i \nu_j}\chi_i^*(\mathbf{r})\chi_j(\mathbf{r})S_{ji}^A \quad (1)$$

where χ is a molecular orbital (MO) with occupation ν and S_{ji}^A is an element of an atomic overlap matrix (AOM) associated with Ω_A,

$$S_{ij}^A = \int_{\Omega_A} \chi_i^*(\mathbf{r})\chi_j(\mathbf{r})d\mathbf{r} \quad (2)$$

Note that $g_A(\mathbf{r})$ is non-zero even when **r** is outside the atomic volume, $\mathbf{r} \notin \Omega_A$. $g_A(\mathbf{r})$ takes into account the averaged, (de)localized distribution of electrons found within Ω_A. In fact, integrating $g_A(\mathbf{r})$ over the entire molecular space yields the QTAIM-defined electron population of atom A, $\int g_A(\mathbf{r})d\mathbf{r} = N(A)$ and gives a count of the number of electrons found, on average, within Ω_A. Of considerably more import to us, however, is a measure and visualization of the electrons localized within Ω_A or delocalized amongst a basin-pair, Ω_A-Ω_B.

© University of Pretoria

FALDI provides this through atom-localized and atom-pair-delocalized distributions. The former, known as *loc*–ED distributions, calculate the contribution to the ED at **r** arising from electron-pairs localized to Ω_A:

$$\mathcal{L}_A(\mathbf{r}) = \sum_{ij}^{N_{MO}} \sqrt{\nu_i \nu_j}\chi_i^*(\mathbf{r})\chi_j(\mathbf{r})\left(\mathbf{S}^A\mathbf{S}^A\right)_{ji} \tag{3}$$

where $\mathbf{S}^A\mathbf{S}^A$ is the matrix product of the AOM associated with Ω_A, eqn. 2. Integrating $\mathcal{L}_A(\mathbf{r})$ over all molecular space yields the QTAIM-defined Localization Index (LI), $\mathrm{LI(A)} = Tr\left(\boldsymbol{\nu}^{\frac{1}{2}}\mathbf{S}^A\mathbf{S}^A\boldsymbol{\nu}^{\frac{1}{2}}\right) = \int \mathcal{L}_A(\mathbf{r})d\mathbf{r}$, and provides a count of the total number of electron-pairs localized to atom A. Similarly, the contribution to the ED at **r** arising from electron-pairs fully delocalized between two atomic basins are known as *deloc*–ED distributions,

$$\mathcal{D}_{A,B}(\mathbf{r}) = \sum_{ij}^{N_{MO}} \sqrt{\nu_i \nu_j}\chi_i^*(\mathbf{r})\chi_j(\mathbf{r})\left(\mathbf{S}^A\mathbf{S}^B + \mathbf{S}^B\mathbf{S}^A\right)_{ji} \tag{4}$$

Again, integrating $\mathcal{D}_{A,B}(\mathbf{r})$ over all molecular space yields the QTAIM-defined Delocalization Index (DI), $\mathrm{DI(A,B)} = Tr\left(\boldsymbol{\nu}^{\frac{1}{2}}(\mathbf{S}^A\mathbf{S}^B + \mathbf{S}^B\mathbf{S}^A)\boldsymbol{\nu}^{\frac{1}{2}}\right) = \int \mathcal{D}_{A,B}(\mathbf{r})d\mathbf{r}$. Note that both LIs and DIs correspond to an *electron* count of associated *electron-pairs*, and hence are additive to the total atomic electron population, $N(\mathrm{A}) = \mathrm{LI(A)} + \sum_{B\neq A}\frac{1}{2}\mathrm{DI(A,B)}$.

We have previously noted[23] that *loc*–ED distributions are generally somewhat delocalized over other atoms. That is, $\mathcal{L}_A(\mathbf{r}) \neq 0$ when $\mathbf{r} \notin \Omega_A$. This suggests that LIs, while physically exact, describe both a portion of core (fully localized) and valence (partially localized) electron-pairs. We introduced[23] the *localized-overlap* (LO) algorithm which removes any overlap between *loc*–ED distributions of different atoms. The resulting LO-free *loc*–ED distributions,

$$\mathcal{L}'_A(\mathbf{r}) = \sum_{i}^{N_{MO}} n'^{AA}_i\left[\phi^{AA}_i(\mathbf{r})\right]^2 \tag{5}$$

where $n'^{AA}_i\left[\phi^{AA}_i(\mathbf{r})\right]^2$ is a natural density function composed of eigenvectors of $\mathbf{S}^A\mathbf{S}^A$ with modified occupation n'^{AA}_i, provide a distribution of electrons which are exclusively localized to a single atomic basin. Integrating $\mathcal{L}'_A(\mathbf{r})$ over all space yields an LO-free localization index, $\mathrm{LI_{LO}(A)}$ that describes only core and non-bonded electrons. The result of the LO algorithm is

© University of Pretoria

generally much smaller LIs and larger DIs that correspond to the number of *electrons* shared, rather than the number of *electron-pairs*. Unlike orthodox QTAIM-defined DIs, LO-free DIs does not represent equal sharing of electrons. Specifically, each atom can contribute differently to the total inter-atomic DI, $\mathrm{DI(A,B)} = \mathrm{DI^A(A,B)} + \mathrm{DI^B(A,B)}$, with $\mathrm{DI^A(A,B)} \neq \mathrm{DI^B(A,B)}$ (however, in symmetric cases these may still be equal). Note that all *loc*–ED and *deloc*–ED distributions (as well as corresponding LIs and DIs) reported in this work are LO-free, and we will therefore drop corresponding accents for simplification.

Finally, we will utilize fragment ED distributions almost exclusively throughout this work. A fragment is defined in the FALDI scheme as a set of atomic basins, $\mathcal{F}$ = {A, B, C…} and $\Omega_{\mathcal{F}} = \sum \Omega_{\mathrm{A}}$. As a result, we can define a number of fragment-specific FALDI terms, starting with the total fragment contribution to the ED at **r**,

$$g_{\mathcal{F}1}^{\mathrm{total}}(\mathbf{r}) = \sum_{\mathrm{A}\in\mathcal{F}1} g_{\mathrm{A}}(\mathbf{r}) \tag{6}$$

$g_{\mathcal{F}1}^{\mathrm{total}}(\mathbf{r})$, when integrated over all space, yields the total fragment electron population or as $N(\mathcal{F}) = \sum_{\mathrm{A}\in\mathcal{F}1} N(\mathrm{A})$. Note that $N(\mathcal{F}_1)$ describes both electrons localized to the fragment as well as a contribution of electrons shared between other fragments.

The atom-localized contributions from each fragment, which with the LO-free algorithm generally only includes core and non-bonded electrons, can be summed to provide a fragment *loc*–ED distribution,

$$\mathcal{L}_{\mathcal{F}1}(\mathbf{r}) = \sum_{\mathrm{A}\in\mathcal{F}1} \mathcal{L}_{\mathrm{A}}(\mathbf{r}) \tag{7}$$

and integrated over all space to give fragment localization index, $\mathrm{LI}(\mathcal{F}_1)$. On the other hand, electrons delocalized amongst atoms within the fragment provide an intra-fragment *deloc*–ED distribution,

$$\mathcal{D}_{\mathcal{F}1}^{intra}(\mathbf{r}) = \sum_{\mathrm{A,B}\in\mathcal{F}1} \mathcal{D}_{\mathrm{A,B}}(\mathbf{r}) \tag{8}$$

and corresponding intra-fragment delocalization index, $\mathrm{DI}(\mathcal{F}_1,\mathcal{F}_1)$, after integration over all space. Similarly, the ED shared between atoms of different fragments can be summed to give an inter-fragment *deloc*–ED distribution,

© University of Pretoria

$$\mathcal{D}^{inter}_{\mathcal{F}1,\mathcal{F}2}(\mathbf{r}) = \sum_{A\in\mathcal{F}1}\sum_{B\in\mathcal{F}2}\mathcal{D}_{A,B}(\mathbf{r}) \quad (9)$$

and corresponding inter-fragment delocalization index, DI($\mathcal{F}_1$,$\mathcal{F}_2$). Note again that the contributions of each fragment to the inter-fragment DI is not necessarily equal, $\mathrm{DI}(\mathcal{F}_1,\mathcal{F}_2) = \mathrm{DI}^{\mathcal{F}_1}(\mathcal{F}_1,\mathcal{F}_2) + \mathrm{DI}^{\mathcal{F}_2}(\mathcal{F}_1,\mathcal{F}_2)$, with $\mathrm{DI}^{\mathcal{F}_1}(\mathcal{F}_1,\mathcal{F}_2) \neq \mathrm{DI}^{\mathcal{F}_2}(\mathcal{F}_1,\mathcal{F}_2)$.

Putting equations 7–9 together relates the various intra- and inter-fragment (de)localization terms to the total fragment population, Eq. 6:

$$g^{total}_{\mathcal{F}1}(\mathbf{r}) = \mathcal{L}_{\mathcal{F}1}(\mathbf{r}) + \mathcal{D}^{intra}_{\mathcal{F}1}(\mathbf{r}) + \sum_{X\neq 1}\mathcal{D}^{inter,\mathcal{F}1}_{\mathcal{F}1,\mathcal{F}X}(\mathbf{r}) \quad (10)$$

or in terms of integrated electron populations, $N(\mathcal{F}_1) = \mathrm{LI}(\mathcal{F}_1) + \mathrm{DI}(\mathcal{F}_1,\mathcal{F}_1) + \sum_{X\neq 1}\mathrm{DI}^{\mathcal{F}_1}(\mathcal{F}_1,\mathcal{F}_X)$. That is, the population of the fragment is equal to atom-localized electrons of atoms of the fragment, electrons delocalized within atoms of the fragment and a contribution to electrons delocalized with other fragments.

Computational Methods

All calculations were performed using the Gaussian 09 package[31] with density functional theory (DFT) method[32], CAM-B3LYP level of theory and augmented cc-pVDZ basis set. Atomic overlap matrices were calculated using the AIMAll version 17.11.14[33]. FALDI data was calculated using in-house software[22–25] with the LO algorithm. FALDI isosurfaces were visualized using VMD version 1.9.3[34].

Results and Discussion

A set of small organic aromatic electron donors were selected, with amine and phosphine functional groups containing various alkyl groups – Scheme 3.1. Two different fragmentation schemes (for FALDI analysis) will be used; note however, that the fragmentation schemes do not involve breaking any bonds or utilizing unchemical radical reference states. Scheme 1a shows a 2-fragment scheme, with $\mathcal{F}_1$ containing atoms from the phenyl ring and $\mathcal{F}_2$ containing the amine– or phosphine– substituent. In the second scheme (Scheme 1b), $\mathcal{F}_2$ is further fragmented into two fragments, with $\mathcal{F}_{2a}$ containing the heteroatom (N or P) and $\mathcal{F}_{2b}$ containing H- or alkyl-chain groups to provide additional detail.

© University of Pretoria

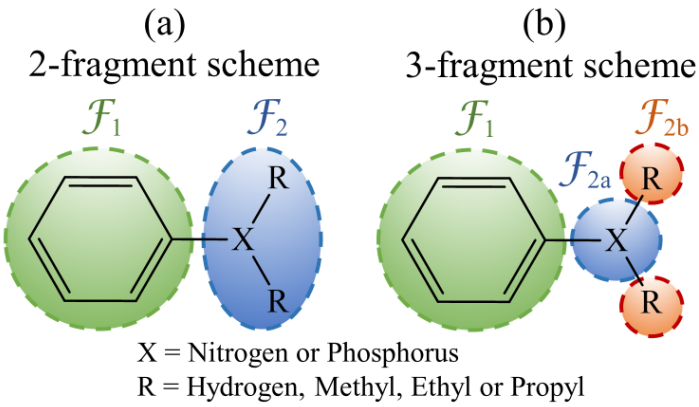

Scheme 3.1. Small organic electron donors utilized, with fragmentation schemes indicated.

In Table 3.1**,** the calculated ionization potentials (IPs) of the molecules are given with some experimental IPs for comparison. Note that cationic states were calculated at the same geometry as the neutral states to assist interpretation of FALDI data; however, no significant difference in calculated IPs was observed when using optimized cationic geometries – Table S3.1 of the SI. It can be noted that the IP trends is in accordance with available reported experimental values. A general trend is observed for the IPs in amine-substituted benzene: as the length of the R-groups increase from hydrogen through to propyl, the IP of the molecules decreases. The same trend is observed for phosphine-substituted molecules, although the calculated IPs are generally larger than for the amine-substituted molecules.

Table 3.1. Calculated IPs and some experimental IPs of the model- molecules.

Species	**IP (Hartree)**	**IP (eV)**	**Experimental IP (eV)**
Benzene	0.341	9.290	9.244[35]
Ph-NH_2	0.290	7.878	7.76[36], 7.720[35], 7.70[37]
Ph-NMe_2	0.266	7.251	7.44[36], 7.14[37]
Ph-NEt_2	0.256	6.975	6.99[36], 6.98[35]
Ph-NPr_2	0.254	6.901	-
Ph-PH_2	0.328	8.916	
Ph-PMe_2	0.300	8.159	-
Ph-PEt_2	0.294	8.012	
Ph-PPr_2	0.288	7.843	

FALDI-based distributions of delocalized density (*deloc*–ED distributions) between fragments $\mathcal{F}_1$ and $\mathcal{F}_2$ are presented in Figure 3.1 as well as the total number of these electrons

© University of Pretoria

shared between $\mathcal{F}_1$ and $\mathcal{F}_2$, (the inter-fragment delocalization or $DI_{GS}(\mathcal{F}_1,\mathcal{F}_2)$). $DI_{GS}(\mathcal{F}_1,\mathcal{F}_2)$ ranges from 3.955 e^- with PH_2 as substituent to 5.923 e^- with NPr_2 as substituent. Interestingly, these values are considerably larger than what would classically be expected and indicates the significance of long-range, non-covalent interactions between distant atoms of each fragment. This observation is evident when inspecting the isosurfaces of inter-fragment delocalized density in Figure 3.1. For instance, with NMe_2 as substituent (Figure 3.1b), the associated *deloc*–ED distribution is spread over the entire molecule at a reasonably large isovalue. The same is observed with NEt_2 (Figure 3.1c), and it is only with NPr_2 (Figure 3.1d) that the terminal methyl groups contribute noticeably fewer electrons.

Figure 3.1 also shows the change in inter-fragment delocalized density, $\Delta DI_{ion}(\mathcal{F}_1,\mathcal{F}_2)$, upon ionization of the molecule. These deformation density isosurfaces reveal that the C–X bonds are predominantly influenced upon ionization, with smaller changes distributed across the remainder of the molecule.

© University of Pretoria

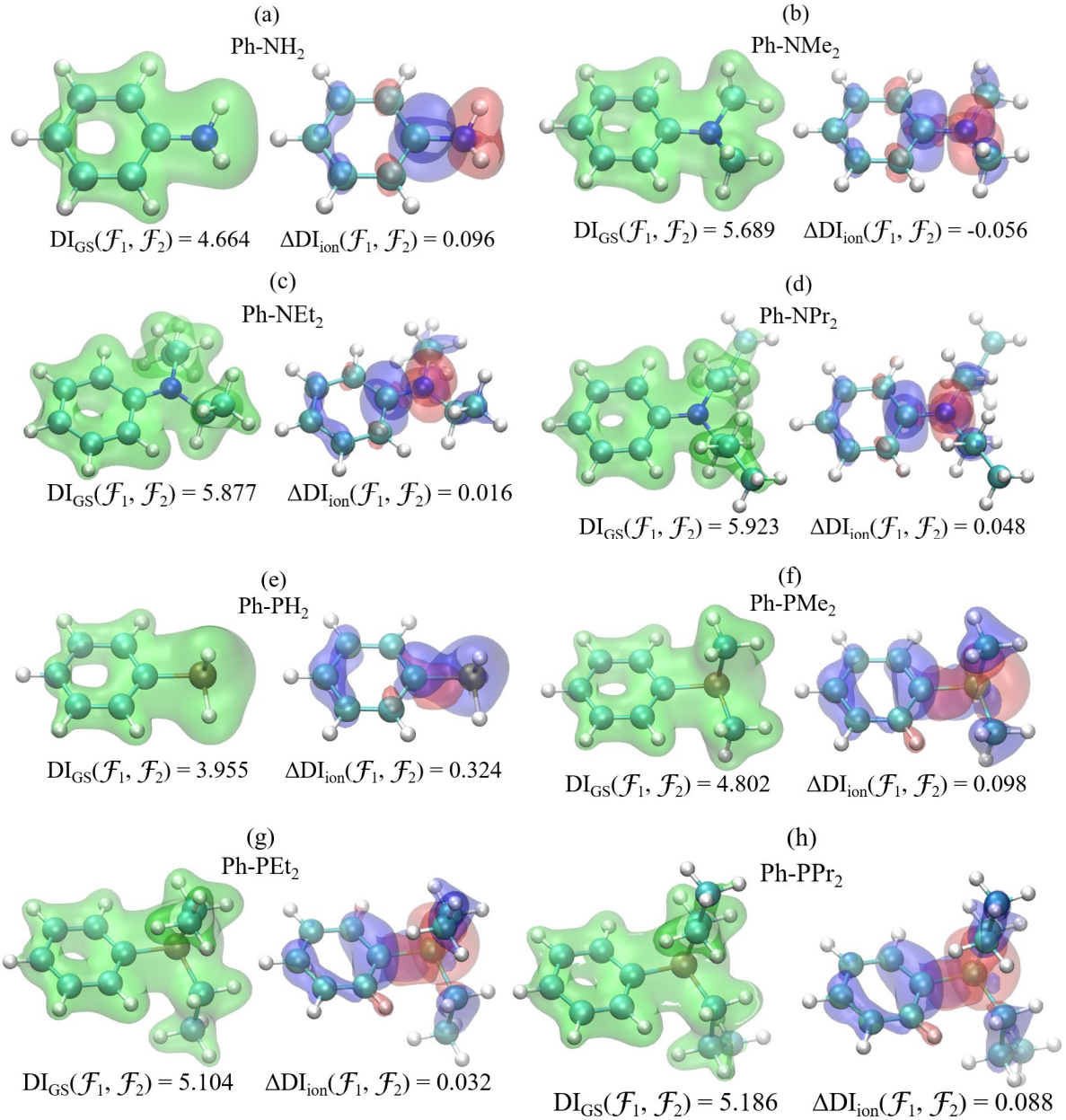

Figure 3.1. Isosurfaces of the interfragment *deloc*–ED distributions of the GS (green, iso = 0.0025) and the change thereof upon ionization (blue showing increase, red showing decrease, iso = 0.001).

A clear trend is apparent from the values of $DI_{GS}(\mathcal{F}_1,\mathcal{F}_2)$: an increase in the R-group alkyl chain length leads to increased inter-fragment electron delocalization, i.e. $DI_{GS}(\mathcal{F}_1,\mathcal{F}_2)$ increases with $NH_2 < NMe_2 < NEt_2 < NPr_2$. The same trend is observed for X = P, although $DI_{GS}(\mathcal{F}_1,\mathcal{F}_2)$ is generally lower than when X = N. A strong relationship was discovered between this inter-fragment electron delocalization and the IP – Figure 3.2 (X = N) and Figure 3.3 (X = P). These trends therefore reveal that the number of electrons shared between the

© University of Pretoria

aromatic ring and the amine/phosphine substituent (molecular delocalization) are highly correlated with the IP. Less energy is required to remove an electron if there are more electrons delocalized between phenyl and substituent. While not an unintuitive result, it is (to our knowledge) the first time that such a quantitative correlation between these two properties have been demonstrated. Datapoints indicating how the inter-fragment electron delocalization shifts upon ionization is also given in Figures 3.2 and 3.3.

Given the important role that the IP plays in determining electron transfer rates (via the Marcus equation[5]), the trends revealed in Figures 3.2 and 3.3 suggest a very attractive variable to study in order to provide more control in the rational design of organic electron donors. The remainder of this work will focus on an in-depth investigation of the origin and tuneability of the inter-fragment electron delocalization in the systems studied.

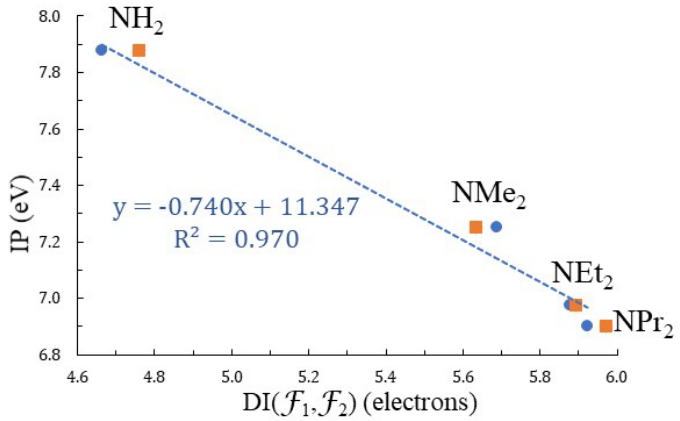

Figure 3.2. IP vs interfragment *deloc*–ED for the GS (blue, dotted trendline, circular datapoints) and cationic state (orange, square datapoints) of Ph-NR_2.

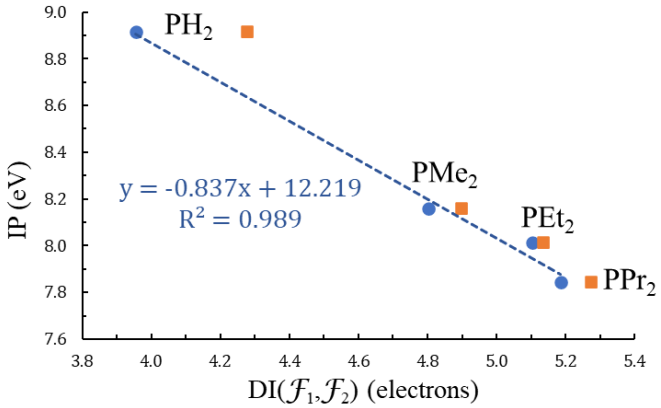

Figure 3.3. IP vs interfragment *deloc*-ED for the GS (blue, dotted trendline, circular datapoints) and cationic state (orange, square datapoints) of Ph-PR_2.

© University of Pretoria

Table 3.2. Electron population per fragment for Ph-NR_2 molecules

	Ph-NH_2			Ph-NMe_2			Ph-NEt_2			Ph-NPr_2		
Fragment	**Phenyl-**	**-N-**	**-H_2**	**Phenyl-**	**-N-**	**-Me_2**	**Phenyl-**	**-N-**	**-Et_2**	**Phenyl-**	**-N-**	**-Pr_2**
Total $N(\mathcal{F})$	40.634	8.218	1.148	40.672	8.132	17.196	40.676	8.155	33.169	40.677	8.158	49.165
Localized $\mathrm{LI_{GS}}(\mathcal{F})$	11.980	3.157	0	11.976	2.018	3.988	11.975	1.999	7.984	11.974	1.999	11.979
Intra-delocalized $\mathrm{DI_{GS}}(\mathcal{F},\mathcal{F})$	26.973	-	0.023	26.388	-	10.186	26.231	-	21.888	26.149	-	33.811
Inter-delocalized $\mathrm{DI}_{\mathrm{GS}}^{\mathcal{F}}(\mathcal{F},\mathcal{F}_X)$	1.680	5.061	1.125	2.309	6.114	3.022	2.470	6.156	3.297	2.553	6.159	3.374

© University of Pretoria

Analysis of (de)localization patterns in Ph-NR$_2$

The total fragment electron populations, $N(\mathcal{F})$, of the ground-state amine-substituted benzene molecules with varying alkyl chain lengths (Ph–NR$_2$, where R= –H, –Me, –Et and –Pr) are shown in Table 3.2. The changes in the electron populations of the phenyl fragment and nitrogen atom ($N(\mathcal{F}_1)$ and $N(\mathcal{F}_{2a})$, respectively) are quite small as the alkyl chain length increases and indicates that little formal charge-transfer occurs. Table 3.2 also shows the FALDI-based decomposition of $N(\mathcal{F})$ into atom-localized electrons (fragment localization index, LI($\mathcal{F}$)), intra-fragment shared electrons (intra-fragment delocalization index, DI$_{GS}(\mathcal{F},\mathcal{F})$) and the contribution of a fragment to inter-fragment shared electrons (partial inter-fragment delocalization index, $\mathrm{DI}_{\mathrm{GS}}^{\mathcal{F}}(\mathcal{F},\mathcal{F}_X)$. Note that large changes in most of the FALDI decomposition terms are observed for the R-fragment due to a variable number of atoms and can therefore not be compared directly. Interestingly, while the atom-localized electrons of the phenyl fragment remain relatively constant and close to the classically-expected number of core 1*s* electrons (LI($\mathcal{F}_1$) ~ 11.98 e^- for 6 occupied 1*s* orbitals), the localized electrons of the nitrogen atom changes quite dramatically: LI($\mathcal{F}_{2a}$) = 3.157 e^- in Ph-NH$_2$, 2.018 e^- in Ph-NMe$_2$ and 1.999 e^- in Ph-NEt$_2$ and Ph-NPr$_2$. This result indicates that the lone-pair on N is fully delocalized over the rest of the molecule when R = Et or Pr, but most localized when R = H. Furthermore, intra-fragment delocalized density of the phenyl fragment decreases significantly when the alkyl chain is increased: $\Delta\mathrm{DI}_{GS}(\mathcal{F}_1,\mathcal{F}_1)$ = –0.585 e^- in Ph-NMe$_2$, –0.742 e^- in Ph-NEt$_2$ and –0.824 e^- in Ph-NPr$_2$, all relative to Ph-NH$_2$. On the other hand, the number of electrons that the phenyl fragment shares with the rest of the molecule increases: $\Delta\mathrm{DI}_{\mathrm{GS}}^{\mathcal{F}_1}(\mathcal{F}_1,\mathcal{F}_X)$ = +0.629 e^- in Ph-NMe$_2$, +0.790 e^- in Ph-NEt$_2$ and +0.873 e^- in Ph-NPr$_2$. Similar increases are observed for the contributions to inter-fragment delocalized density from the nitrogen atom and R-group fragments as well. Therefore, while little formal charge transfer occurs as the alkyl chain lengthens, a considerable increase in inter-fragment delocalized electrons is seen. Table 3.2 reveals that the origin of these delocalized electrons is predominantly from the nitrogen atom's lone-pair and the electrons delocalized within the aromatic phenyl ring.

Table 3.3 lists the specific inter-fragment delocalization indices for all fragment-pairs in Ph-NR$_2$ molecules. Note that the delocalization indices (DI$_{GS}(\mathcal{F}_A,\mathcal{F}_B)$) includes the delocalization between all atom-pairs of fragments A and B. For instance, DI$_{GS}(\mathcal{F}_1, \mathcal{F}_{2a})$ = 4.360 e^- in Ph-NH$_2$, and includes both the covalent C–N bond as well as all long-range C···N and H···N

© University of Pretoria

interactions involving the remainder of the phenyl ring. This value shows that the total interaction between Ph and N in Ph-NH_2 involves slightly more than 2 electron-pairs.

Table 3.3. Inter-fragment delocalised density for Ph-NR_2 molecules

	Fragments		Inter-fragment delocalised ED, $DI_{GS}(\mathcal{F}_A, \mathcal{F}_B)$	$DI_{GS}(\mathcal{F}_1, \mathcal{F}_2)$
Ph-NH_2	-N-	-H_2	3.203	4.664
	Phenyl-	-N-	4.360	
	Phenyl-	-H_2	0.304	
Ph-NMe_2	-N-	-Me_2	5.756	5.689
	Phenyl-	-N-	4.039	
	Phenyl-	-Me_2	1.650	
Ph-NEt_2	-N-	-Et_2	6.046	5.877
	Phenyl-	-N-	3.756	
	Phenyl-	-Et_2	2.121	
Ph-NPr_2	-N-	-Pr_2	6.164	5.923
	Phenyl-	-N-	3.664	
	Phenyl-	-Pr_2	2.258	

Several interesting trends can be observed from the data in Table 3.3. The number of electrons shared between the nitrogen atom and R-group is $DI_{GS}(\mathcal{F}_{2a}, \mathcal{F}_{2b})$ = 3.203 e^- in Ph-NH_2 , indicating that each N–H bond shares fewer than a single electron pair. However, increasingly more electrons are shared between these fragments as the alkyl-length increases: $\Delta DI(\mathcal{F}_{2a}, \mathcal{F}_{2b})$ = +2.553 e^- in Ph-NMe_2, +2.843 e^- in Ph-NEt_2 and +2.961 in Ph-NPr_2, relative to Ph-NH_2. In fact, in Ph-NPr_2 a total of 6.164 e^- are shared between the nitrogen atom and the propyl groups, indicating that each N–Pr interaction shares considerably more than a single electron pair. A similar trend is seen for the long-range and non-covalent interactions between Ph and R-group fragments. In Ph-NH_2, $DI(\mathcal{F}_1,\mathcal{F}_{2b})$ is at a minimum of 0.304 e^- – a fraction of an electron pair shared. $DI(\mathcal{F}_1,\mathcal{F}_{2b})$ increases by +1.346 e^- in Ph-NMe_2 and +1.954 in Ph-NPr_2, relative to Ph-NH_2. The total number of electrons shared in Ph-NPr_2 between the phenyl group and the distant R-groups are therefore 2.258 e^- – slightly more than a complete electron pair. It is therefore clear that the long-range, non-covalent interactions present with alkyl-substituted amine groups are significantly larger than what would classically be expected. Finally, the number of electrons delocalized between the nitrogen atom and the phenyl group *decreases* with increasing alkyl chain length: $\Delta DI(\mathcal{F}_1, \mathcal{F}_{2a})$ = –0.321 e^- in Ph-NMe_2, –0.604 e^- in Ph-

© University of Pretoria

NEt_2 and –0.696 in Ph-NPr_2, relative to Ph-NH_2. This result is also somewhat unexpected, but it is reasonable to infer that as both the phenyl fragment and nitrogen atom share more electrons with the R-groups (as the alkyl chain-length increases), fewer electrons are available to delocalize between the phenyl fragment and nitrogen atom.

The origin of the total inter-fragment delocalization observed earlier ($DI_{GS}(\mathcal{F}_1,\mathcal{F}_2)$, Figures 3.1 and 3.2) is therefore quite clear: as the alkyl chain-length increases, some of the electrons delocalized within the aromatic phenyl ring ($DI_{GS}(\mathcal{F}_1,\mathcal{F}_1)$, Table 3.2) becomes preferentially shared with the alkyl R-groups in a long-range, non-covalent fashion ($DI_{GS}(\mathcal{F}_1,\mathcal{F}_{2b})$, Table 3.3). Despite the decrease in electron delocalization between the phenyl ring and the nitrogen atom ($DI_{GS}(\mathcal{F}_1,\mathcal{F}_{2a})$, Table 3.3), $DI_{GS}(\mathcal{F}_1,\mathcal{F}_2)$ still increases which emphasises the strength of the phenyl R-group interaction.

The chemical nature of these effects can be ascribed to inductive donation from the alkyl groups, hyperconjugation or a combination of both. However, since very little formal charge transfer was observed ($N(\mathcal{F})$, Table 3.2), and given the strong long-range interactions observed between the phenyl ring and the R-groups, the trends discussed above is very likely due to increasing hyperconjugation with increasing alkyl chain-length.

When an electron is removed from the Ph-NH_2 system (Table S3.6 in the SI) to form the cationic state, most of the removed electron originates from the phenyl ring ($\Delta_{ion}N(\mathcal{F}_1)$ = –0.718 e^-). When the H-atoms are substituted for alkyl groups, fewer electrons are removed from the phenyl ring and more from the R-groups ($\Delta_{ion}N(\mathcal{F}_1)$ = –0.552 e^- and $\Delta_{ion}N(\mathcal{F}_{2b})$ = –0.345 e^- in Ph-NPr_2). In addition, it is primarily the electrons delocalized within the Ph fragment that is removed ($\Delta_{ion}DI(\mathcal{F}_1,\mathcal{F}_1)$ = –0.802 e^- in Ph-NH_2 and –0.623 in Ph-NPr_2). Regardless of the origin of the removed electron upon ionization, the general trends in electron (de)localization remain the same in the cationic state as for the ground state. Tables S3.2 and S3.3 in the SI show the intra- and inter-fragment electron populations for the Ph-NR_2 systems in their cationic states. As the alkyl chain-length increases, i) more electrons are delocalized between the N-atom and the R-groups, ii) more electrons are delocalized in the long-range interactions between the Ph-ring and the R-groups, and iii) fewer electrons are delocalized between the Ph-ring and the N-atom. Therefore, as is also seen in Figure 3.2, ionization to the cationic state of Ph-NR_2 systems does not seem to meaningfully impact the general

© University of Pretoria

(de)localization of electrons; rather, the cationic state seems to be electron-poor in intra-fragment electrons delocalized within the Ph-ring or within alkyl chains.

In summary, our FALDI results suggest that the apparent correlation between IP and inter-fragment electron delocalization (Figure 3.2) in Ph-NR_2 systems is likely the result of increasing hyperconjugation with increased alkyl chain-length. However, the mechanism of this effect is quite surprising: rather than strengthening the Ph–N bond, increased hyperconjugation results in a large strengthening of the long-range Ph···R interactions. Upon ionization, the majority of the electron is removed from intra-fragment delocalized densities of the Ph-ring and alkyl chains. Therefore, our results suggest that less energy is required to ionize Ph-NR_2 molecules (i.e. lower IP) as more electrons are delocalized between the Ph-ring and alkyl chains.

Analysis of Ground state (de)localization patterns in Ph-XR_2

We noted above (Table 3.1, Figure 3.1) that when the nitrogen atom is replaced by phosphorus in Ph-XR_2 molecules, a general increase in IP and decrease in inter-fragment delocalization was observed. Tables S3.5 and S3.7 in the SI contains the ground-state FALDI populations for intra- and inter-fragment (de)localization in Ph-PR_2 molecules. For the most part, the trends observed with increasing alkyl chain length is very similar for X = P and N. Below, we will briefly analyse and highlight specific differences between the two molecule sets.

Table 3.4 collects the ground state FALDI fragment populations of Ph-PR_2 molecules, relative to the corresponding Ph-NR_2 molecules. Replacing N with P adds 8 core electrons to the system; indeed, $LI_{GS}(\mathcal{F}_{2a})$ is generally 8 e^- higher with X = P than N. However, the valence electron distribution amongst the various fragments is significantly different for X = P. The total number of shared, valence electrons found on the heteroatom is significantly less when X = P relative to N; for instance, $\Delta DI_{GS}^{\mathcal{F}_{2a}}(\mathcal{F}_{2a}, \mathcal{F}_X) = -3.130$ e^- in Ph-PMe_2, relative to Ph-NMe_2. These electrons were transferred to the neighbouring Ph and R-groups, as a corresponding increase is observed primarily in intra-fragment delocalized ED; e.g. $\Delta DI_{GS}(\mathcal{F}_1, \mathcal{F}_1) = +0.867$ e^- and $\Delta DI_{GS}(\mathcal{F}_{2b}, \mathcal{F}_{2b}) = +1.479$ e^- in Ph-PMe_2, relative to Ph-NMe_2. As a result, the total fragment electron populations of the Ph and R-groups increase significantly when N is replaced with P. It is clear, therefore, that replacing nitrogen with the heavier phosphorus atom in Ph-

© University of Pretoria

XR_2 systems results in a large degree of charge transfer from P to the rest of the molecule. This effect seems to be generally constant with increasing alkyl chain-length.

© University of Pretoria

Table 3.4. Electron population change from X = N to P for Ph-XR_2 molecules

	Ph-XH_2			Ph-XMe_2			Ph-XEt_2			Ph-XPr_2		
Fragment	**Phenyl-**	**-X-**	**-H_2**	**Phenyl-**	**-X-**	**-Me_2**	**Phenyl-**	**-X-**	**-Et_2**	**Phenyl-**	**-X-**	**-Pr_2**
Total $\Delta N(\mathcal{F})$	0.925	5.114	1.961	0.929	5.172	1.898	0.918	5.189	1.892	0.922	5.186	1.892
Localized $\Delta \mathrm{LI}_{\mathrm{GS}}(\mathcal{F})$	0.002	7.625	0.000	0.005	8.302	0.009	0.005	8.152	0.009	0.006	8.011	0.009
Intra-delocalized $\Delta \mathrm{DI}_{\mathrm{GS}}(\mathcal{F},\mathcal{F})$	0.708	-	0.227	0.867	-	1.479	0.827	-	1.621	0.844	-	1.668
Inter-delocalized $\Delta \mathrm{DI}_{\mathrm{GS}}^{\mathcal{F}}(\mathcal{F},\mathcal{F}_X)$	0.216	-2.511	1.734	0.056	-3.130	0.410	0.085	-2.964	0.261	0.072	-2.824	0.216

© University of Pretoria

Replacing X = N with P also has an effect on the manner through which electrons are delocalized amongst fragments of the molecules – Table 3.5. Ph-PR_2 systems generally have significantly less electrons shared between the X-atom and both, the phenyl fragment and R-groups, than Ph-NR_2 systems. On the other hand, the long-range interaction between Ph and R-groups are strengthened in the presence of a phosphorus relative to a nitrogen atom. The latter change in inter-fragment delocalization is, however, less than the former, resulting in a general decrease in delocalization between Ph and its substituent. For instance, the P-atom and phenyl fragment in Ph-PPr_2 share $\Delta DI_{GS}(\mathcal{F}_1, \mathcal{F}_{2a})$ = –1.140 fewer electrons than the N-atom and Ph does in Ph-NPr_2. However, Ph and the propyl groups only share $\Delta DI_{GS}(\mathcal{F}_1, \mathcal{F}_{2b})$ = +0.404 e^- more when X = P than when X = N, resulting in a net decrease in inter-fragment delocalized ED of $\Delta DI_{GS}(\mathcal{F}_1, \mathcal{F}_2)$ = –0.737 e^-. Given the correlations observed above between the IP and inter-fragment electron delocalization (Figures 3.2 and 3.3), it is likely that the general higher IPs of Ph-PR_2 systems than Ph-NR_2 systems is also a result of decreased inter-fragment electron delocalization observed when X = P.

Table 3.5. Inter-fragment delocalised density change from X = N to P for Ph-XR_2 molecules

Molecule	**Fragments**		$\Delta DI_{GS}(\mathcal{F}_A, \mathcal{F}_B)$	$\Delta DI_{GS}(\mathcal{F}_1, \mathcal{F}_2)$
Ph-XH_2	-X-	-H_2	0.147	-0.709
	Phenyl-	-X-	-1.752	
	Phenyl-	-H_2	1.043	
Ph-XMe_2	-X-	-Me_2	-1.777	-0.887
	Phenyl-	-X-	-1.463	
	Phenyl-	-Me_2	0.576	
Ph-XEt_2	-X-	-Et_2	-1.844	-0.773
	Phenyl-	-X-	-1.233	
	Phenyl-	-Et_2	0.460	
Ph-XPr_2	-X-	-Pr_2	-1.799	-0.737
	Phenyl-	-X-	-1.140	
	Phenyl-	-Pr_2	0.404	

Ionization Analysis

Being more familiar with the behaviour of the electronic structure of the ground state, we now focus on the effects of the removal of an electron.

When a molecule is ionized by removal or addition of an electron, the change in ED is not uniform throughout. This is apparent in Table 3.6 where the removal of an electron is quantified by measuring the change in fragment electron populations. In Ph-NH_2, the majority of the

© University of Pretoria

removed electron originates from the phenyl fragment, $\Delta_{ion}N(\mathcal{F}_1) = -0.718\ e^-$. Replacing R = H with R = Me/Et/Pr shifts the removal of an electron more towards the functional group, e.g. $\Delta_{ion}N(\mathcal{F}_2) = -0.447\ e^-$ in Ph-NPr$_2$.. When X=P a similar trend is seen as for X=N, but more electrons are removed from the functional groups, e.g. $\Delta_{ion}N(\mathcal{F}_2) = -0.679\ e^-$ in Ph-PPr$_2$.

Table 3.6. Change in ED on the indicated fragment ($\Delta_{ion}N(\mathcal{F})$) when an electron is removed from the molecule (static geometry)

	Ph-NR$_2$		Ph-PR$_2$	
R-group	**Phenyl-**	**-NR$_2$**	**Phenyl-**	**-PR$_2$**
H	-0.718	-0.281	-0.644	-0.355
Methyl	-0.583	-0.417	-0.395	-0.605
Ethyl	-0.564	-0.435	-0.326	-0.672
Propyl	-0.552	-0.447	-0.321	-0.679

Change in inter-fragment delocalization upon ionization is visualised in Figure 3.1 and tabulated in Table 3.7. In general, for most combinations of X-atoms and R-groups, ionization leads to i) a decrease in electrons shared between the X-atom and R-groups, $\Delta_{ion}DI(\mathcal{F}_{2a},\mathcal{F}_{2b})$ and ii) an increase in long-range delocalization of electrons between the phenyl fragment and the R-groups.

It should be noted again, however, that the vast majority of the removed electron upon cationization originates from intra-fragment, rather than inter-fragment delocalized ED. For instance, intra-fragment delocalization of Ph decreases by $\Delta_{ion}DI(\mathcal{F}_1,\mathcal{F}_1) = -0.623\ e^-$ in Ph-NPr$_2$ and of the propyl groups by $\Delta_{ion}DI(\mathcal{F}_{2b},\mathcal{F}_{2b}) = -0.334\ e^-$, Table S3.6 in the SI. Therefore, it seems that the observed increase in inter-fragment delocalization with longer alkyl-chain lengths facilitates removal of an electron from both the phenyl fragment and the alkyl R-groups.

© University of Pretoria

Table 3.7. Inter-fragment delocalised density change upon ionization for Ph-XR_2 molecules

Fragments		$\Delta_{ion}DI(\mathcal{F}_A, \mathcal{F}_B)$ X = N		$\Delta_{ion}DI(\mathcal{F}_A, \mathcal{F}_B)$ X = P	
-X-	**-H_2**	-0.385		-0.154	
Phenyl-	**-X-**	0.154	**0.096**[#]	0.303	**0.324**
Phenyl-	**-H_2**	-0.057		0.022	
-X-	**-Me_2**	-0.379		-0.056	
Phenyl-	**-X-**	-0.077	**-0.056**	0.022	**0.098**
Phenyl-	**-Me_2**	0.022		0.076	
-X-	**-Et_2**	-0.346		-0.108	
Phenyl-	**-X-**	-0.049	**0.016**	-0.034	**0.032**
Phenyl-	**-Et_2**	0.065		0.066	
-X-	**-Pr_2**	-0.237		-0.136	
Phenyl-	**-X-**	-0.016	**0.048**	-0.065	**0.088**
Phenyl-	**-Pr_2**	0.064		0.153	

[#]$DI(\mathcal{F}_1, \mathcal{F}_2) = DI(\mathcal{F}_1, \mathcal{F}_{2a}) + DI(\mathcal{F}_1, \mathcal{F}_{2b})$

From our analyses of the electronic structures of both ground and cationic states of the Ph-XR_2 systems, it is clear that the general trends with increasing alkyl chain-lengths are present in both ground and cationic states (Table 3.7 as well as Table S3.2, S3.3 and S3.6 in SI). With respect to the change in interfragment delocalized density upon ionization, none of the variables in Table 3.7 were found to correlate significantly with the IPs of the molecules – despite strong trends observed between $DI(\mathcal{F}_1, \mathcal{F}_2)$ of both the ground and cationic states with IP (Figures 3.1 and 3.2). Therefore, removing an electron from a Ph-XR_2 molecule seems to be predominantly dependent on the interfragment delocalized density of the ground or cationic state itself, rather than the change between the two states.

Conclusion

The energy required for the ionization of a molecule – whether to an anion or a cation – is a critically important quantity in many chemical and physical processes. Finding fundamental and quantifiable chemical arguments to predict or understand ionization potentials allows for precise tuneability and improved material design. In this work we have shown that the FALDI electron decomposition scheme can be used to explore IPs for a set of substituted benzene molecules. Through FALDI we have identified a tentative link between electron delocalization and IPs for a set of substituted benzene molecules.

© University of Pretoria

We have found a strong correlation between the delocalization of electrons between benzene and its substituents and the IP – as the inter-fragment electron delocalization increases the IP decreases. Inter-fragment electron delocalization increased as alkyl chain-lengths in Ph-XR_2 lengthened. We furthermore pinpointed the origin of the observed delocalization changes to increasing long-range delocalization between the phenyl-ring and alkyl chains despite decreasing number of electrons shared between the phenyl-ring and nitrogen/phosphorus atoms. Due to very little formal charge-transfer observed when the alkyl chains were lengthened, we conclude that the increase in long range Ph···R_2 delocalization is due to increased hyperconjugation as opposed to an inductive effect. When the nitrogen atom was replaced by a phosphorus atom, the IP was observed to increase and – in line with our hypothesis – a decrease in inter-fragment electron delocalization was observed.

The FALDI scheme allows for an in-depth, atomistic description of the molecular electronic structure of both ground and cationic states, as well as the electronic structure change upon ionization. Using FALDI, we could therefore trace the origin of the removed electron when Ph-XR_2 molecules are ionized. Specifically, we found that the electron is primarily removed from the electrons delocalized *within* the phenyl-ring in Ph-XH_2, and after alkyl substitution it is removed from electrons delocalized *within* phenyl as well as the R-groups. Given the observed correlation between inter-fragment electron delocalization and IP, it is therefore plausible to suggest that the long-range delocalization between the phenyl ring and alkyl groups facilitates removal of an electron from the fragments themselves.

Based on our observations, we therefore suggest the following: as more electrons are shared between the phenyl ring and its substituent due to hyperconjugation, an electron can be more easily removed from both phenyl ring and the substituent. Consequently, the IP is lowered. Future studies on this phenomenon will hopefully reveal whether our hypothesis is specific to Ph-XR_2 molecules or generalizable to a larger set of molecular systems.

Finally, it is clear that FALDI analysis have a tremendous ability to understand and investigate ionization in an orbital-free, atomistic manner. While our focus is primarily on photophysical processes related to photosensitizers, we expect that FALDI will prove its insightful capacity to various other phenomena that occur in the realm of physical chemistry.

© University of Pretoria

Acknowledgements

The authors would like to acknowledge the University of Pretoria for financial support.

Conflict of Interest

The authors would like to declare no conflict of interest.

References

[1] C. Wang, L. Ouyang, X. Xu, S. Braun, X. Liu, M. Fahlman, *Sol. RRL* **2018**, *2*, 1800122.

[2] S. Janietz, D. D. C. Bradley, M. Grell, C. Giebeler, M. Inbasekaran, E. P. Woo, *Appl. Phys. Lett.* **1998**, *73*, 2453–2455.

[3] S. Rothe, A. N. Andreyev, S. Antalic, A. Borschevsky, L. Capponi, T. E. Cocolios, H. De Witte, E. Eliav, D. V. Fedorov, V. N. Fedosseev, D. A. Fink, S. Fritzsche, L. Ghys, M. Huyse, N. Imai, U. Kaldor, Y. Kudryavtsev, U. Köster, J. F. W. Lane, J. Lassen, V. Liberati, K. M. Lynch, B. A. Marsh, K. Nishio, D. Pauwels, V. Pershina, L. Popescu, T. J. Procter, D. Radulov, S. Raeder, M. M. Rajabali, E. Rapisarda, R. E. Rossel, K. Sandhu, M. D. Seliverstov, A. M. Sjödin, P. Van Den Bergh, P. Van Duppen, M. Venhart, Y. Wakabayashi, K. D. A. Wendt, *Nat. Commun.* **2013**, *4*, 1–6.

[4] P. Jaramillo, L. R. Domingo, E. Chamorro, P. Pérez, *J. Mol. Struct. THEOCHEM* **2008**, *865*, 68–72.

[5] R. A. Marcus, *Rev. Mod. Phys.* **1993**, *65*, 599–610.

[6] T. Koopmans, *Physica* **1934**, *1*, 104–113.

[7] R. D. Hancock, I. V. Nikolayenko, *J. Phys. Chem. A* **2012**, *116*, 8572–8583.

[8] Y. Liu, B. Liu, Y. Liu, M. G. B. Drew, *ACS Publ.* **2011**, *89*, 355–359.

[9] J. Murrell, S. Kettle, J. Tedder, *The Chemical Bond*, Wiley-VCH, New York, **1985**.

[10] P. L. A. Popelier, S. Bond, *Springer* **2016**, *170*, 71–118.

[11] I. V. Alabugin, G. dos Passos Gomes, M. A. Abdo, *Wiley Interdiscip. Rev. Comput. Mol. Sci.* **2019**, *9*, DOI 10.1002/wcms.1389.

[12] J. F. Gonthier, S. N. Steinmann, M. D. Wodrich, C. Corminboeuf, *Chem. Soc. Rev.* **2012**, *41*, 4671–4687.

[13] S. E. Wheeler, K. N. Houk, P. V. R. Schleyer, W. D. Allen, *J. Am. Chem. Soc.* **2009**, *131*, 2547–2560.

[14] M. D. Wodrich, C. S. Wannere, Y. Mo, P. D. Jarowski, K. N. Houk, P. Von Ragué Schleyer, *Chem. - A Eur. J.* **2007**, *13*, 7731–7744.

[15] F. Weinhold, C. R. Landis, E. D. Glendening, *Int. Rev. Phys. Chem.* **2016**, *35*, 399–

© University of Pretoria

440.

[16] L. Zhao, M. von Hopffgarten, D. M. Andrada, G. Frenking, *Wiley Interdiscip. Rev. Comput. Mol. Sci.* **2018**, *8*, DOI 10.1002/wcms.1345.

[17] Y. Mo, L. Song, Y. Lin, *J. Phys. Chem. A* **2007**, *111*, 8291–8301.

[18] P. von Ragué Schleyer, *Chem. Rev.* **2005**, *105*, 3433–3435.

[19] J. Poater, M. Duran, M. Solà, B. Silvi, **2005**, DOI 10.1021/cr030085x.

[20] P. Schuster, *Berichte Der Bunsengesellschaft Für Physikalische Chemie*, Wiley-VCH, Berlin, Heidelberg, New York, **1982**.

[21] J. C. A. Boeyens, *Int. J. Mol. Sci.* **2010**, *11*, 4267–4284.

[22] I. Cukrowski, D. M. E. van Niekerk, J. H. de Lange, *Struct. Chem.* **2017**, *28*, 1429–1444.

[23] J. H. de Lange, I. Cukrowski, *J. Comput. Chem.* **2018**, *39*, 1517–1530.

[24] J. H. de Lange, D. M. E. van Niekerk, I. Cukrowski, *J. Comput. Chem.* **2018**, *39*, 973–985.

[25] J. H. de Lange, I. Cukrowski, *J. Comput. Chem.* **2017**, *38*, 981–997.

[26] R. Ponec, *J. Math. Chem.* **1997**, *21*, 323–333.

[27] R. Ponec, *J. Math. Chem.* **1998**, *23*, 85–103.

[28] D. L. Cooper, J. H. de Lange, R. Ponec, *Theor. Chem. Acc.* **2020**, *139*, 1–14.

[29] R. Bader, T. Nguyen-Dang, *Adv. Quantum Chem.* **1981**, *14*, 63–124.

[30] A. Müller, *Phys. Lett. A* **1984**, *105*, 446–452

[31] Gaussian 16, Revision C.01, M. J. Frisch, G. W. Trucks, H. B. Schlegel, G. E. Scuseria, M. A. Robb, J. R. Cheeseman, G. Scalmani, V. Barone, G. A. Petersson, H. Nakatsuji, M. C. , X. Li, A. Marenich, J. Bloino, B. G. Janesko, R. Gomperts, B. Mennucci, H. P. Hratchian, J. V. Ortiz, A. F. Izmaylov, J. L. Sonnenberg, D. Williams-Young, F. Ding, F. Lipparini, F. Egidi, J. Goings, B. Peng, A. Petrone, T. Henderson, D. Ranasinghe, V. G. Zakrzewski, J. Gao, N. Rega, G. Zheng, W. Liang, M. Hada, M. Ehara, K. Toyota, R. Fukuda, J. Hasegawa, M. Ishida, T. Nakajima, Y. Honda, O. Kitao, H. Nakai, T. Vreven, K. Throssell, J. A. Montgomery, J. E. Peralta, F. Ogliaro, M. Bearpark, J. J. Heyd, E. Brothers, K. N. Kudin, V. N. Staroverov, T. Keith, R. Kobayashi, J. Normand, K. Raghavachari, A. Rendell, J. C. Burant, S. S. Iyengar, J. Tomasi, M. Cossi, J. M. Millam, M. Klene, C. Adamo, R. Cammi, J. W. Ochterski, R. L. Martin, K. Morokuma, O. Farkas, J. B. Foresman, D. J. Fox, **2016**.

[32] W. Koch, M. C. Holthausen, *A Chemist's Guide to Density Functional Theory*, Wiley-VCH, **2001**.

[33] T. A. Keith, AIMAll (version 19.10.12); TK Gristmill Software: Overland Park KS, USA, **2019**.

[34] W. Humphrey, A. Dalke, K. Schulten, *J. Mol. Graph.* **1996**, *14*, 33–38.

[35] J. Hager, M. A. Smith, S. C. Wallace, *J. Chem. Phys.* **1985**, *83*, 4820–4822.

© University of Pretoria

[36] P. G. Farrell, J. Newton, *Tetrahedron Lett.* **1966**, *7*, 5517–5523.

[37] "The National Institute for Occupational Safety and Health (NIOSH)," can be found under https://www.cdc.gov/niosh/npg/npgd0033.html, **2019**.

© University of Pretoria

Table of Contents

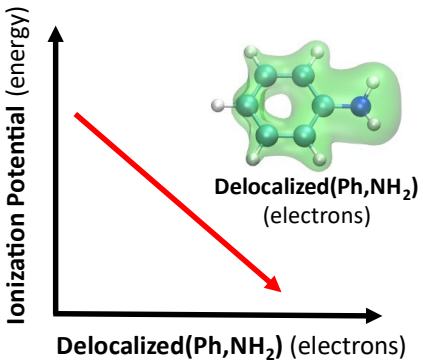

The relationship between ionization potentials (IPs) of a series of aromatic organic molecules and interfragment electron delocalization is investigated. The Fragment, Atomic, Localized, Delocalized and Interatomic (FALDI) density decomposition scheme reveals that IPs decrease as more electrons are delocalized between a phenyl group and a pnictogen functional group.

© University of Pretoria

Chapter 4 –Electron density, delocalization, and electron attachment of organic electron acceptors

Introduction

The electron affinity (EA), defined as the energy difference between a neutral atom or molecule and its corresponding anion, is a property of great importance in chemistry. Generally, the electron affinity is the energy released when an electron is introduced into a molecular system and therefore reflects the ability of a system to bind an electron. A high electron affinity therefore implies a large amount energy released, a strongly bound electron and often a spontaneous electron attachment process. However, for the sake of avoiding confusion and promote the easy comparability of values, the electron affinity, also referred to here as the electron attachment energy, is calculated like the ionization potential. In our results it therefore gives the energy required to add an electron to some moiety instead of energy released as is the conventional use of the electron affinity.

There are many areas in chemistry,[1–4] including material science and even environmental chemistry[5] where negative ions are important. Electron affinities play a role in areas such as the chemistry of silicon,[6] quantum dot semiconductor chemistry,[7] fullerene chemistry,[8–10] polymer photoluminescence,[11] Schottky diodes,[12] etc. The electron attachment energy is also core to electron transfer dynamics. In Marcus theory[13], the theory describing the rate of electron transfer between a donor and acceptor moiety, the electron attachment energy is directly linked to the calculation of the charge transfer rate constants. Therefore, it would be worthwhile to understand how and to what extent this energy is altered when changes are made to a molecule. Fullerene derivatives are known to have a high electron affinity[14] and is, among other factors, one of the reasons it is such a successful electron acceptor in bulk heterojunction (BHJ) organic solar cells.

However, a large electron affinity is not necessarily predictive of fast electron transfer rates. In Marcus theory there exists a so called ‘inverted region’ in which strong thermodynamic drive – due to a favourable ΔG^0 – does not necessarily amount to a good rate constant. And ΔG^0 used in Marcus theory is usually calculated from the electron attachment energy, among other parameters. In other words, in order to maximize electron transfer rates we should know how to construct a molecule with a specific rather than maximum electron affinity. This is a somewhat ambitious idea as trying to find the perfect EA for some donor-acceptor pair through

© University of Pretoria

incremental variation would influence at least four other parameters in the Marcus equation. While such a ubiquitous and correlated study would be extremely insightful, it is beyond the scope of this chapter and thus we restrict ourselves to focussing solely on EA for now.

Trends of the EA of atoms have already been recognized across the periodic table and is well documented, but is considerably harder to predict for molecules. To our knowledge, any trends in EA that carry generalized predictive power have not been thoroughly investigated for molecules. However, assuming that objective relationships exist between chemical molecular structure and EA exists, a predictive model of EA for a subset of molecules will be extremely useful in the rational design of solar cells, complex electrocatalysts and other electron transfer systems. To accomplish this, we need to establish fundamental principles, which we believe can be established by finding the precise relationship between molecular and electronic structure and the electron attachment energy.

Quantum Chemical Topology (QCT)[15] is a field of theoretical chemistry which aims to explain chemical phenomena through topological analysis of various fields among which the electron density distribution is the most explored. The Fragment, Atom, Localized, Delocalized and Interatomic (FALDI) electron density decomposition scheme is a QCT approach used here for investigation of the origin of the electron attachment energy. Here we hypothesize that, in a small subset of small organic electron acceptors, that there exists a link between the electron delocalization and the electron attachment energy as well as between phenyl electron population and the electron attachment energy. While this hypothesis might be expected, to our knowledge this has never been documented nor quantified before.

With electron delocalization tough to quantify it is not as surprising that it is hard to find literature where a correlation between delocalization and physical properties are established. With that said, we here implement the recently developed FALDI electron density decomposition scheme for the study of EAs. FALDI can quantify and visualize electron (de)localization in an atomistic manner, thereby recovering non-local electron correlation effects stemming from the molecular-wide wavefunction in a typically chemical, reductionist construction. It is extremely useful for isolating the effect that one atom or fragment has on the electronic structure of a molecule and allows to study the rearrangement thereof after ionization. It presents an intriguing approach to study the intricacies of systems such as delocalization and all its peculiarities and is therefore ideal for revealing the origin of physical properties of a molecule such as the electron affinity.

© University of Pretoria

Computational Methods

All calculations were performed using the Gaussian 09 package[25] with density functional theory (DFT) method[26], CAM-B3LYP level of theory and augmented cc-pVDZ basis set. Atomic overlap matrices were calculated using the AIMAll version 17.11.14[27]. FALDI data was calculated using in-house software[28–31] with the LO algorithm. FALDI isosurfaces were visualized using VMD version 1.9.3[32]. For an overview and description of FALDI terms, please consult Chapter 2 and Chapter 3.

Results and Discussion

Two sets of small organic electron acceptors were investigated – a halogen substituted and nitroso- substituted set. The halogen series consists of three molecules: fluoro-, chloro- and bromobenzene. The nitroso- series consists of nitrosobenzene and three analogues in which a varying carbohydrate chain (R-group) separates the nitroso from the phenyl – Scheme 4.1.

For the Halogen series only a 2-fragment scheme is implemented for FALDI analysis; $\mathcal{F}_1$ consisting of all atoms in the Ph and $\mathcal{F}_2$ consisting only of the halogen (Scheme 4.1a). For the nitroso- series, however, two fragmentation schemes were used: i) A 2-fragment scheme in which $\mathcal{F}_1$ is the atoms of Ph and where $\mathcal{F}_2$ consists of all atoms in the substituted nitroso- group (RNO) and ii) a 3-fragment scheme where $\mathcal{F}_2$ is further divided into only the NO functionality ($\mathcal{F}_{2a}$) and the atoms of the R-group ($\mathcal{F}_{2b}$).

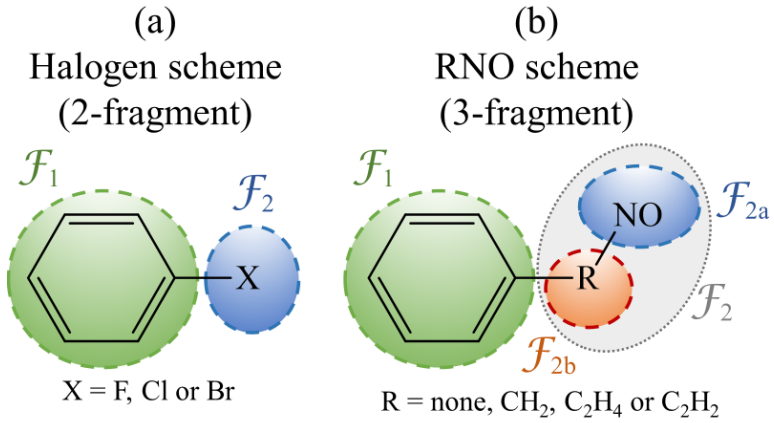

Scheme 4.1. Small organic electron acceptors utilized, with fragmentation schemes indicated.

© University of Pretoria

Calculated electron affinities (EAs) of these molecules are reported in Table 4.1. It should be noted here that these are not calculated the standard way. These do not represent the energy released when an electron is attached to a molecule, but the energy required to add the electron to the molecule. Also, like with the IP in Chapter 3, the vertical EA is computed; EA is obtained by taking the difference in energy between anionic state at neutral optimized geometry and the neutral state at that same geometry (eqn. 4.1). Again, this is done to allow more meaningful interpretations of the FALDI data.

$$EA = E(A^-) - E(A) \tag{4.1}$$

For the halogen-substituted molecules, energy is required to attach an electron (positive EA). However, heavier halogens decreases this energy, from 1.144 eV in Ph–F to 0.953 eV in Ph–Br. In the nitroso-substituted set, all EAs are negative (an electron is readily accommodated) but increases as the nitroso group is seperated with saturated alkyl groups from the phenyl ring. However, when the system conjugation is restored with an unsaturated alkyl chain, the EA returns to a more negative value. These molecules are simple enough that trends in EA can be explained qualitatively through concepts such as electronegativity, induction and conjugation. However, such explanations remain conjecture and speculative, in addition to be intrinsically unquantifiable.

Table 4.1. Calculated EAs of the small organic acceptors

Species	**EA (eV)**
Ph-F	1.144
Ph-Cl	1.032
Ph-Br	0.953
Ph-NO	-1.024
Ph-CH_2NO	-0.355
Ph-C_2H_4NO	-0.259
Ph-C_2H_2NO	-1.236

© University of Pretoria

In Figure 4.1 the *deloc*-ED distributions between fragments $\mathcal{F}_1$ and $\mathcal{F}_2$ are presented along with the integrated number of electrons involved – $DI_{GS}(\mathcal{F}_1,\mathcal{F}_2)$. Here $DI_{GS}(\mathcal{F}_1,\mathcal{F}_2)$ ranges from 3.432 – 3.881 e^- for the halogen set and for the nitroso- sunstituted set it ranges from 4.440 – 4.964 e^-. Here it is shown again, as in Chapter 3, how significant long-range interactions are. The *deloc*-ED distributions adds to this showing how $DI_{GS}(\mathcal{F}_1,\mathcal{F}_2)$ is spread across the entirety of the molecules; despite the non-conjugated alkyl chain of Ph-C_2H_4NO, $DI_{GS}(\mathcal{F}_1,\mathcal{F}_2)$ is reasonably distributed over most atoms of the systems – Figure 4.1f.

Figure 4.1 also displays the change in *deloc*-ED distributions and $DI_{GS}(\mathcal{F}_1,\mathcal{F}_2)$ upon addition of an electron – $\Delta DI_{ion}(\mathcal{F}_1,\mathcal{F}_2)$. When considering these distributions it is helpful to be reminded that these are not the total ED change, only the inter-fragment delocalization. In the halogen set there is little change with Ph-Cl having the largest at $\Delta DI_{ion}(\mathcal{F}_1,\mathcal{F}_2)$ = 0.039 e^-. However, in the nitroso-set the change in $DI_{GS}(\mathcal{F}_1,\mathcal{F}_2)$ is more significant with Ph-CH_2NO showing $\Delta DI_{ion}(\mathcal{F}_1,\mathcal{F}_2)$ = 0.996 e^-.

© University of Pretoria

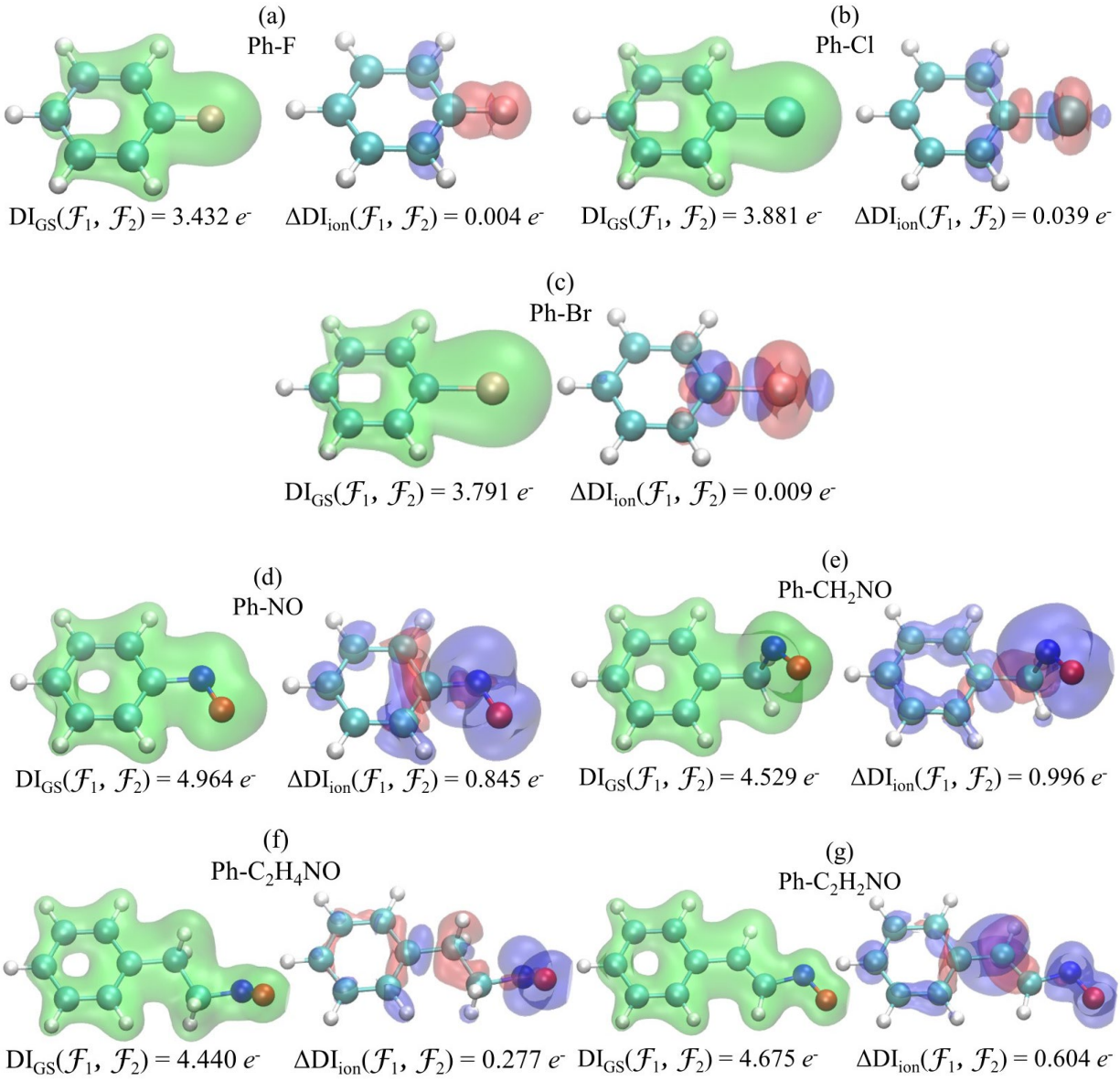

Figure 4.1. Isosurfaces of the interfragment *deloc*-ED of the GS (green, iso = 0.0025) and the change thereof upon ionization (blue showing increase, red showing decrease, iso = 0.001).

Change in inter-fragment delocalized ED upon selection of halogens does not follow a trend. Consequently, when compared to the EAs from Table 4.1, there seems to be no linear correlation between EA and $DI_{GS}(\mathcal{F}_1,\mathcal{F}_2)$ – Figure 4.2. While a trend with regard to EAs of halogens are expected, it is likely that additional halogens - such as iodine - need to be considered as well in order to rule out outliers. However, when considering nitrosobenzene with only its saturated alkyl derivatives, there do seem to be a trend. With increasing saturated alkyl chain length separation between Ph and NO the shared electrons goes down; $DI_{GS}(\mathcal{F}_1,\mathcal{F}_2)$ deceases with Ph-NO → Ph-CH_2NO → Ph-C_2H_4NO. When plotted with their corresponding

© University of Pretoria

EAs it follows a linear trend – Figure 4.3. As $DI_{GS}(\mathcal{F}_1,\mathcal{F}_2)$ increases, electron attachment will release more energy. The same but opposite trend was found for a series of molecules where the substituents of the phenyl are COH, COOH, COOMe and COOEt – see SI Figure S4.1. This is, to our knowledge, also the first time that a relationship between delocalization and electron affinity is revealed, even though it is only present in a specific subset of our dataset.

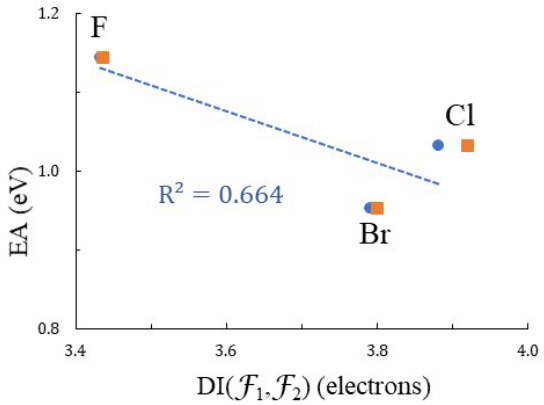

Figure 4.2. EA vs interfragment *deloc*–ED for the GS (blue, dotted trendline, circular datapoints) and anionic state (orange, square datapoints) of Ph-X

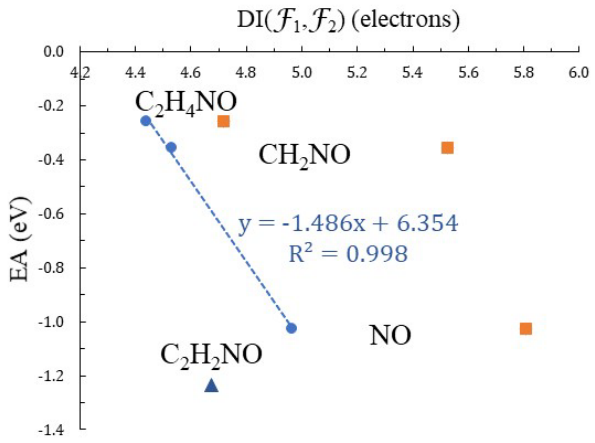

Figure 4.3. EA vs interfragment *deloc*–ED for the GS (blue, dotted trendline, circular datapoints) and anionic state (orange, square datapoints) of Ph-RNO

© University of Pretoria

Analysis of Ground State (de)localization patterns in Ph-X

Table 4.2. Electron population per fragment for Ph-X molecules in ground state

Fragment	Ph-F		Ph-Cl		Ph-Br	
	Phenyl-	**-F**	**Phenyl-**	**-Cl**	**Phenyl-**	**-Br**
Total $N(\mathcal{F})$	40.366	9.634	40.730	17.270	40.894	35.106
Localized $LI_{GS}(\mathcal{F})$	11.977	7.398	11.983	14.839	11.983	32.815
Intra-delocalized $DI_{GS}(\mathcal{F},\mathcal{F})$	27.193	-	27.297	-	27.411	-
Inter-delocalized $DI_{GS}^{\mathcal{F}}(\mathcal{F},\mathcal{F}_X)$	1.195	2.237	1.450	2.431	1.500	2.291
$DI_{GS}(\mathcal{F}_1, \mathcal{F}_2)$	3.432		3.881		3.791	

In Table 4.2 the total fragment electron populations, $N(\mathcal{F})$, are given for the halogen substituted set. Clearly $N(\mathcal{F}_1)$ is reduced in the presence of the halogens as 41 e^- are classically expected on Ph in the absence of electron withdrawing effects, but Ph-F has only 40.366 e^- on average on the phenyl-ring. This effect fades moving down the periodic table as would be expected. (Electron population data like that of Table 4.2 and 4.3 is also calculated for the two series of molecules of which the substituents are COH, COOH, COOMe and COOEt and OH, OMe and OEt, and is supplied in the SI – Tables S4.3 and S4.4)

The fragment population is further decomposed in its components: the localized ($LI_{GS}(\mathcal{F})$), intra- ($DI_{GS}(\mathcal{F},\mathcal{F})$) and partial inter-fragment delocalized ED ($DI_{GS}^{\mathcal{F}}(\mathcal{F},\mathcal{F}_X)$). The total inter-fragment delocalized ED is also given ($DI_{GS}(\mathcal{F}_1,\mathcal{F}_2) = DI_{GS}^{\mathcal{F}_1}(\mathcal{F}_1,\mathcal{F}_2) + DI_{GS}^{\mathcal{F}_2}(\mathcal{F}_1,\mathcal{F}_2)$) An unsubstituted benzene is expected to have 28$^-$ sp^2 intra-delocalized electrons; however, closer to 27 e^- is observed – $DI_{GS}(\mathcal{F}_1,\mathcal{F}_1)$ = 27.193 e^- for Ph-F. This suggests the electron withdrawing halogens have a strong pull on the valence electrons of benzene and is the primary reason for Ph being electron poor. Accordingly, phenyl's valence electrons are then delocalized between the phenyl ring and the halogen as the ED shared between the two fragments, $DI_{GS}(\mathcal{F}_1, \mathcal{F}_2)$, is quite high – $DI_{GS}(\mathcal{F}_1, \mathcal{F}_2)$ = 3.791 e^- for Ph-Br – almost 2 electron pairs. The phenyl-halogen interaction is therefore more comprehensive than a 1 electron pair covalent bond as classically represented.

© University of Pretoria

From Table 4.2, a portion of the halogens' lone pairs are also involved in this interaction. Classically, the number of core and lone pair electrons on F, Cl and Br would be 8, 16 and 34 e^-, respectively. Instead, we see 7.398, 14.839 and 32.815 e^-. For Ph-Br, this indicates that 1.185 e^- of Br's lone pair electrons are participating in bonding with Ph, which in classical chemistry terms is nothing but resonance. The resonance effect of the first three halogens has, therefore, essentially been quantified here with the resonance of in Ph-Br being at the order of 1.185 e^-.

Interestingly, $DI_{GS}(\mathcal{F}_1,\mathcal{F}_2)$ is the highest for when the phenyl is substituted with Cl – the halogen in the middle of the series. Like Br, Cl shares a significant amount of its lone pairs and $\mathcal{F}_1$ still contributes a high amount of its intra-delocalized ED towards $DI_{GS}(\mathcal{F}_1, \mathcal{F}_2)$, similar to F. This suggests that Cl has an optimal combination between being highly electron negative and having orbitals sufficiently sized to allow resonance to arrive at the highest degree of electron delocalization between the phenyl and the halogen. Furthermore, note how $DI_{GS}(\mathcal{F}_1, \mathcal{F}_2)$ is unequally divided between Ph and X due to the halogen being much more electron negative. For instance, in Ph–Br, the total number of electrons shared between the halogen and the entire phenyl ring is $DI_{GS}(\mathcal{F}_1, \mathcal{F}_2)$ = 3.791 e^-, but 2.291 e^- (60%) is contributed by Br whereas only 1.500 e^- (40%) is contributed by the phenyl ring.

In summary, the inductive, electron withdrawing and resonance effect of halogens could be retrieved and quantified by the FALDI decomposition scheme. The inductive effect is described as a portion of the intra-fragment delocalized density ($DI_{GS}(\mathcal{F}_1,\mathcal{F}_1)$) being converted into inter-fragment delocalized density ($DI_{GS}(\mathcal{F}_1,\mathcal{F}_2)$), meaning these electrons can be found on the halogen as well. Here the inductive effect is withdrawing due to the electron negative halogens. And the resonance is identified by the halogens contributing a significant amount of its localized density ($LI_{GS}(\mathcal{F}_2)$) to the inter-fragment delocalized density ($DI_{GS}(\mathcal{F}_1,\mathcal{F}_2)$) as well. As a result, the number of electrons shared between the phenyl and the halogen is far greater than the classically expected 2 e^-.

The above figures also show trends regarding the anionic states of the studied molecules. In general, for these curves and those that follow, the anionic state follows the ground state calculations qualitatively albeit with less linearity. Whether the loss of strong linear correlations is an artifact of the model will be investigated in future studies; the data is included here for comparison but will not be discussed in detail.

Analysis of Ground State (de)localization patterns in Ph-RNO

© University of Pretoria

Table 4.3 introduces the electron population per fragment and the decomposition thereof for the nitroso-substituted set. As Ph-NO does not have an alkyl group it has only two fragments. In this molecule, the electron population on Ph is depleted the most (within the nitroso-substituted set) as the absence of an alkyl interjection fully exposes the phenyl ring to the electron withdrawing power of NO; $N(\mathcal{F}_1) = 40.524\ e^-$ for Ph-NO. However, as the alkyl chain-length increases the population on the phenyl ring increases and thereby displaying formal charge-transfer – $N(\mathcal{F}_1) = 41.018\ e^-$ for Ph-C_2H_4NO. This is possibly due to the spatial separation of Ph and NO, and/or the inductive donating effect of alkyl chains.

© University of Pretoria

Table 4.3. Electron population per fragment for Ph-RNO molecules in ground state

Fragment	Ph-NO		Ph-CH_2NO			Ph-C_2H_4NO			Ph-C_2H_2NO		
	Phenyl-	**-NO**	**Phenyl-**	**-CH_2-**	**-NO**	**Phenyl-**	**-C_2H_4-**	**-NO**	**Phenyl-**	**-C_2H_2-**	**-NO**
Total $N(\mathcal{F})$	40.524	15.476	40.953	7.662	15.385	41.018	15.570	15.412	40.889	13.571	15.540
Localized $\mathrm{LI_{GS}}(\mathcal{F})$	11.980	8.510	11.981	1.996	8.553	11.981	3.993	8.586	11.982	3.992	8.673
Intra-delocalized $\mathrm{DI_{GS}}(\mathcal{F},\mathcal{F})$	26.698	3.847	26.971	3.011	3.937	26.917	8.383	3.934	26.790	6.048	3.790
Inter-delocalized $\mathrm{DI}^{\mathcal{F}}_{\mathrm{GS}}(\mathcal{F},\mathcal{F}_X)$	1.846	3.118	2.000	2.655	2.895	2.120	3.193	2.892	2.118	3.531	3.076

© University of Pretoria

Again, there is a significant number of electrons delocalized between $\mathcal{F}_1$ (phenyl ring) and $\mathcal{F}_2$ (entire alkylnitroso substituent) in all nitroso-substituted molecules. The source of these delocalized electrons is similar to that described in the halogen set – intra-fragment delocalized electrons from Ph and lone pair electrons from N and O. However, in this case there are even more electrons withdrawn from Ph's intra-fragment delocalized density; $DI_{GS}(\mathcal{F}_1,\mathcal{F}_1) = 26.698$ e^- for Ph-NO (classically 28 e^- are expected). As of the lone pairs: The number of electrons participating in the double bond between N and O is in all moieties close to the expected 4 e^- (intra-fragment delocalized density, $DI_{GS}(\mathcal{F}_{2a},\mathcal{F}_{2a})$). It can thus be assumed that the lone pairs of these heteroatoms are not participating in the N=O bond, conforming to the classical expectation. For Ph-NO, this allows the same conclusion as drawn as for the halogen set, which is that the missing localized electrons on $\mathcal{F}_2$ are lone pairs delocalized unto the phenyl ring. The high number of electrons shared between the phenyl ring and NO in Ph-NO ($DI_{GS}(\mathcal{F}_1,\mathcal{F}_2)$ = 4.964 e^- – Table 4.4) are possibly facilitated by the uninterrupted conjugated system of electrons present.

Table 4.4. Inter-fragment delocalized density for Ph-RNO molecules in ground state

Molecule	**Fragments**		**Inter-fragment delocalized ED, $DI_{GS}(\mathcal{F}_A, \mathcal{F}_B)$**	**$DI_{GS}(\mathcal{F}_1, \mathcal{F}_2)$**
Ph-NO	Phenyl-	-NO	4.964	
Ph-CH_2NO	-CH_2-	-NO	3.021	4.529
	Phenyl-	-NO	1.522	
	Phenyl-	-CH_2-	3.007	
Ph-C_2H_4NO	-C_2H_4-	-NO	3.764	4.440
	Phenyl-	-NO	0.715	
	Phenyl-	-C_2H_4-	3.725	
Ph-C_2H_2NO	-C_2H_2-	-NO	4.050	4.675
	Phenyl-	-NO	0.890	
	Phenyl-	-C_2H_2-	3.785	

However, for Ph-CH_2NO (methyl bridge) and Ph-C_2H_4NO (ethylene bridge) the situation is slightly different as NO does now not only interact with the phenyl but with the alkyl chain as well. Interestingly, the lone pairs of NO are still as much delocalized in these as with Ph-NO indicated by a similar number of missing localized electrons – $LI_{GS}(\mathcal{F}_{2a})$ = 8.553 e^- for Ph-CH_2NO. From Table 4.4, where the inter-fragment delocalized electron populations between

© University of Pretoria

the different fragments are given, a large number of electrons are shared between the alkyl bridges and nitroso groups: $\mathcal{F}_{2a}$ and $\mathcal{F}_{2b}$ – $DI_{GS}(\mathcal{F}_{2a},\mathcal{F}_{2b})$ = 3.764 e^- for Ph-C_2H_4NO (as opposed to a classically expected single, $2e^-$ bond). The lone pairs on nitroso therefore interact with the alkyl chains suggesting hyperconjugative interactions. Density shared between phenyl and NO, however, decreased rapidly with increasing alkyl chain length ($DI_{GS}(\mathcal{F}_1,\mathcal{F}_{2a})$ = 0.715 e^- for Ph-C_2H_4NO). These observations clearly suggest that the Ph···NO interaction competes with the hyperconjugative component of the alkyl–NO interaction. When the ethylene bridge is unsaturated (i.e. in Ph-C_2H_2NO), the long-range Ph···NO is slightly enhanced ($DI_{GS}(\mathcal{F}_1,\mathcal{F}_{2a})$ = 0.890 e^- for Ph-C_2H_2NO). The fully conjugated unsaturated chain also allowed more of the intra-fragment delocalized density of Ph to be delocalized and thereby partially restoring the NO character of the molecule as with Ph-NO ($DI_{GS}(\mathcal{F}_1,\mathcal{F}_1)$ = 26.790 e^- for Ph-C_2H_2NO). With increasing alkyl chain length the inter-fragment delocalized density, $DI_{GS}(\mathcal{F}_1,\mathcal{F}_2)$, decreased. However, the unsaturated fully conjugated system enhanced delocalization throughout the molecule, as all $DI_{GS}(\mathcal{F}_A, \mathcal{F}_B)$ terms increased relative to the saturated case– Table 4.4.

To summarize, the nitroso group was demonstrated to be very electron withdrawing – more so than fluorine. This electron withdrawing effect on the phenyl ring quickly weakened as the alkyl chain length of Ph-RNO increased. Also, as the chain length increased, the inter-fragment delocalized density between $\mathcal{F}_1$ and $\mathcal{F}_2$ decreased. As in Ph-NO, the lone pair electrons of NO are still significantly delocalized in Ph-CH_2NO and Ph-C_2H_4NO, suggesting hyperconjugative interactions between NO and the alkyl group. Compared to the saturated C_2 chain, the unsaturated chain slightly restores the electron withdrawing and delocalization effect as found in Ph-NO. Thereby, the difference between a fully conjugated and an interrupted conjugated system was demonstrated quantitatively.

Phenyl electron population vs Electron affinity and Ionization Analysis

In both sets of molecules, the electron populations on Ph ($N(\mathcal{F}_1)$ – Tables 4.2 and 4.3) follow a clear trend by progressing through the series of molecules. In the halogen-substituted set, the Ph electron population increases by substituting a halogen further down the periodic table. For the nitroso- set, Ph electron population increases with increasing R-group size. Here, another correlation was discovered – there is a relationship between the EA and the phenyl electron population, $N(\mathcal{F}_1)$. This is illustrated in Figures 4.4 and 4.5 where it shows that, for these small

© University of Pretoria

organic electron acceptors, the EA is strongly dependent on the electron population of Ph. To our knowledge, this is also the first time that such a correlation is represented quantitatively.

Interestingly the trends for the two sets of molecules are opposite. For the halogen-substituted set (Figure 4.4) when phenyl is more electron rich, less energy is required to attach an electron to the molecule. For every one extra electron on the phenyl ring, the EA seems to drop with 0.351 eV. This is somewhat counterintuitive and raises the question of where the added electron is localized within the molecule, and how the remaining electrons have been rearranged upon ionization. The electron density difference between the anionic and neutral states provides a mapping of both the localization of the added electron as well as rearrangement of the remaining electrons. If the density difference is predominantly localized to a region other than the phenyl ring it should not be as puzzling as coulombic repulsion can then be mitigated. In Table 4.5 the change in fragment electron populations upon introduction of an electron is given for the halogen set. In fluorobenzene the electron is almost exclusively added to the phenyl ring ($\Delta N(\mathcal{F}_1) = +0.953\ e^-$) while in bromobenzene the electron is much less added to the ring ($\Delta N(\mathcal{F}_1) = +0.789\ e^-$), suggesting that the larger bromine atom can more readily accommodate electron density and the excess density is slightly more delocalized. This lesser amount added to the more electron rich phenyl ring in bromobenzene is, therefore, sufficient to reduce the energy of electron attachment in Ph-Br relative to Ph-F. It should be noted that the EA energy range in Figure 4.4 is very narrow (~0.2 eV difference between Ph-Br and Ph-F) for the electron population range compared to that of the nitroso- set in Figure 4.5.

In the nitroso-substituted set, when the phenyl electron population is low, more energy is released (negative EAs) upon attachment of an electron than when the electron population is higher. This is in line with intuition. For every one electron the phenyl ring gains, EA will increase with 1.555 eV. This is a much steeper change compared to the halogen set, suggesting that these molecules are more sensitive to the phenyl electron population in terms of the EA. The release of energy instead of using energy – as in the halogen set, indicates that the nitroso set are better acceptors as it can spontaneously accept an electron. The unsaturated alkyl chain moiety – Ph-C_2H_2NO – does not conform to the trend as indicated on Figure 4.5.

© University of Pretoria

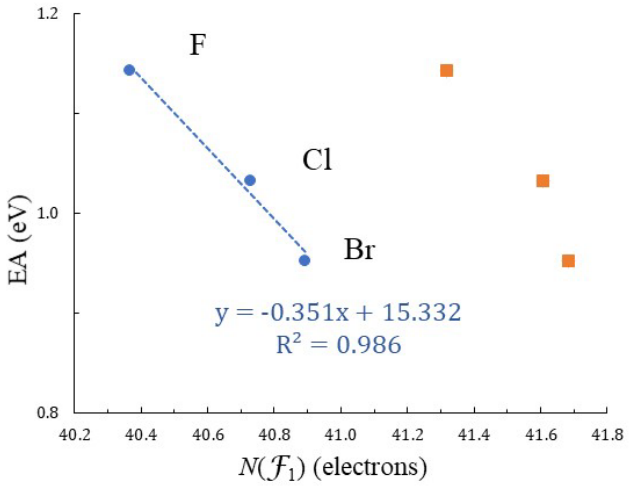

Figure 4.4. EA vs Total electron count on Ph for the GS (blue, dotted trendline, circular datapoints) and anionic state (orange, square datapoints) of Ph-X

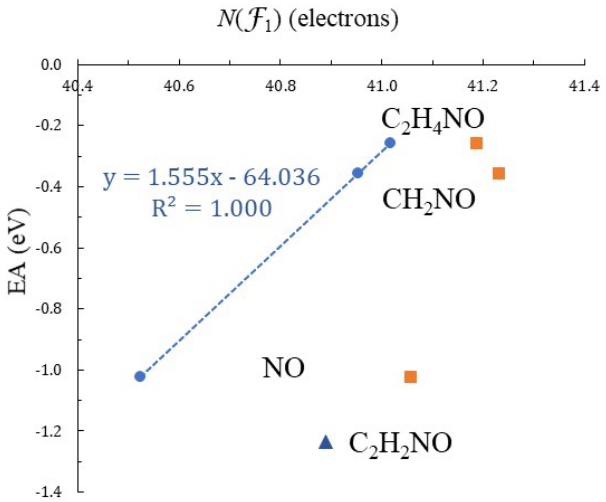

Figure 4.5. EA vs Total electron count on Ph for the GS (blue, dotted trendline, circular datapoints) and anionic state (orange, square datapoints) of Ph-RNO

© University of Pretoria

Table 4.5. Electron population *change* upon electron attachment for Ph-X molecules[#]

	Ph-F		Ph-Cl		Ph-Br	
Fragment	**Phenyl-**	**-F**	**Phenyl-**	**-Cl**	**Phenyl-**	**-Br**
Total $\Delta N(\mathcal{F})$	0.953	0.047	0.875	0.125	0.789	0.211
Localized $\Delta LI_{GS}(\mathcal{F})$	-0.002	0.069	-0.001	0.103	0.000	0.206
Intra-delocalized $\Delta DI_{GS}(\mathcal{F},\mathcal{F})$	0.929	-	0.859	-	0.786	-
Inter-delocalized $\Delta DI_{GS}^{\mathcal{F}}(\mathcal{F},\mathcal{F}_X)$	0.025	-0.022	0.017	0.022	0.003	0.005
$\Delta DI_{GS}(\mathcal{F}_1, \mathcal{F}_2)$	0.004		0.039		0.009	

[#]Anionic data is provided in the SI – Tables S4.1 and S4.2

In Table 4.6 and 4.7 the change in electron population of the fragments and of the inter-fragment electron population upon ionization is given, respectively. Initially with Ph-NO, the added electron is almost equally divided between Ph and NO – $\Delta N(\mathcal{F}_1) = +0.532\ e^-$ and $\Delta N(\mathcal{F}_2) = +0.468\ e^-$ (Table 4.6). With alkyl chains added, significantly less ED is added to the phenyl ring with the most added to NO – $\Delta N(\mathcal{F}_1) = +0.169\ e^-$ and $\Delta N(\mathcal{F}_{2a}) = +0.639\ e^-$ for Ph-C_2H_4NO. However, in Ph-C_2H_2NO where the molecule is fully conjugated again, the Ph-NO character is once again partially restored with an almost even addition to Ph and NO – $\Delta N(\mathcal{F}_1) = +0.408\ e^-$ and $\Delta N(\mathcal{F}_{2a}) = +0.371\ e^-$. Furthermore, the N=O bond is weakened in all molecules upon addition of an electron as the intra-fragment electron density of $\mathcal{F}_{2a}$ decreases for all moieties. The largest decrease is seen in Ph-C_2H_4NO; $\Delta DI_{GS}(\mathcal{F}_1,\mathcal{F}_1) = -0.344\ e^-$.

From Table 4.7 there does not seem to be a trend in how electron density is added to the various inter-fragment delocalized electron densities. However, the addition of an electron does certainly increase overall inter-fragment delocalization, with the most significant increase in the inter-fragment delocalized density between $\mathcal{F}_1$ and $\mathcal{F}_2$ of Ph-CH_2NO; $\Delta DI_{ion}(\mathcal{F}_1, \mathcal{F}_2) = 0.996\ e^-$. Here, almost the entire electron is added to the density shared between the phenyl and its substituent.

© University of Pretoria

Table 4.6. Electron population *change* upon electron attachment for Ph-RNO molecules

	Ph-NO		Ph-CH_2NO			Ph-C_2H_4NO			Ph-C_2H_2NO		
Fragment	**Phenyl-**	**-NO**	**Phenyl-**	**-CH_2-**	**-NO**	**Phenyl-**	**-C_2H_4-**	**-NO**	**Phenyl-**	**-C_2H_2-**	**-NO**
Total $\Delta N(\mathcal{F})$	0.532	0.468	0.279	0.139	0.582	0.169	0.193	0.639	0.408	0.221	0.371
Localized $\Delta LI_{GS}(\mathcal{F})$	0.001	0.201	0.000	0.000	-0.080	0.000	0.000	0.388	0.000	0.000	0.133
Intra-delocalized $\Delta DI_{GS}(\mathcal{F},\mathcal{F})$	0.245	-0.291	-0.018	0.029	-0.284	0.074	0.084	-0.344	0.154	-0.061	-0.233
Inter-delocalized $\Delta DI_{GS}^{\mathcal{F}}(\mathcal{F},\mathcal{F}_X)$	0.287	0.558	0.297	0.110	0.946	0.096	0.110	0.595	0.253	0.282	0.471

Table 4.7. Inter-fragment delocalized density *change* upon electron attachment for Ph-RNO molecules

Molecule	**Fragments**		$\Delta DI_{ion}(\mathcal{F}_A, \mathcal{F}_B)$	$\Delta DI_{ion}(\mathcal{F}_1, \mathcal{F}_2)$
Ph-NO	Phenyl-	-NO	0.845	
Ph-CH_2NO	-CH_2-	-NO	0.357	0.996
	Phenyl-	-NO	0.938	
	Phenyl-	-CH_2-	0.057	
Ph-C_2H_4NO	-C_2H_4-	-NO	0.523	0.277
	Phenyl-	-NO	0.361	
	Phenyl-	-C_2H_4-	-0.083	
Ph-C_2H_2NO	-C_2H_2-	-NO	0.402	0.604
	Phenyl-	-NO	0.368	
	Phenyl-	-C_2H_2-	0.236	

© University of Pretoria

In summary, a novel relationship between the phenyl ring's electron count and the EA was discovered for substituted benzene molecules. However, this correlation does not seem to be ubiquitous among all kinds of substituted benzene molecules; For halogenated benzene molecules the EA declined with increasing phenyl electron population, while for the set of nitroso-substituted molecules the EA increased as the phenyl became more electron rich. Furthermore, exactly where the added electron goes within a molecule could be determined. In the halogenated molecules the electron mostly adds to the phenyl ring, but as a larger halogen is substituted it is increasingly added to this atom. For nitroso molecules the electron is spread equally between the phenyl and NO group when the molecule is fully conjugated but adds primarily to the nitroso group with non-conjugated alkyl chains separating the phenyl and the nitroso. The addition of an electron was also found to destabilize the N=O bond in all cases.

Conclusion

In this chapter it was demonstrated how the FALDI density decomposition scheme can be used to analyse two kinds of small organic electron acceptors. Like the ionization potential, the electron affinity is an important quantity governing many physical processes. Here, more links between ionization energy – specifically the electron affinity – and electronic populations within a molecule was discovered.

For the nitroso-substituted benzene molecules, electron affinity becomes increasingly negative (electron attachment becomes increasingly spontaneous) as inter-fragment delocalized density between the phenyl and substituent increases. This is a relationship analogous to that discovered for the IP of small organic acceptors in Chapter 3. This link between EA and inter-delocalized density, is not present for the halogen molecules, however.

Furthermore, a link between EA and the phenyl electron population was also discovered for both halogen- and nitroso-substituted molecules. Interestingly, these trends are opposite: less energy is required to add an electron to the halogenated molecules when the phenyl ring gains electron density. However, when nitroso- groups are substituted instead, the process of adding an electron becomes less spontaneous with increasing phenyl electron density. This is also, to our knowledge, the first time these relationships are revealed.

© University of Pretoria

Of course, the number of molecules used to establish these trends is too small to draw definite conclusions and make bold assertions. This therefore only serves the important role to indicate that the link exists.

Furthermore, in these analyses, it was again found that more electrons are shared than expected between benzene and its functionality. This again stresses the importance of long-range interactions. When halogens are substituted, this is explained by inductive effects as well as resonance. It is accepted that lone pair electrons fully participate in the π-conjugated system when only core electrons remain on an atom or fragment. The electrons can also be partially conjugated if more ED remains localized – the number of core electrons is more than what is expected. In this way the FALDI scheme allows exact calculation of the number of conjugated lone pair electrons. And with conjugation and resonance essentially being the same construct, the degree of resonance can thus be quantified.

In nitroso-substituted molecules even more ED are shared between the phenyl ring and substituted group. From the results the NO group has a tremendous electron withdrawing capacity, which, in conjunction with the fully conjugated system such as in Ph-NO, causes many electrons to be delocalized between phenyl and substituent. When saturated alkyl chains are inserted between phenyl and NO, delocalization is prevented but only to some degree. Even without a fully conjugated system, many electrons are still delocalized.

The precise effect of molecular wide conjugation could be measured by comparing systems such as Ph-C_2H_4NO and Ph-C_2H_2NO – one is partially and the other fully conjugated. The fully conjugated molecules did prove to be the most delocalized systems. Naturally, when full conjugation was restored in the Ph-C_2NO system, more Ph-NO character was also restored to the molecule such as delocalized density on the NO, delocalized density between phenyl and NO and the electron accepting mechanism. The results also suggested hyperconjugation between alkyl groups and NO as the latter's lone pair electrons are not localized even when conjugation is interrupted.

It is clear from our results that electron affinity is truly a molecular-wide property, dependent on highly correlated chemical and physical factors. It is therefore not surprising that electron affinity is not a property that is easily predictable by rational chemical concepts, unlike the electron affinity of atoms. However, FALDI provides a clear avenue to investigate the electron affinity in a chemically-interpretable manner. Since FALDI can be fully automated, we expect that it will provide tremendous insights when applied to larger datasets.

© University of Pretoria

References

[1] Hilkka Kenttämaa, *J. Chem. Soc. Perkin Trans. 2* **1999**, *0*, 2233–2240.

[2] B. T. K. and, J. Michl*, *J. Am. Chem. Soc.* **2000**, *122*, 10255–10256.

[3] K. M. B. and, S. R. Kass*, *J. Am. Chem. Soc.* **2000**, *122*, 10697–10703.

[4] K. M. B. and, S. R. Kass*, *J. Am. Chem. Soc.* **2001**, *123*, 4189–4196.

[5] T. J. Wallington, H. Egsgaard, O. J. Nielsen, J. Platz, J. Sehested, T. Stein, *Chem. Phys. Lett.* **1998**, *290*, 363–370.

[6] R. Damrauer, J. A. Hankin, *Chem. Rev* **1995**, *95*, 1137–1160.

[7] R. Cohen, N. Zenou, D. Cahen, S. Yitzchaik, *Chem. Phys. Lett.* **1997**, *279*, 270–274.

[8] * Olga V. Boltalina, Ilya N. Ioffe, and Igor D. Sorokin, L. N. Sidorov, *J. Phys. Chem. A* **1997**, *101*, 9561–9563.

[9] W. Andreoni, *http://dx.doi.org/10.1146/annurev.physchem.49.1.405* **2003**, *49*, 405–439.

[10] G. Khairallah, J. B. Peel, *Chem. Phys. Lett.* **1998**, *296*, 545–548.

[11] Seung-Yong Song, and Min Sik Jang, H.-K. Shim*, D.-H. H. and, T. Zyung, *Macromolecules* **1999**, *32*, 1482–1487.

[12] M. C. Lonergan, *Science (80-.).* **1997**, *278*, 2103–2106.

[13] R. A. Marcus, *Rev. Mod. Phys.* **1993**, *65*, 599–610.

[14] T. Liu, A. Troisi, *Adv. Mater.* **2013**, *25*, 1038–1041.

[15] P. L. A. Popelier, S. Bond, *Springer* **2016**, *170*, 71–118.

[16] I. V. Alabugin, G. dos Passos Gomes, M. A. Abdo, *Wiley Interdiscip. Rev. Comput. Mol. Sci.* **2019**, *9*, DOI 10.1002/wcms.1389.

[17] J. F. Gonthier, S. N. Steinmann, M. D. Wodrich, C. Corminboeuf, *Chem. Soc. Rev.* **2012**, *41*, 4671–4687.

[18] S. E. Wheeler, K. N. Houk, P. V. R. Schleyer, W. D. Allen, *J. Am. Chem. Soc.* **2009**, *131*, 2547–2560.

[19] M. D. Wodrich, C. S. Wannere, Y. Mo, P. D. Jarowski, K. N. Houk, P. Von Ragué Schleyer, *Chem. - A Eur. J.* **2007**, *13*, 7731–7744.

[20] F. Weinhold, C. R. Landis, E. D. Glendening, *Int. Rev. Phys. Chem.* **2016**, *35*, 399–440.

[21] L. Zhao, M. von Hopffgarten, D. M. Andrada, G. Frenking, *Wiley Interdiscip. Rev. Comput. Mol. Sci.* **2018**, *8*, DOI 10.1002/wcms.1345.

[22] Y. Mo, L. Song, Y. Lin, *J. Phys. Chem. A* **2007**, *111*, 8291–8301.

[23] P. von Ragué Schleyer, *Chem. Rev.* **2005**, *105*, 3433–3435.

[24] J. Poater, M. Duran, M. Solà, B. Silvi, **2005**, DOI 10.1021/cr030085x.

© University of Pretoria

[25] M. J. Frisch, G. W. Trucks, H. B. Schlegel, G. E. Scuseria, M. A. Robb, J. R. Cheeseman, G. Scalmani, V. Barone, G. A. Petersson, H. Nakatsuji, M. C. , X. Li, A. Marenich, J. Bloino, B. G. Janesko, R. Gomperts, B. Mennucci, H. P. Hratchian, J. V. Ortiz, A. F. Izmaylov, J. L. Sonnenberg, D. Williams-Young, F. Ding, F. Lipparini, F. Egidi, J. Goings, B. Peng, A. Petrone, T. Henderson, D. Ranasinghe, V. G. Zakrzewski, J. Gao, N. Rega, G. Zheng, W. Liang, M. Hada, M. Ehara, K. Toyota, R. Fukuda, J. Hasegawa, M. Ishida, T. Nakajima, Y. Honda, O. Kitao, H. Nakai, T. Vreven, K. Throssell, J. A. Montgomery, J. E. Peralta, F. Ogliaro, M. Bearpark, J. J. Heyd, E. Brothers, K. N. Kudin, V. N. Staroverov, T. Keith, R. Kobayashi, J. Normand, K. Raghavachari, A. Rendell, J. C. Burant, S. S. Iyengar, J. Tomasi, M. Cossi, J. M. Millam, M. Klene, C. Adamo, R. Cammi, J. W. Ochterski, R. L. Martin, K. Morokuma, O. Farkas, J. B. Foresman, D. J. Fox, **2016**.

[26] W. Koch, M. C. Holthausen, *A Chemist's Guide to Density Functional Theory*, Wiley-VCH, **2001**.

[27] T. A. Keith, **2019**.

[28] I. Cukrowski, D. M. E. van Niekerk, J. H. de Lange, *Struct. Chem.* **2017**, *28*, 1429–1444.

[29] J. H. de Lange, I. Cukrowski, *J. Comput. Chem.* **2018**, *39*, 1517–1530.

[30] J. H. de Lange, D. M. E. van Niekerk, I. Cukrowski, *J. Comput. Chem.* **2018**, *39*, 973–985.

[31] J. H. de Lange, I. Cukrowski, *J. Comput. Chem.* **2017**, *38*, 981–997.

[32] W. Humphrey, A. Dalke, K. Schulten, *J. Mol. Graph.* **1996**, *14*, 33–38.

© University of Pretoria

Chapter 5 – Tuneability of theoretically predicted charge-separation rate constants in organic solar cell interfaces

Introduction

As stated in Chapter 1, the overarching aim of this research is to apply the FALDI density decomposition technique to the modelling of electron transfer rates in organic solar cells (OSC). An OSC, primarily made up of an electron donor and acceptor material, functions by the absorption of a solar photon, causing an electron-hole pair (exciton) to form (either or both the donor or acceptor moiety can be light harvesting). Chapter 3 investigated how electron density delocalization, as measured by FALDI, influences the potential to remove an electron from an electron donor. Similarly, Chapter 4 investigated how electron delocalization affects the electron attachment potential of an electron acceptor. These two chapters therefore provided an in-depth look at two fundamental aspects and steps during electron transfer reactions. However, an effective OSC requires an interface of donor and acceptor material performing their functions as efficiently as possible. In this chapter, we investigate the donor-acceptor interface as a whole.

The various factors affecting electron transfer rates are best described by Marcus theory. Marcus theory has been described in detail in preceding chapters, and a full overview was given in Chapter 2. In this chapter, we will investigate all components of the Marcus equation for the determination of an electron transfer rate. Specifically, we aim to further explore the role of electron delocalization within the various terms in the Marcus equation.

As mentioned in the preceding chapters, electron delocalization is particularly difficult to measure. Numerous reports have indicated, however, that the FALDI density decomposition technique is perfectly suited to study electron (de)localization in real chemical molecules using a real-space approach. Since the FALDI density decomposition technique has never before been applied to study electron transfer reactions, we expect that FALDI will be a very useful tool for decomposing the Marcus equation and investigating each component with extreme detail.

© University of Pretoria

Theoretical Background

In Chapter 2, the theoretical background, the theory on which this chapter builds were covered extensively. Here we wish to briefly reiterate the core aspects thereof. Marcus theory,[10] the theory that revolves around the calculation of the rate of charge transfer between two moieties, is expressed by the equation;

$$k = \sqrt{\frac{4\pi^3}{h^2 \lambda k_B T}} |V_{DA}|^2 e^{-\frac{(\Delta G^0 + \lambda)^2}{4\lambda k_B T}} \quad (5.1)$$

Here k is the rate of electron transfer from the donor to the acceptor (charge separation, k_{CS}) or from the already charged acceptor to the already discharged donor (charge recombination, k_{CR}). h is Planck's constant, λ is the recombination energy which can neither be negative nor zero (energy required to rearrange the atoms in the molecules from the initial to final geometry when the electronic state of the molecule is kept constant), k_B is Boltzmann's constant, T is the temperature in Kelvin, V_{DA} is the electronic coupling between donor $\mathcal{D}$ and acceptor $\mathcal{A}$ of the initial and final state and ΔG^0 is the change in Gibbs free energy of the process. The species dependent parameters are the change in the Gibbs free energy, the reorganization energy, and the coupling potential, and are therefore of great importance in this work.

A remarkable result of the Marcus equation is the so called 'inverted region'. Generally, when considering reactions' ΔG^0 value, we can tell its spontaneity and thereby gives an indication of the rate of the process – a very negative ΔG^0 suggests a quick rate and a less negative ΔG^0 a slow rate.[16] However, electron transfer reactions described by Marcus theory behaves differently. When examining the exponential term of eqn. 5.1, it becomes clear that a very negative ΔG^0 would not always be in favour of a faster rate. In fact, $-\Delta G^0$ should equal λ or at least be close to it for optimal transfer rates. If not, the rate suffers as a result. This is illustrated in Figure 5.1 which gives the rate constant as a function of ΔG^0 and λ. For some reorganization energy λ there exists an optimal value of ΔG^0 that will result in the maximum rate constant as determined by the pre-exponential factor.

© University of Pretoria

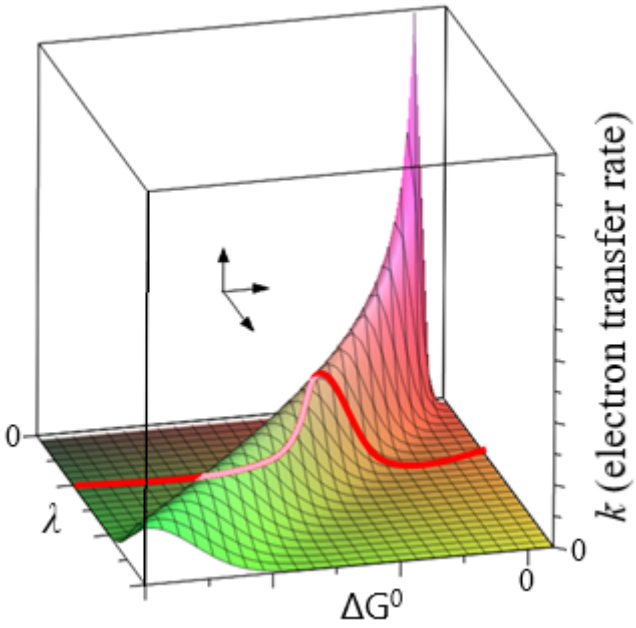

Figure 5.1. The rate constant as a function of both the reorganization energy as well as the change in Gibbs free energy, at a constant temperature of T=298 K.

ΔG^0 can be calculated as follows;[7]

$$\Delta G^0 = IP_D + EA_A + \Delta E_{col} \tag{5.2}$$

Where IP_D is the ionization potential of the donor, EA_A is the electron affinity of the acceptor (calculated same way as the IP) and ΔE_{col} is the change in total coulombic potential energy. It can be assumed that the donor is excited by a photon and thereby IP_D is the ionization potential of a ground state or excited state donor for calculation of the rate in the absence or presence of a light source, respectively.

Only the internal reorganization energy, λ_i, was used and thereby the subscript i will be dropped. This is calculated as the average of $\lambda_{[D*A]}$ and $\lambda_{[D+A-]}$,

$$\lambda = \frac{\lambda_{[D*A]} + \lambda_{[D+A-]}}{2} \tag{5.3}$$

where $\lambda_{[D*A]}$ is the difference in energy of the reactants (prior to charge transfer) at the product (charge transfer state) geometry and the reactants at their optimum geometry. The subscript [D*A] indicates the case of excited donor, however for calculation in the absence of light $\lambda_{[DA]}$ is used.[17] This is expressed as

$$\lambda_{[D*A]} = \left(E_{D*(+)} + E_{A^{(-)}}\right) - (E_{D*} + E_A) \tag{5.4}$$

© University of Pretoria

and is analogous for $\lambda_{[D+A-]}$. Figure 5.2 showing the energy-geometry curves of the different states explains this more elegantly. $E_{D*(+)}$ is the energy of the excited donor at the cationic optimized geometry. The average of $\lambda_{[D*A]}$ and $\lambda_{[D+A-]}$ is necessary since the potential energy curvatures (Figure 5.2) of the of the reactant ([$\mathcal{D}^*$-$\mathcal{A}$]) and product ([$\mathcal{D}^+$-$\mathcal{A}^-$]) often differ.

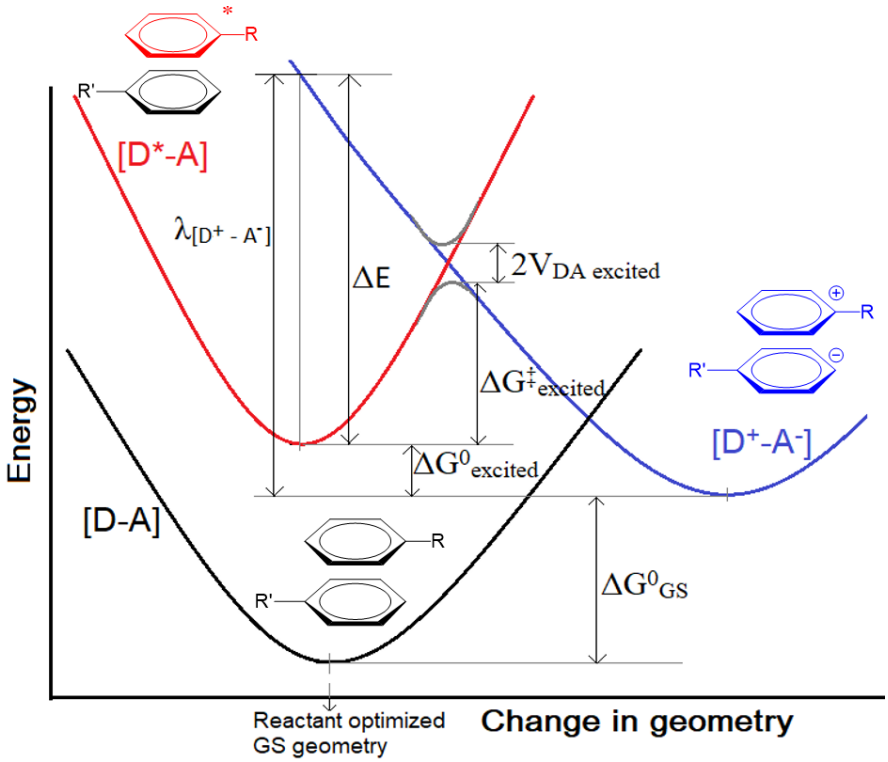

Figure 5.2. Potential energy wells for neutral and non-excited state ([$\mathcal{D}$-$\mathcal{A}$], black), neutral donor excited state ([$\mathcal{D}$*-$\mathcal{A}$], red) and the cationic donor anionic acceptor charge separated state ([$\mathcal{D}^+$-$\mathcal{A}^-$], blue). Parameters used in the Marcus equation are visually illustrated here.

The coupling potential, V_{DA}, gives the energy due to the electronic coupling of the donor and acceptor interface between the initial and final state (see Figure 5.2). V_{DA} is calculated as the relatedness of the initial and final state and can therefore be expressed as

$$V_{DA} = \int \Psi^*_{[D*A]} \Psi_{[D+A-]} d\tau. \tag{5.5}$$

Generally, solving for V_{DA} this way is challenging, therefore the generalized Mulliken-Hush (GMH) approximation[18],[19] is employed;

$$V_{DA} = \frac{\mu_{tr} \Delta E}{\sqrt{\Delta\mu^2 + 4{\mu_{tr}}^2}} \tag{5.6}$$

© University of Pretoria

where μ_{tr} is the transition dipole-moment from initial to final state, $\Delta\mu$ is the change in stationary dipole moment and ΔE is the difference in the electronic energy between the initial and final state (also known as the vertical excitation energy). The transition dipole moment is defined as

$$\vec{\mu}_{tr} = \int \Psi_f^* \hat{\boldsymbol{\mu}} \Psi_i d\tau \tag{5.7}$$

with Ψ_i and Ψ_f representing the initial and final state, respectively, and $\hat{\boldsymbol{\mu}}$ is the electric dipole moment operator. We note here that there are a large number of approaches for approximating V_{DA}, some of which we will explore and compare in the future.

Computational Methods

All calculations were performed using the Gaussian 09 package[20] with density functional theory (DFT) method,[21] CAM-B3LYP level of theory and augmented cc-pVDZ basis set. Atomic overlap matrices and QTAIM analyses were calculated using the AIMAll version 17.11.14.[22] FALDI data was calculated using in-house software[12–15] with the LO algorithm. FALDI isosurfaces were visualized using VMD version 1.9.3.[23] Transition dipole moments and additional visualizations regarding excited states were determined through Multiwfn v3.6.[25]

Strategy for calculating electron transfer rate constants

Here follows the practical methodology implemented for the calculation of the charge separation rate constants – k_{CS} (no photoexcitation) and k_{CS}* (electron donor underwent photoexcitation), as well as the charge recombination rate constant; k_{CR}. As detailed in in the Theoretical Background, the Gibbs free energy (ΔG^0), the reorganization energy (λ) and the coupling potential (V_{DA}) need to be calculated from which the rate constants can be obtained with the Marcus eqaution.[24]

To find ΔG^0, the IP, EA and ΔE_{col} is required. For calculation of all energetic terms – IP, EA, reorganization energy (λ) and the vertical excitation energy (ΔE) – optimizations and single point calculations (SPCs) were performed on the appropriate geometries and electronic states. I.e., for the calculation of the IP of the ES of some moiety, we need the energy of the optimized ES and that of the cationic state at ES geometry. The IP calculated here is therefore

© University of Pretoria

also the vertical IP as used in Chapter 3 – the energy required to remove an electron without geometric rearrangement. Similarly, this was done for the EA as well – corresponding to Chapter 4. The reorganization energy is that used to physically rearrange the interface system from the optimized initial state geometry to the optimized final state geometry while the electronic state remains the same. The vertical excitation energy is that required to change electronic state of the interface system while nuclear coordinates remain fixed. To reiterate; all terms' calculation is expressed mathematically and is visually illustrated in Chapter 2.

The change in electrostatic potential, ΔE_{col}, due to charge transfer was approximated in the following manner: effective atomic charges before and after charge transfer were obtained by the Quantum Theory of Atoms in Molecules (QTAIM) analyses on the individual optimized initial and final structures. For instance, for the calculation of k_{CS}*, the atomic charge differences between the cationic and excited states were calculated. These atomic charges were then used with their initial and final atomic coordinates in an interface system (Figure 5.6). The electrostatic potential between donor and acceptor was then calculated for the initial state of the interface as well as the final state (the initial and final interfaces have slightly different geometries as different optimized structures were used to build it). The difference between these quantities gives ΔE_{col}. IP, EA and ΔE_{col} were then used to calculate the change in Gibbs free energy (ΔG^0).

To recall, the coupling potential, V_{DA}, is obtained by the generalized Mulliken-Hush approximation[18],[19] which relies on three quantities – the change in static dipole moment ($\Delta\mu$), the transition moment (μ_{tr}) and the vertical excitation energy (calculation of the latter already described).

The first two terms were determined as follows: Donor-acceptor interfaces were built from the donor's ground-state and excited-state optimized geometries and acceptor's ground-state geometries (optimized cationic donor and anionic acceptor geometries were used for recombination rate calculations). For these interfaces the first 20 excited states were calculated by TD-DFT as a SPC. These states' degree of charge transfers were then classified in order to find the states that best represent the appropriate initial and final state. As an example, for the determination of k_{CS}*, the two interface states where only the donor is excited (initial) and where CT occurred (final) was searched for. Good excited state candidates' MO isosurfaces should match that of the individual moieties as in Figure 5.3 and 5.4. Transitions involving MOs of the π-system were selected as these were consistently found throughout the four

© University of Pretoria

interfaces, their spatial occupation suggests good coupling, and these are often prominently involved in the transitions with good oscillator strength. As an illustration, for the excitation of Ph-NH_2, the transition MO25 → MO29 is the most prominent in the likely to occur ES1. And for that of the interface ([NH_2-NO]), the transitions MO53 → MO56 and MO53 → MO60 is the most prominent in interface-ES3, which matches that of the individual moiety (Figure 5.4). Also note how these MO isosurfaces match that in Figure 5.3. More details of all interfaces used (Figure 5.6) are included in the SI, where the excitation energies for individual and interface systems are also provided.

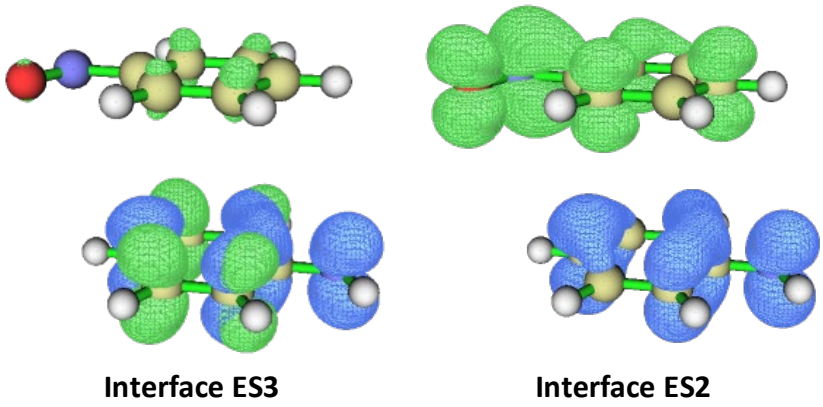

Figure 5.3. Interface [NH_2-NO] donor excited state (ES3) and CT state (ES2) (iso = 0.002). Green = ED increase, blue = ED depletion.

© University of Pretoria

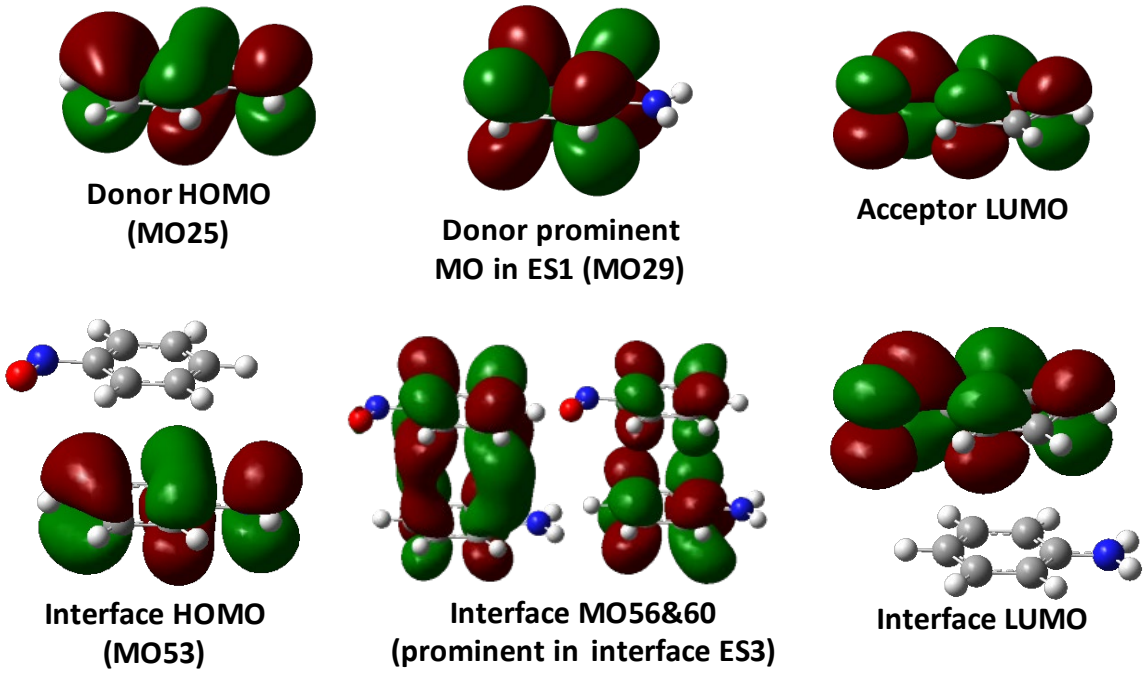

Figure 5.4. Ph-NH_2 and Ph-NO individual and interface MOs corresponding to ESs in Figure 5.3 (iso = 0.020).

For the [NH_2-NO] interface, ES3 and ES2 was then accepted as appropriate to represent the initial and final state of the system, respectively. The same procedure was followed for the rest of the interfaces. The appropriate interface-ESs were then noted to repeat the TD-DFT SPCs, aimed specifically at saving the data of these states. This allows the static dipole moment, μ, to be obtained for these states from which the difference between initial and final, $\Delta\mu$, can be taken as described in Chapter 2. The transition dipole moment, μ_{tr}, was obtained using Multiwfn.[25]

With these dipole moments, $\Delta\mu$ and μ_{tr}, and the vertical excitation energy obtained, the coupling potential could be calculated by eqn. 5.6. With this being the last of the parameters that were required, the rate constants can then be calculated with the Marcus equation.[24] The methodology described above is strongly based upon that followed numerous similar applications in literature.[7,26–28]

To attempt to fundamentally understand the results that was obtained from the above-described calculations, FALDI analyses were also performed on the interfaces. Naturally, the donor and acceptor were selected as each being a 'fragment' giving the most simplistic and intuitive results – Figure 5.5. A 4-fragment scheme, where each functional group and phenyl

© University of Pretoria

is its own fragment (as in Chapters 3 and 4) is excluded from this project in favour of simplification but will be explored in future work.

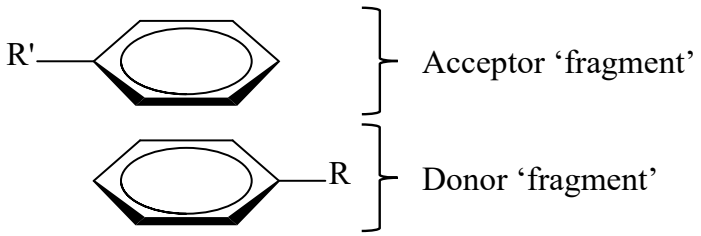

Figure 5.5. FALDI fragmentation scheme used

Results and Discussion

Rate constants were calculated for four interface combinations – Figure 5.6. These are combinations of Ph-NH_2 and Ph-NPr_2 (donors) and Ph-NO and Ph-C_2H_4NO (acceptors). The interplanar distance was set to 4Å with the functional groups facing opposite directions to minimize interference with the electronic coupling. Hereby the electronic coupling should solely consist of the interaction of the electron clouds on the phenyls of both moieties. This way the molecular wide effect of the functional groups is considered rather than their localized influence. As described in detail in Chapter 2, the interfaces were mathematically constructed ensuring consistency by minimal geometry dependance in the results. The calculated rate constants for these four interfaces are presented in Table 5.1.

© University of Pretoria

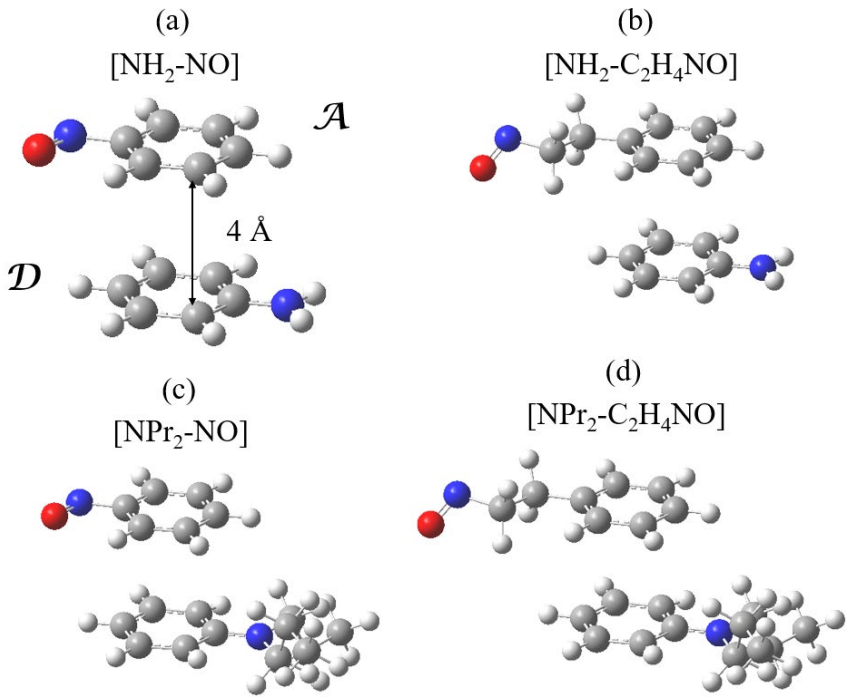

Figure 5.6. Interface geometries. Optimized excited state geometries were used for donors and optimized ground state geometries for acceptors.

Table 5.1. Charge separation (k_{CS}, k_{CS}*) and recombination (k_{CR}) rate constants

Interface	k_{CS} [$\mathcal{D}$-$\mathcal{A}$] (e^-/s)	k_{CS}* [$\mathcal{D}$ *-$\mathcal{A}$] (e^-/s)	k_{CR} [$\mathcal{D}^+$-$\mathcal{A}^-$] (e^-/s)
(a)	1.84×10^6	4.27×10^{11}	9.38×10^6
(b)	3.72×10^4	8.40×10^{13}	2.74×10^8
(c)	1.04×10^7	1.92×10^{11}	1.15×10^8
(d)	1.60×10^7	7.18×10^{10}	2.81×10^9

The optimized donor and acceptor geometries used in the interface is indicated in square brackets. I.e., for [$\mathcal{D}$*-$\mathcal{A}$], donor ES-opt and acceptor GS-opt structures were used. Note how k_{CS}* is, on average, several orders of magnitude greater than k_{CS} and k_{CR}, while k_{CS} is inferior to k_{CR}. A net forward charge transfer in the presence of an appropriate light source is therefore predicted, as the forward rection is abundantly quicker than the reverse. And no current is expected when a light source is absent as the recombination rate dominates separation in the absence of an excitation. The scale of these rates and their proportions relative to each other resembles experiment and literature.[7]

It is important to remember that the rates in Table 5.1 should only be considered seriously in a qualitative way thus far. It might be the case that they carry quantitative merit, but the

© University of Pretoria

methodology followed, although based on literature,[7,26–28] was not actively validated. There is a good indication, however, that the rates are realistic as it compares very well with that in literature,[7],[29] but it must be admitted that these are different systems. Here it is assumed that they are quantitatively valid relative to each other.

As described earlier in Chapter 2, the Marcus equation[24] is essentially an Arrhenius equation that describes the rate of electron transfer instead of a chemical reaction. The Arrhenius equation gives the rate of a chemical reaction based on the energetic favourability, and similarly does the coupling independent part of the Marcus equation. Therefore, the rate equation can be decomposed by making a distinction between this energetic driving force and the electronic coupling.

In Table 5.2, k_{CS}* is decomposed into the coupling potential V_{DA} and the energetic driving force. With solar cells dependent on a light source, the charge transfer rate due to a photoexcitation (k_{CS}*) is what we are most interested in. The driving force is relatively similar in all cases, but this is not the case for V_{DA}. The electronic coupling of interface **(b)** massively outperforms that of the other interfaces, resulting in its rate constant to be at least two orders of magnitude higher. Therefore, a CT may be energetically very favourable, however, if there is poor coupling of the initial and final state, the rate constant will be greatly limited. It is for this reason that more attention will be given to deciphering the origins of V_{DA}.

Table 5.2. Decomposed [$\mathcal{D}$ *-$\mathcal{A}$] charge transfer rate constants

Interface	V_{DA}^{α} **(au)**	**Driving Force**	k_{CS}* **(e^-/s)**
(a)	0.0020	1.06×10^{17}	4.27×10^{11}
(b)	0.0317	8.37×10^{16}	8.40×10^{13}
(c)	-0.0015	8.35×10^{16}	1.92×10^{11}
(d)	0.0009	9.78×10^{16}	7.18×10^{10}

α – V_{DA} will be squared thus negatives may be omitted
Driving force is the exponential term in the Marcus equation.

To investigate the coupling potential, it is analysed in conjunction with the FALDI results. With the FALDI decomposition scheme, the electron densities were again decomposed into localized (LI($\mathcal{A}$)), intra-fragment delocalized (DI($\mathcal{A}$,$\mathcal{A}$)) and inter-fragment delocalized (DI($\mathcal{A}$,$\mathcal{B}$)) ED. The donor and acceptor are each a fragment – a 2-fragment scheme is therefore used. In Table 5.3, the change in these EDs due to electron transfer is given for the donor and acceptor. For **(a)** and **(b)** these results are visualized in Figure 5.5. Only these two interfaces

© University of Pretoria

are included since that of **(a)** and **(c)** are almost identical and **(b)** and **(d)** are similar (see SI – Figures S5.2 – S5.5). Figure 5.7 is to be observed alongside Table 5.3 as it is a qualitative and visual representation of the same results.

For **(a) – (c)** there is a reasonable charge transfer of 0.6 – 0.8 e^- (1 e^- is ideal) and is considered valid. However, **(d)** does not permit an actual charge transfer as only about 0.09 e^- is transferred in the transition (Table 5.3). For this reason, we disregard **(d)** as its severely incomplete CT is not considered usable to draw conclusions from. In Table 5.4 the rate constants are scaled by this fraction of electrons transferred in the transition. Obviously, this has the biggest impact on the rate of **(d)**, while **(a)** – **(c)** remains relatively similar.

Table 5.3. [$\mathcal{D}$*-$\mathcal{A}$] ED change upon charge transfer – FALDI results

		Electron density distribution category					
Interface		**Total ED change**	**ΔLI($\mathcal{D}$) & ΔLI($\mathcal{A}$)**	**ΔDI($\mathcal{D}$,$\mathcal{D}$) & ΔDI($\mathcal{A}$,$\mathcal{A}$)**	**ΔDI^D($\mathcal{D}$,$\mathcal{A}$) & ΔDI^A($\mathcal{D}$,$\mathcal{A}$)**	**ΔDI($\mathcal{D}$,$\mathcal{A}$)**	**V_{DA} (au)**
(a)	**NH_2***	-0.853	-0.086	-0.258	**-0.471**	**-0.710**	0.0020
	NO	0.852	0.026	1.134	**-0.239**		
(b)	**NH_2***	-0.611	-0.117	-0.452	**-0.027**	**0.204**	0.0317
	C_2H_4NO	0.609	-0.059	0.456	**0.231**		
(c)	**NPr_2***	-0.846	0.000	-0.347	**-0.461**	**-0.658**	-0.0015
	NO	0.846	0.007	1.103	**-0.197**		
(d)	**NPr_2***	-0.090	0.009	0.017	**-0.101**	**-0.089**	0.0009
	C_2H_4NO	0.086	0.051	0.019	**0.012**		

Table 5.4. Scaling the rate constants with actual number of electrons transferred

Interface	**k_{CS}* (e^-/s)**	**Scaled k_{CS}* (e^-/s)**
(a)	4.27×10^{11}	3.64×10^{11}
(b)	8.40×10^{13}	5.13×10^{13}
(c)	1.92×10^{11}	1.62×10^{11}
(d)	7.18×10^{10}	6.32×10^{9}

From Table 5.3, the CT mechanism for interfaces **(a)** and **(c)** appears to be almost identical, indicating that the propyl group does not significantly affect V_{DA} (see also SI). We therefore continue by comparing **(a)** and **(b)**, which show substantial differences, to find the cause of the V_{DA} results.

© University of Pretoria

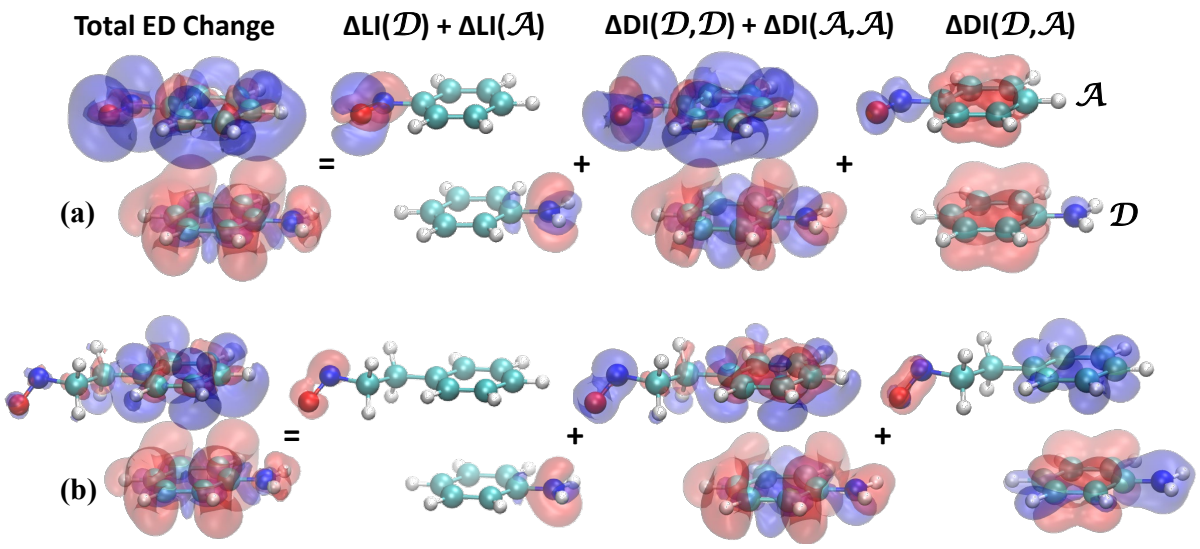

Figure 5.7. Change of ED due to charge transfer (iso = 0.001). Blue = ED increase, red = ED depletion. (A justification for combining ΔLI($\mathcal{D}$) & ΔLI($\mathcal{A}$) and ΔDI($\mathcal{D}$,$\mathcal{D}$) & ΔDI($\mathcal{A}$,$\mathcal{A}$) in the same isosurfaces is provided in the SI – see Figure S5.1)

From Table 5.3, there is a significant difference between **(a)** and **(b)** in how DI($\mathcal{D}$,$\mathcal{A}$) changes upon charge transfer. In **(a)**, most of the ED transferred from the donor is removed from DI^{D}($\mathcal{D}$,$\mathcal{A}$) (-0.471 e^-), however, DI($\mathcal{D}$,$\mathcal{D}$) also contributes to the transfer (-0.258 e^-) as well as a small amount of the donor's core electrons (-0.086 e^-). Most of the transferred ED is added to the *deloc*-ED of the acceptor, DI(A,A) (+1.134 e^-). A portion of DI^{A}($\mathcal{D}$,$\mathcal{A}$) is also removed and also added to DI($\mathcal{A}$) (-0.239 e^-), which inflates the change in DI($\mathcal{A}$,$\mathcal{A}$) to more than what is actually transferred to the acceptor. The ED shared between the donor and the acceptor, is therefore decreased on both moieties causing the total, DI($\mathcal{D}$,$\mathcal{A}$), to decrease with 0.710 e^-. In simple terms, the charge transfer mechanism in the [NH_2*-NO] interface mostly involves the transfer of electron density shared between $\mathcal{D}$ and $\mathcal{A}$ towards the acceptor, as well as a small amount of density delocalized on $\mathcal{D}$. This resulted in a coupling potential of 0.0020 au.

In contrast to **(a)**, in **(b)**, most ED is removed from DI($\mathcal{D}$,$\mathcal{D}$) (-0.452 e^-) and a relatively high amount from the localized electrons as well (-0.117 e^-) – the core electrons normally remain little affected in these transitions, thus this is probably the displacement of lone pair electrons. The removed density is also added primarily to DI($\mathcal{A}$,$\mathcal{A}$) (+0.456 e^-) but a fair amount is also added to DI^{A}($\mathcal{D}$,$\mathcal{A}$) (+0.231 e^-). With little change of DI^{D}($\mathcal{D}$,$\mathcal{A}$), DI($\mathcal{D}$,$\mathcal{A}$) increased with 0.204 e^-. In other words, the charge transfer mechanism for [NH_2*-C_2H_4NO] is

© University of Pretoria

that the density transferred to the acceptor was originally found only (de)localized on the donor. Most of this is transferred to that delocalized within $\mathcal{A}$ with a small amount added to that on $\mathcal{A}$ but also shared with $\mathcal{D}$. This resulted in a coupling potential of 0.0317 au.

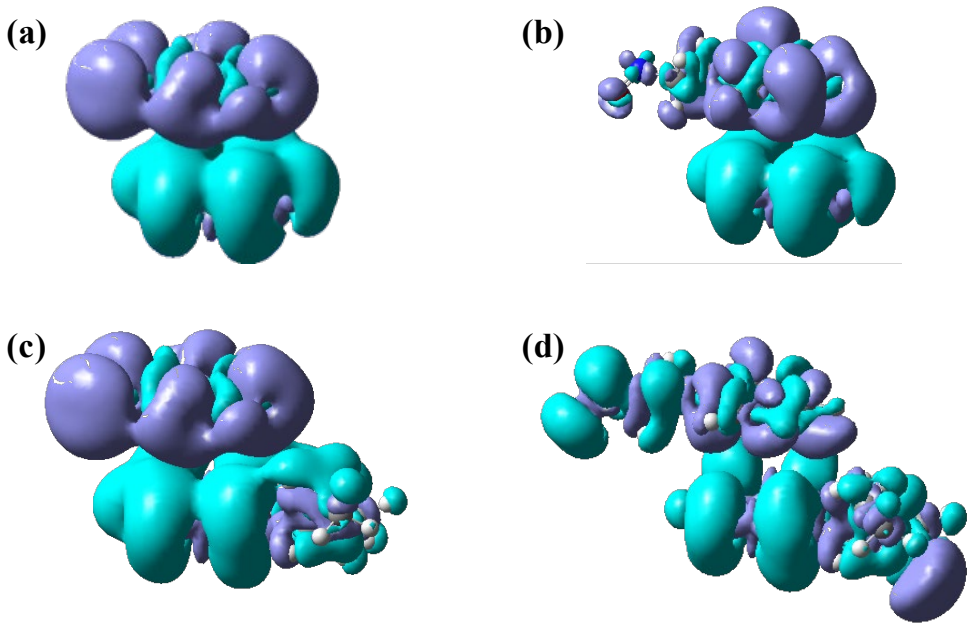

Figure 5.8. ED change upon charge transfer for [$\mathcal{D}$ *-$\mathcal{A}$] interfaces (iso = 0.004). Purple (top) = ED increase, cyan (bottom) = ED depletion.

The GausView[30] computed charge transfer isosurfaces are shown in Figure 5.8. These are in good agreement with the Total ED change isosurfaces computed with the FALDI results shown in Figure 5.7. Form visual inspection of these isosurfaces there is no indication why **(b)** has an excellent coupling potential but not the other interfaces. However, one can note that higher alkyl content in the substituent seems to cause a disruption in the clarity of the charge transfer, with the worst instance being interface **(d)**. This appears to be a cause for the poor Total ED transferred in this interface.

These results indicate that the intricacies of how the electronic structure change is linked to the coupling potential. The coupling potential is probably not linked to the total ED transferred – Table 5.3, and the energetic driving force is likely not linked to either the total ED transferred or the change in electronic structure. The latter is deduced from the fact that the energetic driving force for interfaces **(b)** and **(c)** are very similar (Table 5.2), but their FALDI results are vastly different (Table 5.3). This agrees with the results from Chapter 3 and 4, where it is stated

© University of Pretoria

that there does not seem to be a trend or rationale for the way the internal electronic structure changes upon ionization. To predict the driving force, one should therefore rather turn to analysing the intra-molecular delocalization (and perhaps the inter-molecular delocalization) of the molecules in an interface system.

From results in Table 5.3 it is tempting to draw the conclusion that if DI($\mathcal{D}$,$\mathcal{A}$) increases after charge transfer, there will be good coupling between donor and acceptor and vice versa. However, this would be erroneous. As mentioned earlier, the sign of the coupling potential is not of importance (as it is squared when used in the Marcus equation[24]) but the absolute value of it is. Therefore, since the calculation of V_{DA} solely consists of differences in energies and differences in dipole moments, the sign of V_{DA} is reversed when the final and initial states are reversed. Stated differently; the exact same coupling potential (absolute value) is obtained when considering the reverse reaction. This means if we take all initial as final and final as initial states, the sign of all quantities in Table 5.3 will be reversed. Thus, it is incorrect to state that an increase of DI($\mathcal{D}$,$\mathcal{A}$) will give a good coupling since the reverse reaction, giving the same $|V_{DA}|$, will show a decrease in DI($\mathcal{D}$,$\mathcal{A}$).

It would therefore be more realistic to consider possibilities such as a correlation between the magnitude of ΔDI($\mathcal{D}$,$\mathcal{A}$) and $|V_{DA}|$, or the difference between ΔDI$^{\mathrm{D}}$($\mathcal{D}$,$\mathcal{A}$) and ΔDI$^{\mathrm{A}}$($\mathcal{D}$,$\mathcal{A}$) and $|V_{DA}|$ – or perhaps both. A link between system-wide electron delocalization and electronic coupling between states is conceivable; however, a larger data set will be required to accurately investigate this link.

In Table 5.5, V_{DA} is further separated into its three components. From this, the deciding factor that results in interface **(b)** having the best coupling (and therefore the highest rate constant), is its transition dipole moment being significantly higher (1.612 au vs 0.164 au). The change in static dipole moment is also noticeably different (4.144 au vs 6.139 au). The coupling potential of **(b)** is not only enhanced due to its transition moment, but is also energetically strengthened compared to its contemporaries, although not to a great extent.

Important to note is that for none of these parameters the sign matters – not even relative to each other. A sign change in ΔE or μ_{tr} will only result in the coupling potential being of opposite sign (eqn. 5.6). Only the absolute value of the quantities in Table 5.5 is therefore of

© University of Pretoria

importance. The greater the absolute value, for any of the three parameters, the greater the coupling potential.

Table 5.5. Decomposition of coupling potential

Variable (all in au)	Interface (ES donor) **(a)**	**(b)**	**(c)**
ΔE	0.075	0.103	0.056
μ_{tr}	0.164	1.612	-0.167
$\Delta\mu$	6.139	4.144	6.154
V_{DA}	0.0020	0.0317	-0.0015

The transition dipole moment between initial state Ψ_i and final state Ψ_f, Eqn. 5.7., is a vector quantity of which the magnitude (which is used in the Marcus equation[24]) can be regarded as a measure of charge redistribution due to an electronic transition. More specifically, a transition is active only if the charge redistribution has a dipole associated with it.[31] Clearly, a change in electronic structure is linked to the coupling potential – a fact that has major implications for the interpretation of our results.

Firstly, it implies that all information about μ_{tr} are contained in how the electron density is redistributed in an electronic transition. If this is true then μ_{tr} can – in principle – be recovered from Table 5.3 and Figure 5.7 given that these are a complete description and decomposition of the electron density redistribution. In that case, the FALDI decomposition scheme is a promising tool for offering an alternative way of calculating (or at least approximate) the transition dipole moment of an electronic transition.

Secondly, the slower rates for interfaces **(a)** and **(c)** are thus due to a lesser charge redistribution or a redistribution without a strong dipole associated with it. From Table 5.3, **(a)** and **(c)** shows a stronger redistribution (~0.8 e^-) than **(b)** (~0.6 e^-). The charge redistribution of **(b)** must therefore have a stronger dipole associated with it, overshadowing its lesser degree of charge redistribution. From this it naturally flows that if more ED is transferred in a transition, the transition moment should be stronger for the same spatial redistribution of the charge. This again stresses the fact that no definite information about the coupling potential (the transition moment really) can be obtained by only considering the amount of charge transferred in a transition or the isosurface of ED change as in Figure 5.8.

© University of Pretoria

The change in static dipole moment is, however, likely connected to the total electron density transferred in the transition. In interfaces **(a)** and **(c)**, ~0.8 e^- are transferred from donor to acceptor with a change of static dipole moment of ~6.1 au. While interface **(b)** displays a charge transfer of ~0.6 e^- with a change in static dipole moment of ~4.1 au associated with it. The differences seem to be somewhat in proportion to each other and suggests a link between total charge transferred from donor to acceptor and the change in static dipole moment. But more than this cannot be said as this relies only on three data points.

Decomposition of the Driving force

In Table 5.6 the thermodynamic driving force of the electron transfer, as given in Table 5.2, is decomposed into the change in Gibbs free energy, ΔG^0, and the internal reorganization energy, λ. The two components from which λ_i is the average is also given – $\lambda_{[D*A]}$ and $\lambda_{[D+A-]}$. Notice how these two components are not significantly different. This indicates that the potential energy curves (Figure 5.2) of the initial and final states of the interfaces have similar curvature which adds to the reliability of the average used.

Table 5.6. Decomposition of Driving Force

Interface	**Driving Force**	ΔG^0 **(eV)**	$\lambda_{[D*A]}$ (eV)	$\lambda_{[D+A-]}$ (eV)	λ_i **(eV)**	$(\Delta G^0 + \lambda_i)^2$ **(eV)**
(a)	1.06×10^{17}	-0.932	0.453	0.296	0.375	0.311
(b)	8.37×10^{16}	0.193	0.633	0.442	0.537	0.534
(c)	8.35×10^{16}	-1.204	0.466	0.441	0.454	0.562
(d)	9.78×10^{16}	-0.143	0.645	0.588	0.616	0.224

Driving force is the exponential term in the Marcus equation.

Interestingly, despite substantial differences between ΔG^0 values, the differences in the driving force are relatively small. This is possibly due to a balance between $1 / \lambda$ in the exponential term and the pre-exponential factor in eqn. 5.1. Furthermore, Table 5.6 presents a clear demonstration of the effect of the Marcus inverted region. Comparing interfaces **(a)** and **(c)**; interface **(c)** has a ΔG^0 that suggests a more spontaneous charge transfer than **(a)**, however, due to the mismatch in energy with the reorganization energy, interface **(a)**'s driving force is superior. This is graphically illustrated by Figure 5.1.

Table 5.7 gives a quantitative example of the effect of the inverted region for interface **(a)** where the reorganization energy (as well as all other variables) was held constant while changing ΔG^0 to produce three different scenarios. Clearly, as ΔG^0 gets more and more negative – which would generally suggest a more and more spontaneous process – the rate of

© University of Pretoria

charge transfer falls flat. This emphasizes the importance of having $\Delta G^0 + \lambda$ close to zero and therefore the importance of having fine control over the IP and EA since they are used to calculate ΔG^0. Moving past scenario 1 with decreasing ΔG^0 – having $|\Delta G^0 + \lambda|$ about 1.5 eV or greater, the rate constant starts to severely suffer as a result.

Table 5.7. Analysis of the inverted region of interface **(a)**

	k_{CS} (e^-/s)	ΔG^0 (eV)	λ_i (eV)	$\Delta G^0 + \lambda_i$ (eV)
Actual	4.27×10^{11}	-0.932	0.375	-0.558
1	1.72×10^{11}	-1.5	0.375	-1.125
2	8.30×10^{8}	-3.0	0.375	-2.625
3	5.60×10^{4}	-4.5	0.375	-4.125

Rate constant vs IP and EA

In Figure 5.9 it is illustrated how the rate of electron transfer varies with changes in the ionization potential of the donor and the electron attachment energy of the acceptor. Since the IP of the donor and EA of the acceptor, which are directly used in the calculation of ΔG^0, are interlinked with λ and ΔE, one cannot simply change the IP_D and EA_A to plot the rate's dependency on them. There is more than one way by which ΔG^0 can be altered and therefore there is no single way by which the rate would respond to these different kinds of changes.

In Figure 5.9 IP_D and EA_A is changed by means of varying the optimized excited donor and optimized neutral acceptor energy levels – these affects ΔG^0 and ΔE but not λ (see Figure 5.2). (Since the varying of IP_D and EA_A is only hypothetical, there is no need to take the average of the reorganization energy – therefore, only $\lambda_{[D+A-]}$ was used for λ.) This way of varying the difference in energy between initial and final state can be understood as the reactants' potential energy curve – red (or black) curve in Figure 5.2 – being moved up or down whilst the rate is calculated at every infinitesimal change for both changes in IP_D and EA_A. Thereby IP_D and EA_A was varied without changing the energy level of the products and without altering the curvature of the reactants' or the products' potential energy wells.

© University of Pretoria

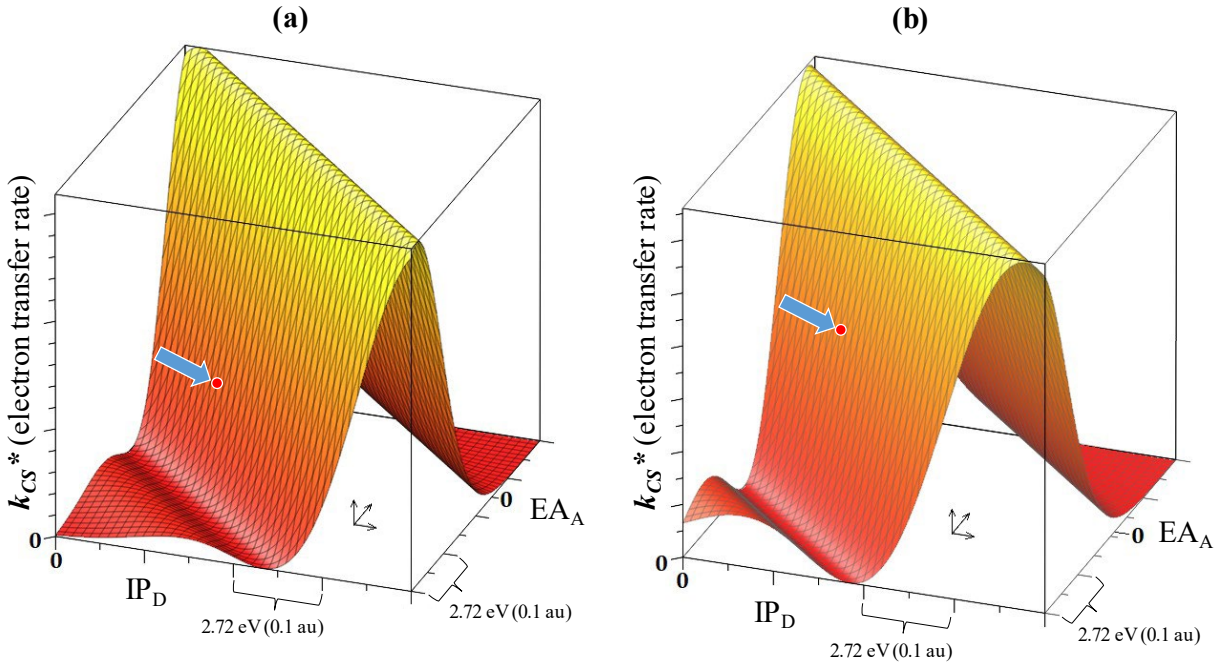

Figure 5.9. Rate constant of interfaces **(a)** and **(b)** as a function of IP_D and EA_A. Arrows indicate actual rates for the actual IP_D and EA_A; 4.27×10^{11} e^-/s and 8.40×10^{13} e^-/s for interfaces **(a)** and **(b)**, respectively.

The behaviour of the rate with changes in IP_D and EA_A for interfaces **(a)** and **(b)** are markedly similar with differences essentially only being in the amplitude. Note that the scales for the rate in **(a)** and **(b)** are not the same. The rate for interface **(b)** is about 200 times greater than that of **(a)**, which is therefore completely dwarfed in comparison.

These surfaces give another 'perspective' on the Marcus inverted region which is where IP_D and EA_A are lowest. These figures therefore closely resemble Figure 5.1 but with a constant λ, a dependency on both IP_D and EA_A instead of only ΔG^0 and with the simultaneous change of ΔE is now also accounted for.

Figure 5.9 show that in both interfaces, the actual calculated rate is on an exceptionally 'steep' slope, meaning that small changes in either IP_D or EA_A will result in significant changes in the rate. Also, the rates achieved are only about half of what it could potentially be for the given reorganization energy. This beautifully illustrates and emphasizes the significance of tuning IP_D or EA_A and provides a direct link to Chapters 3 and 4 where possibilities of finetuning IP of EA are investigated. For instance, Figure 5.9a suggests that an increase in IP_D would result in an increased rate constant. This knowledge we can combine with that learned in Chapter 3; we can tune the donor to have an increased or decreased IP by tuning the degree of delocalization between phenyl and substituent. This in turn can be done by changing the

© University of Pretoria

alkyl length of the R-group in Ph-NR_2. However, this is only predictable when assuming there is no change in the coupling potential when administering such changes.

ED comparison of individual and interface moieties

A quick review of the agreement of Chapter 3 & 4 and Chapter 5 data; The localized ED on the donor and acceptor in the interfaces is found to agree with that of the individual molecules to a reasonable degree. I.e. the total localized electron density for the individual molecules Ph-NH_2 and Ph-NO are 15.14 e^- and 20.49 e^-, respectively, while in interface [NH_2-NO] it is 15.57 e^- and 20.41 e^-.

The intra-delocalized ED is also in good agreement between the single and interface systems. For the individual species, the intra-delocalized ED are 34.86 e^- and 35.51 e^- and in interface [NH_2-NO] it is 33.41 e^- and 34.88 e^- for Ph-NH_2 and Ph-NO, respectively. This intra-delocalized ED of the individual molecules is calculated from the data in Chapter 3 and 4 as the total ED minus all localized ED. The combined intra-delocalized ED for the donor and acceptor is 70.37 e^- and 68.29 e^- for the individual and interface systems, respectively. This indicates an error of only ~3%. However, it should be noted that here the GS donor (individual) and ES donor (interface) are compared.

Conclusion and discussion

In this chapter we have successfully calculated electron transfer rate constants with the Marcus equation[24] for four interfaces. For each interface three rate constants were calculated – charge separation in the presence of a light source, in the absence of a light source and charge recombination. These rates compared well with rates of different systems from literature[7],[29] and were within sensible ranges; In the absence of light the recombination rate dominates over the charge separation meaning no current will be generated, but with a photoexcitation the charge separation greatly exceeds the recombination rate indicating that a photocurrent will be generated.

The [NH_2*-C_2H_4NO] interface displayed a vastly superior rate constant of 8.40×10^{13} e^-/s, which is at least two orders of magnitude greater than that of the next best. To decipher the origin of a quicker rate constant, it was separated into the coupling and energetic roots of the Marcus equation. This revealed that the strong electronic coupling between donor and acceptor

© University of Pretoria

greatly contributes to a faster rate of charge separation, while the energetic terms were of similar magnitude for all interfaces. The charge transfer was therefore almost equally favoured thermodynamically in all interfaces. Therefore, in our systems the vastly different coupling strengths was the deciding factor for the tempo of electron transfer.

Clearly the coupling potential, V_{DA}, begs for closer investigation. V_{DA} was further decomposed into its three variables – the transition and static dipole moment and the vertical excitation energy. This decomposition led to the decisive insight that the transition dipole moment is the major cause of the significantly quicker rate constant in interface [NH_2*-C_2H_4NO]. The thermodynamic driving force was also decomposed into its components – Gibbs free energy change and reorganization energy. This provided a practical illustration of the Marcus inverted region and indicated that the rate constant suffers with a $|\Delta G^0 + \lambda_i|$ of more than 1.5 eV. Furthermore, the rate constant was plotted to visualize its dependency on IP_D and EA_A and provided the direct link between Chapters 3 & 4 and Chapter 5. It indicated that small changes in IP_D or EA_A could inflict large changes in the rate of electron transfer and thereby only adds to the value of the investigations performed in Chapters 3 and 4.

FALDI decompositions of the interfaces have been performed with the donor and acceptor each selected as fragment. It was then attempted to connect these results with that of the coupling potential and transition moment. It is concluded that the total electron density transferred from one moiety to another in an electronic transition does not necessarily affect the coupling potential (it will affect the rate constant though). In fact, our results have shown no indication thereof at all. Instead, it is suggested that the change in internal electronic 'structure' of the electron density governs the transition moment and therefore the coupling potential. This agrees with theory that the transition moment is a measure of the charge redistribution in a system due to a charge transfer.[31] This measure thus refers to either the total electron density or the internal restructuring of the electron density, or both.

The change internal electronic 'structure' is expected to be completely described by the FALDI terms; $\Delta DI^D(\mathcal{D},\mathcal{A})$, $\Delta DI^A(\mathcal{D},\mathcal{A})$, $\Delta DI(\mathcal{D},\mathcal{D})$ and $\Delta DI(\mathcal{A},\mathcal{A})$ as well as $\Delta LI(\mathcal{D})$ and $\Delta LI(\mathcal{A})$. The exact link between these terms and transition moment cannot be fully established here as this data set used here is far too limited. Also, these terms provide no hope of finding V_{DA} by only knowing the donor and acceptor and their properties as they are dependent on the initial and final state of the transition in an interface. Finding rate constants therefore remain

© University of Pretoria

burdened by the tedious methodology as described and followed here. It should also be added that this methodology is not infallible as it could not successfully arrive at a proper charge separation transition for one of the interfaces.

The results also suggests that the total electron density transferred from donor to acceptor, as computed by FALDI, is linked to the change in static dipole moment. Although it is an intuitive result, more data points are needed to establish this more concretely for this type of interface systems.

Finally and in addition, our results indicate that FALDI has great potential for providing an alternative way of calculating the transition moment, since it quantifies that what governs the transition moment on a fundamental level.

References

[1] A. Wadsworth, M. Moser, A. Marks, M. S. Little, N. Gasparini, C. J. Brabec, D. Baran, I. McCulloch, *Chem. Soc. Rev.* **2019**, *48*, 1596–1625.

[2] S. Günes, H. Neugebauer, N. S. Sariciftci, *Chem. Rev.* **2007**, *107*, 1324–1338.

[3] S. Zhang, L. Ye, H. Zhang, J. Hou, *Mater. Today* **2016**, *19*, 533–543.

[4] Z. Zheng, O. M. Awartani, B. Gautam, D. Liu, Y. Qin, W. Li, A. Bataller, K. Gundogdu, H. Ade, J. Hou, *Adv. Mater.* **2017**, *29*, 1604241.

[5] D. Lackner, O. Höhn, R. Müller, P. Beutel, P. Schygulla, H. Hauser, F. Predan, G. Siefer, M. Schachtner, J. Schön, J. Benick, M. Hermle, F. Dimroth, *Sol. RRL* **2020**, *4*, 2000210.

[6] V. Lemaur, M. Steel, D. Beljonne, J. L. Brédas, J. Cornil, *J. Am. Chem. Soc.* **2005**, *127*, 6077–6086.

[7] T. Liu, A. Troisi, *J. Phys. Chem. C* **2011**, *115*, 2406–2415.

[8] P. Barbeitas Miranda, *Artic. Phys. Rev. B* **2001**, *64*, DOI 10.1103/PhysRevB.64.081201.

[9] M. Glatthaar, M. Riede, N. Keegan, K. Sylvester-Hvid, B. Zimmermann, M. Niggemann, A. Hinsch, A. Gombert, *Sol. Energy Mater. Sol. Cells* **2007**, *91*, 390–393.

[10] M. Chou, C. Creutz, N. Sutin, *J. Am. Chem. Soc.* **1977**, *99*, 5615–5623.

[11] P. L. A. Popelier, S. Bond, *Springer* **2016**, *170*, 71–118.

[12] I. Cukrowski, D. M. E. van Niekerk, J. H. de Lange, *Struct. Chem.* **2017**, *28*, 1429–1444.

[13] J. H. de Lange, I. Cukrowski, *J. Comput. Chem.* **2018**, *39*, 1517–1530.

© University of Pretoria

[14] J. H. de Lange, D. M. E. van Niekerk, I. Cukrowski, *J. Comput. Chem.* **2018**, *39*, 973–985.

[15] J. H. de Lange, I. Cukrowski, *J. Comput. Chem.* **2017**, *38*, 981–997.

[16] H. Zhou, Y. Wang, F. Wei, D. Wang, Z. Wang, *Appl. Catal. A Gen.* **2008**, *348*, 135–141.

[17] P. Song, Y. Li, F. Ma, T. Pullerits, M. Sun, *J. Phys. Chem. C* **2013**, *117*, 15879–15889.

[18] J. Zheng, Y. K. Kang, M. J. Therien, D. N. Beratan, *J. Am. Chem. Soc.* **2005**, *127*, 11303–11310.

[19] R. J. Cave, M. D. Newton, *Chem. Phys. Lett.* **1996**, *249*, 15–19.

[20] M. J. Frisch, G. W. Trucks, H. B. Schlegel, G. E. Scuseria, M. A. Robb, J. R. Cheeseman, G. Scalmani, V. Barone, G. A. Petersson, H. Nakatsuji, M. C. , X. Li, A. Marenich, J. Bloino, B. G. Janesko, R. Gomperts, B. Mennucci, H. P. Hratchian, J. V. Ortiz, A. F. Izmaylov, J. L. Sonnenberg, D. Williams-Young, F. Ding, F. Lipparini, F. Egidi, J. Goings, B. Peng, A. Petrone, T. Henderson, D. Ranasinghe, V. G. Zakrzewski, J. Gao, N. Rega, G. Zheng, W. Liang, M. Hada, M. Ehara, K. Toyota, R. Fukuda, J. Hasegawa, M. Ishida, T. Nakajima, Y. Honda, O. Kitao, H. Nakai, T. Vreven, K. Throssell, J. A. Montgomery, J. E. Peralta, F. Ogliaro, M. Bearpark, J. J. Heyd, E. Brothers, K. N. Kudin, V. N. Staroverov, T. Keith, R. Kobayashi, J. Normand, K. Raghavachari, A. Rendell, J. C. Burant, S. S. Iyengar, J. Tomasi, M. Cossi, J. M. Millam, M. Klene, C. Adamo, R. Cammi, J. W. Ochterski, R. L. Martin, K. Morokuma, O. Farkas, J. B. Foresman, D. J. Fox, **2016**.

[21] W. Koch, M. C. Holthausen, *A Chemist's Guide to Density Functional Theory*, Wiley-VCH, **2001**.

[22] T. A. Keith, **2019**.

[23] W. Humphrey, A. Dalke, K. Schulten, *J. Mol. Graph.* **1996**, *14*, 33–38.

[24] R. A. Marcus, *Rev. Mod. Phys.* **1993**, *65*, 599–610.

[25] T. Lu, F. Chen, *Artic. J. Comput. Chem.* **2012**, *33*, 580–592.

[26] A. Troisi, *Chem. Soc. Rev.* **2011**, *40*, 2347–2358.

[27] T. Liu, A. Troisi, *Adv. Mater.* **2013**, *25*, 1038–1041.

[28] Q. Lu, M. Qiu, M. Zhao, Z. Li, Y. Li, *Polymers (Basel).* **2019**, *11*, 958.

[29] Q. Wang, Y. Li, P. Song, R. Su, F. Ma, Y. Yang, **n.d.**, DOI 10.3390/polym9120692.

[30] R. Dennington, T. A. Keith, J. M. Millam, **2016**.

[31] P. Atkins, J. de Paula, *Atkins' Physical Chemistry*, Oxford University Press, **2014**.

© University of Pretoria

Chapter 6 – Conclusions

In this project we worked from studying properties of individual donor and acceptor molecules, towards that of interfaces built for charge transfer simulation for calculation of rate constants. The electronic structure of a molecule and the change thereof due to either a change in molecular structure or ionization, is an immensely important characteristic of molecules for electron transfer purposes and constitutes a core theme in this project. In this work it was demonstrated how the FALDI electron density decomposition scheme can be implemented to give an in-depth atomistic description of the electronic structure of ground state molecules as well as ionic states.

In Chapter 3 the electron donor molecules were analysed and in Chapter 4 the acceptor molecules. Some of these molecules were used to construct the charge transfer simulating interfaces used in Chapter 5 – from these the electron transfer rates were calculated.

The donor molecules had the basic structure of Ph-XR_2, where X is either nitrogen or phosphorus and R is hydrogen, methyl, ethyl, or propyl. This selection provides eight combinations thus eight unique molecules of which the electronic structure was decomposed using the FALDI decomposition scheme. Hereby the isolated effects of nitrogen and phosphorus as well as that of different alkyl chain lengths could be revealed which was in turn compared to the physical properties of the molecules. This led to a discovery of a close relationship between the number of electrons shared between phenyl and its functional group and the ionization potential; By increasing the inter-fragment electron delocalization between the phenyl ring and its substituent, the ionization potential decreases. To our knowledge, this has never been documented before.

Upon closer inspection, it is the alkyl chains that increasingly interact with the phenyl ring as they become longer. This increased long-range effect therefore lowers the IP. From the ionization analysis, where exactly the electron was removed from could be traced back to the region within the molecules as well as to the component of the electronic structure. This revealed that the electron was removed mainly from the electron density delocalized within the phenyl and from that within the alkyl groups, depending on their length. The strengthening of the Ph···R interactions therefore lowered the energy barrier for the rest of the electrons on these fragments to be removed by ionization. The Ph···R interaction was also much higher than we would classically anticipate. These findings therefore highlighted the significance of such long-range interactions in these kinds of molecules.

© University of Pretoria

The increased alkyl lengths did not shift significant electron density unto the phenyl, thus the mechanism of sharing between phenyl and R-group cannot be due to the inductive effect and should be accounted for by resonance. This suggests that the mechanism of Ph···R interaction is by means of hyperconjugation and therefore that hyperconjugation is linked to the ionization potential. When nitrogen was replaced with phosphorus, the inter-fragment delocalized electron density decreased and thereby – in line with our hypothesis – increased the ionization potential. This decrease in interfragment delocalization is caused by phosphorus sharing less with the phenyl ring than nitrogen and is explained by Bent's rule which states that s-character is concentrated in orbitals directed towards electropositive atoms.[1] Since phosphorus is less electronegative than nitrogen, its three adjacent carbons is relatively more electronegative meaning the bonds with them has a hybridization closer to sp^3 than sp^2. This could be observed in the bond angles of Ph-PR_2 molecules compared to nitrogen-based ones – with phosphorus the heteroatom is trigonal pyramidal while with nitrogen it is closer to trigonal planar. Phosphorus' lone pair therefore has much less p-character and thereby does not delocalize as effectively into the conjugated system of the phenyl ring. This was observed in the FALDI results; in other words, the effect of Bent's rule could also be recovered and quantified with FALDI.

In Chapter 4 two kinds of molecules with generic structures Ph-RNO, where R is none, CH_2, C_2H_4 or C_2H_2, and Ph-X, where X is F, Cl or Br, were analysed. For these molecules more correlations between electron populations and ionization energies were discovered. For benzene molecules substituted with a nitroso-group and varying alkyl lengths, electron attachment became increasingly spontaneous as the electron delocalization between the phenyl and substituent increased. No such trend was displayed by the set of halogenated benzene molecules. Furthermore, there is also a correlation between the electron affinity and the electron population on the phenyl ring. For nitroso-substituted benzene molecules, as more electron density was accumulated on the phenyl ring the electron attachment became less spontaneous. However, an opposite trend was observed for the halogenated benzenes – as phenyl electron population increased less energy was required to add an electron to the molecule. This is also, to our knowledge, the first time these relationships are demonstrated. The mechanism of these correlations could not be deciphered with our limited number of data points.

For the halogenated benzene molecules, lone-pair electrons of the halogens partaking in resonance could be quantified. When atoms expected to have lone-pair electrons have less

© University of Pretoria

localized electron density than classically expected, the lone-pair electrons are assumed to be delocalized towards other atoms in the molecule. In this way, counting the number of missing localized electrons on some lone-pair-carrying atom, will give the number of lone-pair electrons shared by resonance (conjugation) through the molecule. It is generally the case that the core electron count remains constant despite dramatic changes in the molecule which justifies assigning the missing electrons only to shared lone-pairs. This principle was applied to the lone-pair electrons on the halogens in halogenated benzene molecules. It was found that more than one lone-pair electron is shared with the phenyl ring in the molecules Ph-Cl and Ph-Br.

Furthermore, from the nitroso-substituted molecules it was learned that a very electron withdrawing group closely participating in a conjugated system causes a tremendous number of electrons to be delocalized within that system. It is therefore hypothesised that maximum delocalization is achieved when an electron donating and withdrawing group is linked in a short conjugated system. Also, it is suggested that the effect of a functional group on the electronic structure of a molecule (therefore the properties attributed to the molecule due to the functional group) can be 'diluted' by placing the functionality further away from the molecule by means of -CH- units – lengthening the conjugated system, therefore. This can serve as a useful tool for finetuning some physical property of a molecule. Furthermore, it was recovered from the FALDI results that a fully conjugated system has indeed the most delocalized electrons.

Finally, in Chapter 5 the donors Ph-NH_2 and Ph-NPr_2 and acceptors Ph-NO and Ph-C_2H_4NO were used to build four interfaces to mimic the heterojunction in organic solar cells. There are many factors that influence the efficiency of organic solar cells among which the rate of electron transfer between the donor and the acceptor is one.[2] This rate of charge transfer is calculated for the model interfaces by making use of the Nobel prize winning Marcus theory.[3] Marcus theory is described by the Marcus equation which is a function of several variables specific to the interfaces studied. A methodology adjusted but strongly based on literature[4–7] was implemented to calculate these parameters. This led to the successful calculation of charge separation rate constants in the presence and absence of a light source as well as charge recombination rates. Our calculations of the rates suggest that all interfaces would generate a current with photoexcitations but not without it, which is coherent with the functioning of a solar cell. Surprisingly, large discrepancies in rate constants were obtained for the relatively similar interface systems. Interface [NH_2*-C_2H_4NO] displayed a charge separation rate of at least two orders of magnitude greater than that of the second quickest rate. To find the origin

© University of Pretoria

thereof, the rates were separated into their energetic and electronic coupling contributions. This revealed that the coupling in [NH_2*-C_2H_4NO] is vastly different, while, for these four systems, the energetic driving forces were very similar. The coupling potential, the term indicating the strength of the electronic coupling between donor and acceptor, was further decomposed into its contributions. These are the transition dipole moment, the change in static dipole moment and the change in energy associated with the coupling – the vertical excitation energy. The transition dipole moment of [NH_2*-C_2H_4NO] was found to differ the most from the other interfaces. This was to such an extent that the vastly quicker rate for [NH_2*-C_2H_4NO] could practically be ascribed to its transition dipole moment being of much greater magnitude.

The thermodynamic driving force, the Marcus equation where the coupling potential is excluded, was also separated into its system linked controlling variables – the Gibbs free energy change and the reorganization energy. It was found that the having $|\Delta G^0 + \lambda|$ at 1.5 eV or greater leads to a severe decline in the rate of charge transfer. The reorganization energy was found to be relatively constant around 0.5 eV whilst ΔG^0 varied substantially. Despite this, the thermodynamic driving force was found to be relatively similar between the interfaces.

The direct dependency between the rate of electron transfer and the ionization potential of the donor and electron attachment energy of the acceptor was plotted as a 3D surface in space. This provided a more intuitive and visual understanding of how these dependencies behave and is key to providing the link between Chapters 3 & 4 and Chapter 5 – the tunability of IP & EA and the dependency of k_{CS} on IP and EA. These plots suggested that the rate is quite sensitive towards adjustments in IP_D and in EA_A and shows that for the given reorganization energies there are potential to double the rate by simply changing IP_D or EA_A. However, this could not provide the full picture of how k_{CS} changes with IP_D and EA_A, as these can be changed in more than one way.

FALDI analyses were also performed on the four interfaces, for which the donor and acceptor was considered the interacting fragments – a 2-fragment scheme was therefore used. These electron density decompositions were matched up with their corresponding coupling potentials and transition moments. Here it was found that there is a definite link between FALDI results and transition moment. The results for [NH_2*-C_2H_4NO], which boasts the greatest transition moment, was distinctly different from the rest of the interfaces. It indicates that the transition moment is linked to the magnitude of change of the FALDI terms and how

© University of Pretoria

they change relative to each other. This exact correlation could not be established, however, due to the lack of a large and diverse data set.

Further close examination of the FALDI results indicated that the transition moment is not necessarily dictated by the total amount of electron density transferred, which might be what it is expected to depend on as it is defined as a measure of charge redistribution.[8] Rather, the results suggest it is determined by the way in which the electronic structure is changed by the charge transfer. Based on this, the redistribution, therefore, refers to that due to change in electronic structure and not the total charge redistributed from donor to acceptor necessarily. Although the total charge redistribution does matter for the eventual charge separation efficiency, it does not affect the transition moment and thus the coupling potential. The transition dipole moment is therefore described by the change in electronic structure.

Now, if FALDI provides a complete description of the electronic structure of a molecule and the change thereof, all information about the transition dipole moment should in principle be contained in the FALDI results. In other words, FADLI hereby shows great potential for an alternative way of calculating the transition moment and provides a new facet for visualizing it as well. This is a remarkable outcome of this work and is strongly encouraged to be unravelled in future studies as it would connect FALDI with the spectroscopic properties of molecules. With this the findings of the project are concluded.

For the findings in this work to be established more firmly and elaborate in the future and to reveal whether these phenomena are specific to our selected molecules or generalizable for more systems, it is of most import to enlarge and diversify the molecular database. This would allow the relationships between energetic properties and electron populations as discovered in chapters 3 and 4, and the link between the transition moment and change of electronic structure, to be fully explored, understood, and finally, applied. This work serves as an invaluable pilot study giving strong indications that there are relationships to be established for the use as future tools in designing purpose specific compounds. The specific relationships suggested to study is that between the ionization energy (IP and EA) and electron populations (localized or delocalized) in a molecule as well as that between the transition dipole moment and the intricacies of change in electronic structure. Exactly how electron populations and electronic structures are determined by the molecular structure and elements should obviously be thoroughly understood as well, to complete the link between synthetic chemist and good rate constants. Hence it is also recommended that the FALDI terms is studied on a large and diverse

© University of Pretoria

set of molecules with various fragment combinations. However, these suggested analyses are exhaustingly labour intensive and time consuming. It is therefore inevitable that machine learning algorithms should eventually be employed to gather and decipher the information to arrive at meaningful applications.

There are a few aspects that could be done differently to add reliability to the results or potentially add depth of understanding. Firstly, there were recently improvements to the algorithms of FALDI. The LO-algorithm used in this work only accounts for the unphysical localized overlap but not the localized-delocalized overlap which is incorporated in the LDO-algorithm. The new algorithm was not implemented here as it was only available when the project was already in a developed stage. Furthermore, applying a 4-fragment density decomposition scheme to the interfaces – such that the donor and acceptor functional groups and the two phenyl rings are fragments – would have been helpful to compare with the FALDI results of Chapter 3 and 4. For simplicity and time constraints this was not followed through. Also, to improve validity of the results, a proper method validation for the calculation of the rate constants should be performed. For one of the interfaces no proper charge transfer state could be obtained, which is a possible indicator that the method is partially flawed. However, it is not necessarily the case that all interfaces possess a transition that adds an electron from the donor to the acceptor. Another improvement will be to use the augmented cc-pVTZ basis set, instead of augmented cc-pVDZ, to do all initial optimizations and energy calculations. This would allow more flexibility in wavefunction energy minimizations, however, these calculations proved to fail more often and is significantly more time consuming. Finally, for the calculation of more physically accurate rate constants, a more elaborate calculation could be used such as including the external reorganization energy. This project is more concerned with the relative rates, however, thus this is beyond the scope of our project.

References

[1] † V. Jonas, and C. Boehme, G. Frenking*, *Inorg. Chem.* **1996**, *35*, 2097–2099.

[2] M. Glatthaar, M. Riede, N. Keegan, K. Sylvester-Hvid, B. Zimmermann, M. Niggemann, A. Hinsch, A. Gombert, *Sol. Energy Mater. Sol. Cells* **2007**, *91*, 390–393.

[3] M. Chou, C. Creutz, N. Sutin, *J. Am. Chem. Soc.* **1977**, *99*, 5615–5623.

[4] A. Troisi, *Chem. Soc. Rev.* **2011**, *40*, 2347–2358.

[5] T. Liu, A. Troisi, *Adv. Mater.* **2013**, *25*, 1038–1041.

© University of Pretoria

[6] T. Liu, A. Troisi, *J. Phys. Chem. C* **2011**, *115*, 2406–2415.

[7] Q. Lu, M. Qiu, M. Zhao, Z. Li, Y. Li, *Polymers (Basel).* **2019**, *11*, 958.

[8] P. Atkins, J. de Paula, *Atkins' Physical Chemistry*, Oxford University Press, **2014**.

© University of Pretoria

Supplementary Information (SI)

Stefan Lambert Koning MSc

Contents

Chapter 3

Table S3.1. Vertical IP vs Proper IP 111
Table S3.2. Electron populations for cationic Ph-NR_2 112
Table S3.3. Inter-delocalized EDs for cationic Ph-NR_2 113
Table S3.4. Change in Ph ED in Ph-NR_2 due to R change 113
Table S3.5. Electron populations for GS Ph-PR_2 114
Table S3.6. Electron population change upon ionization for Ph-XR_2 114
Table S3.7. Inter-delocalized EDs for GS Ph-PR_2 115
Table S3.8. Change in Ph ED in Ph-PR_2 due to R change 115
Tables S3.9-S3.16.Atom coordinates for Ph-XR_2 115-121

Chapter 4

Table S4.1. Electron populations for anionic Ph-X 122
Table S4.2. Electron populations for anionic Ph-RNO 123
Table S4.3. Electron populations for ground state Ph-COX 123
Figure S4.1. EA vs DI($\mathcal{F}_1$,$\mathcal{F}_2$) for ground state Ph-COX 124
Table S4.4. Electron populations for ground state Ph-OR 124
Figure S4.2. EA vs DI($\mathcal{F}_1$,$\mathcal{F}_2$) for ground state Ph-OR 124

Chapter 5

Figure S5.1. Justification for DI(D) and DI(A) change visualization 125
Excitation information of interfaces 125-129
Figure S5.2. Summary of [NH_2-NO] isosurfaces 126
Figure S5.3. Summary of [NH_2-C_2H_4NO] isosurfaces 127
Figure S5.4. Summary of [NPr_2-NO] isosurfaces 128
Figure S5.5. Summary of [NPr_2-C_2H_4NO] isosurfaces 129

© University of Pretoria

Chapter 3 SI

Table S3.1. Comparison of calculated vertical IP (no geometry change) and proper IP (molecule allowed to optimize) of selected moieties

Molecule	**Vertical IP (eV)**	**Proper IP (eV)**	**Difference (eV)**
Ph-NH_2	7.891	7.538	-0.354
Ph-NMe_2	7.238	7.075	-0.190
Ph-PH_2	8.680	8.245	-0.435

© University of Pretoria

Table S3.2. Electron population per fragment for Ph-NR_2 molecules in cationic state.

	Ph-NH_2			Ph-NMe_2			Ph-NEt_2			Ph-NPr_2		
Fragment	**Phenyl-**	**-N-**	**-H_2**	**Phenyl-**	**-N-**	**-Me_2**	**Phenyl-**	**-N-**	**-Et_2**	**Phenyl-**	**-N-**	**-Pr_2**
Total	39.916	8.095	0.990	40.089	8.039	16.872	40.112	8.053	32.835	40.125	8.055	48.820
Localized $LI_{GS}(\mathcal{F})$	11.980	3.255	0.000	11.975	2.282	3.985	11.974	2.271	7.980	11.973	2.153	11.974
Intra-delocalized $DI_{GS}(\mathcal{F},\mathcal{F})$	26.171	-	0.016	25.767	-	9.983	25.589	-	21.593	25.526	-	33.477
Inter-delocalized $DI_{GS}^{\mathcal{F}}(\mathcal{F},\mathcal{F}_X)$	1.765	4.839	0.974	2.347	5.757	2.906	2.549	5.782	3.263	2.626	5.902	3.369

© University of Pretoria

Table S3.3. Inter-fragment delocalised density for Ph-NR_2 molecules in cationic state

	Fragments		Inter-fragment delocalised ED, $DI_{GS}(\mathcal{F}_A, \mathcal{F}_B)$	$DI_{GS}(\mathcal{F}_1, \mathcal{F}_2)$
Ph-NH_2	-N-	-H_2	2.818	4.760
	Phenyl-	-N-	4.514	
	Phenyl-	-H_2	0.246	
Ph-NMe_2	-N-	-Me_2	5.377	5.633
	Phenyl-	-N-	3.961	
	Phenyl-	-Me_2	1.672	
Ph-NEt_2	-N-	-Et_2	5.700	5.893
	Phenyl-	-N-	3.707	
	Phenyl-	-Et_2	2.187	
Ph-NPr_2	-N-	-Pr_2	5.927	5.971
	Phenyl-	-N-	3.649	
	Phenyl-	-Pr_2	2.322	

Table S3.4. ED change on phenyl in the Ph-NR_2 molecule due to the change in alkyl length

	GS-optimized			Cationic at neutral geometry		
	Ph-NH_2 → Ph-NMe_2	**Ph-NH_2 → Ph-NEt_2**	**Ph-NH_2 → Ph-NPr_2**	**Ph-NH_2 → Ph-NMe_2**	**Ph-NH_2 → Ph-NEt_2**	**Ph-NH_2 → Ph-NPr_2**
Total	0.039	0.042	0.043	0.174	0.196	0.210
Localised	-0.004	-0.005	-0.005	-0.005	-0.006	-0.007
Intra-delocalised	-0.585	-0.743	-0.824	-0.404	-0.582	-0.645
Inter-delocalised	0.628	0.790	0.873	0.582	0.784	0.861

© University of Pretoria

Table S3.5. Electron population per fragment for ground state Ph-PR_2 molecules

	Ph-PH_2			Ph-PMe_2			Ph-PEt_2			Ph-PPr_2		
Fragment	**Phenyl-**	**-P-**	**-H_2**	**Phenyl-**	**-P-**	**-Me_2**	**Phenyl-**	**-P-**	**-Et_2**	**Phenyl-**	**-P-**	**-Pr_2**
Total	41.559	13.332	3.109	41.601	13.304	19.094	41.594	13.344	35.061	41.599	13.344	51.057
Localized	11.982	10.782	0	11.981	10.320	3.997	11.980	10.151	7.993	11.980	10.010	11.988
Intra-delocalized	27.681	-	0.250	27.255	-	11.665	27.058	-	23.509	26.993	-	35.479
Inter-delocalized	1.896	2.550	2.859	2.365	2.984	3.432	2.555	3.192	3.558	2.625	3.335	3.590

Table S3.6. Electron population *change* upon ionization for Ph-XR_2 molecules

		Ph-XH_2			Ph-XMe_2			Ph-XEt_2			Ph-XPr_2		
	Fragment	**Phenyl-**	**-X-**	**-H_2**	**Phenyl-**	**-X-**	**-Me_2**	**Phenyl-**	**-X-**	**-Et_2**	**Phenyl-**	**-X-**	**-Pr_2**
X = N	**Total**	-0.718	-0.123	-0.158	-0.583	-0.093	-0.324	-0.564	-0.102	-0.334	-0.552	-0.103	-0.345
	Localized	0.000	0.098	0.000	-0.001	0.264	-0.003	-0.001	0.272	-0.004	-0.001	0.154	-0.005
	Intra-Deloc	-0.802	-	-0.007	-0.621	-	-0.203	-0.642	-	-0.295	-0.623	-	-0.334
	Inter-Deloc	0.085	-0.222	-0.151	0.038	-0.357	-0.116	0.079	-0.374	-0.034	0.073	-0.257	-0.005
X = P	**Total**	-0.644	-0.183	-0.172	-0.395	-0.259	-0.347	-0.326	-0.254	-0.418	-0.321	-0.242	-0.437
	Localized	0.008	-0.408	0.000	0.000	-0.043	0.000	0.000	0.057	0.000	0.000	0.135	0.000
	Intra-Deloc	-0.736	-	-0.033	-0.500	-	-0.500	-0.407	-	-0.572	-0.435	-	-0.651
	Inter-Deloc	0.084	0.225	-0.139	0.104	-0.215	0.153	0.081	-0.311	0.154	0.114	-0.377	0.215

© University of Pretoria

Table S3.7. Inter-fragment delocalized density for ground state Ph-PR_2 molecules

	Fragments		Inter-fragment delocalised ED, $DI_{GS}(\mathcal{F}_A, \mathcal{F}_B)$	$DI_{GS}(\mathcal{F}_1, \mathcal{F}_2)$
Ph-PH_2	-P-	-H_2	3.350	3.955
	-P-	Phenyl-	2.608	
	-H_2	Phenyl-	1.347	
Ph-PMe_2	-P-	-Me_2	3.979	4.802
	-P-	Phenyl-	2.576	
	-Me_2	Phenyl-	2.226	
Ph-PEt_2	-P-	-Et_2	4.202	5.104
	-P-	Phenyl-	2.523	
	-Et_2	Phenyl-	2.581	
Ph-PPr_2	-P-	-Pr_2	4.365	5.186
	-P-	Phenyl-	2.524	
	-Pr_2	Phenyl-	2.662	

Table S3.8. ED change on phenyl in the Ph-NR2 molecule due to the change in alkyl length

	GS-optimized			**Cationic at neutral geometry**		
	Ph-PH_2 → Ph-PMe_2	**Ph-PH_2 → Ph-PEt_2**	**Ph-PH_2 → Ph-PPr_2**	**Ph-PH_2 → Ph-PMe_2**	**Ph-PH_2 → Ph-PEt_2**	**Ph-PH_2 → Ph-PPr_2**
Total	0.042	0.035	0.039	0.291	0.353	0.364
Localised	-0.001	-0.002	-0.002	-0.009	-0.010	-0.010
Intra-delocalised	-0.426	-0.623	-0.688	-0.189	-0.293	-0.386
Inter-delocalised	0.470	0.660	0.729	0.489	0.657	0.760

Table S3.9. Atom coordinates for Ph-NH_2 (Å)

Atom		x	y	z
C	1	-1.1687	1.1997	0.0037
C	2	-1.8773	0.0000	0.0076
C	3	-1.1687	-1.1997	0.0037
C	4	0.2215	-1.2050	-0.0045
C	5	0.9349	0.0000	-0.0080
C	6	0.2215	1.2050	-0.0045
H	7	-1.7050	2.1488	0.0069
H	8	-2.9661	0.0000	0.0139
H	9	-1.7050	-2.1488	0.0069
H	10	0.7639	-2.1514	-0.0137
H	11	0.7639	2.1514	-0.0137
N	12	2.3288	0.0000	-0.0715
H	13	2.7838	0.8401	0.2559
H	14	2.7838	-0.8401	0.2559

© University of Pretoria

Table S3.10. Atom coordinates for Ph-NMe_2 (Å)

Atom		x	y	z
C	1	-1.9358	-1.1954	0.0175
C	2	-2.6486	0.0000	0.0401
C	3	-1.9358	1.1954	0.0176
C	4	-0.5467	1.2047	-0.0338
C	5	0.1833	0.0000	-0.0737
C	6	-0.5467	-1.2047	-0.0338
H	7	-2.4680	-2.1465	0.0442
H	8	-3.7365	0.0000	0.0826
H	9	-2.4680	2.1465	0.0443
H	10	-0.0334	2.1617	-0.0426
H	11	-0.0335	-2.1617	-0.0427
N	12	1.5685	0.0000	-0.1635
C	13	2.2844	1.2371	0.0638
H	14	2.1152	1.6507	1.0741
H	15	3.3559	1.0560	-0.0597
H	16	1.9934	1.9990	-0.6703
C	17	2.2844	-1.2371	0.0639
H	18	1.9936	-1.9991	-0.6703
H	19	3.3559	-1.0560	-0.0594
H	20	2.1150	-1.6507	1.0742

© University of Pretoria

Table S3.11. Atom coordinates for Ph-NEt_2 (Å)

Atom		x	y	z
C	1	-2.4643	1.1415	0.3503
C	2	-3.1799	-0.0001	0.0000
C	3	-2.4643	-1.1416	-0.3503
C	4	-1.0747	-1.1513	-0.3497
C	5	-0.3383	0.0000	0.0001
C	6	-1.0748	1.1512	0.3498
H	7	-2.9955	2.0532	0.6246
H	8	-4.2684	-0.0001	-0.0001
H	9	-2.9953	-2.0534	-0.6247
H	10	-0.5653	-2.0744	-0.6105
H	11	-0.5654	2.0743	0.6106
N	12	1.0452	0.0000	0.0001
C	13	1.8065	-1.1391	-0.4782
H	14	2.7595	-0.7583	-0.8690
H	15	1.2910	-1.5874	-1.3366
C	16	1.8064	1.1393	0.4782
H	17	1.2909	1.5877	1.3366
H	18	2.7595	0.7587	0.8689
C	19	2.0796	2.1959	-0.5912
H	20	2.6678	3.0238	-0.1733
H	21	2.6450	1.7650	-1.4275
H	22	1.1442	2.6038	-0.9921
C	23	2.0800	-2.1958	0.5911
H	24	2.6452	-1.7648	1.4275
H	25	1.1449	-2.6042	0.9919
H	26	2.6686	-3.0233	0.1729

© University of Pretoria

Table S3.12. Atom coordinates for Ph-NPr_2 (Å)

Atom		x	y	z
C	1	-2.9470	1.1412	0.3509
C	2	-3.6626	-0.0001	0.0000
C	3	-2.9469	-1.1415	-0.3509
C	4	-1.5574	-1.1511	-0.3500
C	5	-0.8208	0.0000	0.0000
C	6	-1.5575	1.1510	0.3500
H	7	-3.4780	2.0528	0.6260
H	8	-4.7512	-0.0002	0.0000
H	9	-3.4778	-2.0530	-0.6260
H	10	-1.0479	-2.0737	-0.6119
H	11	-1.0480	2.0736	0.6119
N	12	0.5626	0.0000	0.0000
C	13	1.3221	-1.1419	-0.4710
H	14	2.2809	-0.7688	-0.8575
H	15	0.8119	-1.5945	-1.3318
C	16	1.3220	1.1420	0.4710
H	17	0.8117	1.5946	1.3318
H	18	2.2809	0.7690	0.8575
C	19	1.5898	2.2029	-0.5980
H	20	2.1361	1.7359	-1.4298
H	21	0.6331	2.5473	-1.0117
C	22	1.5901	-2.2028	0.5980
H	23	2.1363	-1.7357	1.4298
H	24	0.6334	-2.5473	1.0117
C	25	2.3840	-3.3836	0.0504
H	26	3.3561	-3.0601	-0.3474
H	27	2.5752	-4.1307	0.8303
H	28	1.8416	-3.8835	-0.7642
C	29	2.3836	3.3838	-0.0504
H	30	3.3557	3.0604	0.3474
H	31	2.5748	4.1310	-0.8303
H	32	1.8411	3.8837	0.7641

© University of Pretoria

Table S3.13. Atom coordinates for Ph-PH_2 (Å)

Atom		x	y	z
C	1	1.6255	-1.1978	0.0036
C	2	2.3173	0.0099	0.0163
C	3	1.6101	1.2103	0.0069
C	4	0.2179	1.2026	-0.0054
C	5	-0.4879	-0.0053	-0.0156
C	6	0.2325	-1.2039	-0.0218
H	7	2.1714	-2.1411	0.0036
H	8	3.4069	0.0168	0.0282
H	9	2.1456	2.1596	0.0120
H	10	-0.3232	2.1485	-0.0054
H	11	-0.3002	-2.1551	-0.0520
P	12	-2.3358	-0.0997	-0.0563
H	13	-2.5747	0.1051	1.3391
H	14	-2.5821	1.2670	-0.3850

Table S3.14. Atom coordinates for Ph-PMe_2 (Å)

Atom		x	y	z
C	1	-2.3780	-1.0572	-0.2167
C	2	-2.9285	0.1597	0.1816
C	3	-2.0968	1.2587	0.3733
C	4	-0.7212	1.1418	0.1774
C	5	-0.1552	-0.0731	-0.2190
C	6	-1.0068	-1.1662	-0.4248
H	7	-3.0219	-1.9217	-0.3780
H	8	-4.0034	0.2512	0.3355
H	9	-2.5196	2.2159	0.6783
H	10	-0.0929	2.0161	0.3373
H	11	-0.5899	-2.1168	-0.7617
C	12	2.3536	1.3571	-0.3020
H	13	2.1069	1.8070	0.6688
H	14	3.4451	1.2806	-0.3786
H	15	2.0101	2.0189	-1.1062
C	16	2.1333	-1.0737	1.1169
H	17	1.6725	-2.0621	1.2279
H	18	3.2226	-1.2047	1.1445
H	19	1.8245	-0.4410	1.9594
P	20	1.6496	-0.3418	-0.5232

© University of Pretoria

Table S3.15. Atom coordinates for Ph-PEt_2 (Å)

Atom		x	y	z
C	1	2.8786	0.3800	-0.8485
C	2	3.2629	-0.2137	0.3515
C	3	2.2904	-0.7222	1.2082
C	4	0.9412	-0.6298	0.8717
C	5	0.5391	-0.0360	-0.3289
C	6	1.5305	0.4560	-1.1871
H	7	3.6326	0.7735	-1.5301
H	8	4.3178	-0.2854	0.6151
H	9	2.5830	-1.1928	2.1467
H	10	0.2008	-1.0298	1.5620
H	11	1.2404	0.8986	-2.1411
C	12	-2.1521	-0.9903	0.2422
H	13	-3.2052	-0.6891	0.1466
H	14	-1.8832	-0.8391	1.2956
C	15	-1.6433	1.8194	-0.1642
H	16	-1.0439	2.5464	-0.7289
H	17	-2.6889	2.0073	-0.4487
C	18	-1.4526	2.0322	1.3346
H	19	-1.7011	3.0657	1.6103
H	20	-2.1008	1.3727	1.9244
H	21	-0.4144	1.8471	1.6352
C	22	-1.9983	-2.4607	-0.1448
H	23	-2.3103	-2.6292	-1.1832
H	24	-0.9558	-2.7911	-0.0544
H	25	-2.6101	-3.1025	0.5022
P	26	-1.2159	0.1492	-0.8906

© University of Pretoria

Table S3.16. Atom coordinates for Ph-PPr_2 (Å)

Atom		x	y	z
C	1	3.1485	-0.6848	-0.9469
C	2	3.4769	-1.0837	0.3471
C	3	2.4779	-1.1664	1.3125
C	4	1.1607	-0.8423	0.9908
C	5	0.8156	-0.4378	-0.3021
C	6	1.8296	-0.3782	-1.2673
H	7	3.9211	-0.6255	-1.7134
H	8	4.5065	-1.3363	0.5992
H	9	2.7239	-1.4837	2.3257
H	10	0.4017	-0.9114	1.7672
H	11	1.5793	-0.0946	-2.2907
C	12	-1.9520	-0.4159	0.6054
H	13	-2.8802	0.1602	0.4742
H	14	-1.4979	-0.0570	1.5376
C	15	-0.8281	1.8687	-0.7406
H	16	-0.1308	2.1963	-1.5251
H	17	-1.8208	2.2244	-1.0558
C	18	-0.4400	2.5011	0.5934
H	19	-1.1733	2.2255	1.3629
H	20	0.5259	2.0952	0.9220
C	21	-2.2916	-1.9073	0.7157
H	22	-1.3667	-2.5006	0.6878
H	23	-2.7407	-2.0904	1.7025
P	24	-0.8916	0.0046	-0.8668
C	25	-0.3516	4.0231	0.5089
H	26	-1.3130	4.4603	0.2058
H	27	-0.0749	4.4593	1.4774
H	28	0.4026	4.3339	-0.2271
C	29	-3.2463	-2.4006	-0.3683
H	30	-3.4580	-3.4706	-0.2482
H	31	-4.2030	-1.8619	-0.3208
H	32	-2.8259	-2.2481	-1.3699

© University of Pretoria

Chapter 4 SI

Table S4.1. Electron population per fragment for Ph-X molecules in anionic state

Fragment	Ph-F		Ph-Cl		Ph-Br	
	Phenyl-	**-F**	**Phenyl-**	**-Cl**	**Phenyl-**	**-Br**
Total $N(\mathcal{F})$	41.318	9.681	41.606	17.394	41.683	35.317
Localized $\mathrm{LI_{GS}}(\mathcal{F})$	11.976	7.466	11.982	14.941	11.983	33.021
Intra-delocalized $\mathrm{DI_{GS}}(\mathcal{F},\mathcal{F})$	28.122	-	28.156	-	28.197	-
Inter-delocalized $\mathrm{DI}_{\mathrm{GS}}^{\mathcal{F}}(\mathcal{F},\mathcal{F}_X)$	1.221	2.215	1.467	2.453	1.503	2.296
$\mathrm{DI_{GS}}(\mathcal{F}_1, \mathcal{F}_2)$	3.436		3.920		3.799	

© University of Pretoria

Table S4.2. Electron population per fragment for Ph-RNO molecules in anionic state

	Ph-NO		Ph-CH_2NO			Ph-C_2H_4NO			Ph-C_2H_2NO		
Fragment	**Phenyl-**	**-NO**	**Phenyl-**	**-CH_2-**	**-NO**	**Phenyl-**	**-C_2H_4-**	**-NO**	**Phenyl-**	**-C_2H_2-**	**-NO**
Total $N(\mathcal{F})$	41.056	15.944	41.231	7.801	15.967	41.187	15.763	16.051	41.297	13.792	15.911
Localized $\mathrm{LI_{GS}}(\mathcal{F})$	11.981	8.711	11.981	1.996	8.473	11.981	3.994	8.974	11.982	3.992	8.806
Intra-delocalized $\mathrm{DI_{GS}}(\mathcal{F},\mathcal{F})$	26.943	3.557	26.953	3.040	3.653	26.991	8.466	3.590	26.94	5.987	3.557
Inter-delocalized $\mathrm{DI_{GS}^{\mathcal{F}}}(\mathcal{F},\mathcal{F}_X)$	2.132	3.676	2.297	2.765	3.841	2.215	3.303	3.486	2.371	3.813	3.547

Table S4.3. Electron population per fragment for Ph-COX molecules in ground state

	Ph-COH		Ph-COOH		Ph-COOMe		Ph-COOEt	
Fragment	**Ph-**	**-COH**	**Ph-**	**-COOH**	**Ph-**	**-COOMe**	**Ph-**	**-COOEt**
Total $N(\mathcal{F})$	40.909	15.091	40.839	23.161	40.859	31.141	40.865	39.135
Localized $\mathrm{LI_{GS}}(\mathcal{F})$	11.982	8.095	11.981	13.292	11.981	14.044	11.981	15.840
Intra-delocalized $\mathrm{DI_{GS}}(\mathcal{F},\mathcal{F})$	27.024	4.430	26.942	7.059	26.879	14.212	26.858	20.395
Inter-delocalized $\mathrm{DI_{GS}^{\mathcal{F}}}(\mathcal{F},\mathcal{F}_X)$	1.903	2.566	1.915	2.810	1.999	2.885	2.027	2.900
$\mathrm{DI_{GS}}(\mathcal{F}_1,\mathcal{F}_2)$	4.469		4.725		4.884		4.927	

© University of Pretoria

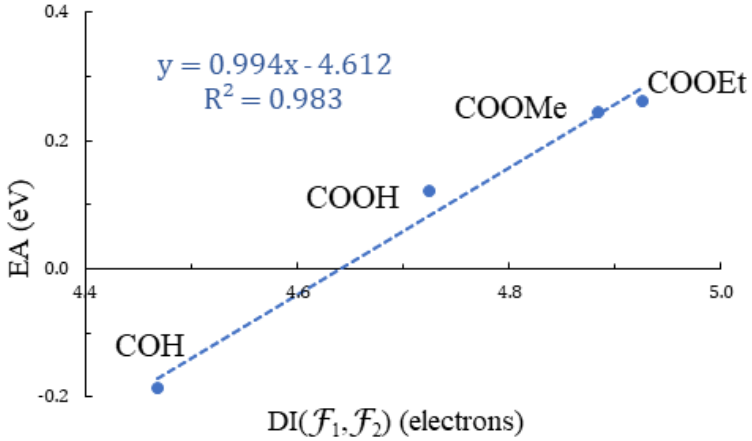

Figure S4.1. EA vs interfragment *deloc*–ED for the ground state of Ph-COX

Table S4.4. Electron population per fragment for Ph-OR molecules in ground state

Fragment	Ph-OH		Ph-OMe		Ph-OEt	
	Phenyl-	**-OH**	**Phenyl-**	**-OMe**	**Phenyl-**	**-OEt**
Total $N(\mathcal{F})$	40.457	9.543	40.468	17.532	40.470	25.530
Localized $LI_{GS}(\mathcal{F})$	11.977	5.648	11.974	6.539	11.973	8.374
Intra-delocalized $DI_{GS}(\mathcal{F},\mathcal{F})$	27.056	1.149	26.762	7.893	26.703	14.048
Inter-delocalized $DI_{GS}^{\mathcal{F}}(\mathcal{F},\mathcal{F}_X)$	1.424	2.746	1.732	3.100	1.794	3.107
$DI_{GS}(\mathcal{F}_1,\mathcal{F}_2)$	4.169		4.832		4.901	

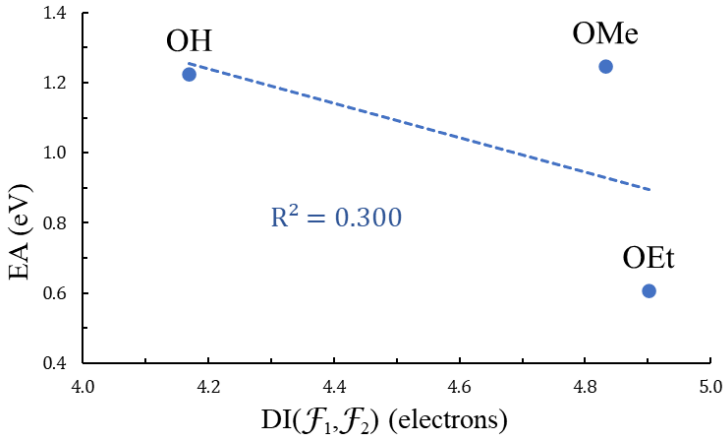

Figure S4.2. EA vs interfragment *deloc*–ED for the ground state of Ph-OR

© University of Pretoria

Chapter 5 SI

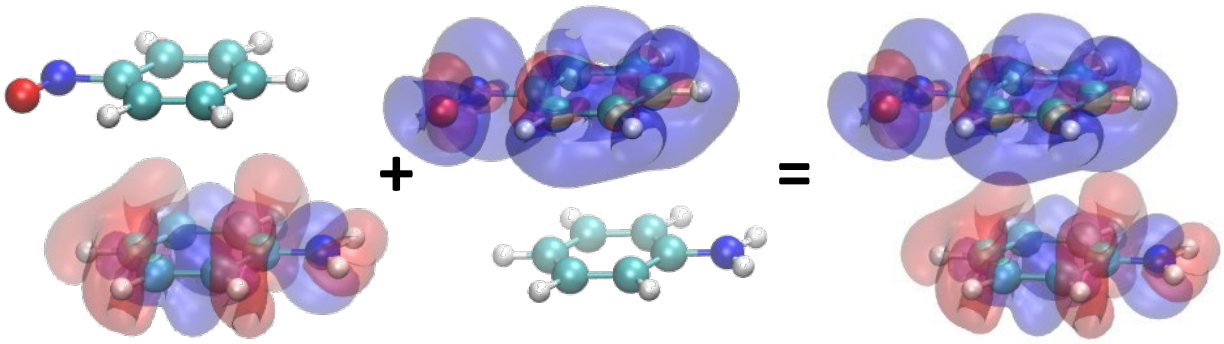

Figure S5.1. Justification for visualizing DI(D) change and DI(A) change in the same isosurface.

Clearly there is no (or very little) interference between the acceptor and donor's isosurfaces when combined in the same isosurface. For the figures where LI(D) change and LI(A) change is visualized on the same isosurface it is the same case.

Excitation information of interfaces

[NH_2-NO]

Ph-NH_2 individually:

Excited State 1: Singlet-A 4.4505 eV 278.58 nm f=0.0501 <S**2>=0.000

24 -> 32 0.18407

25 -> 28 0.27352

25 -> 29 0.61674

[NH_2-NO] ES corresponding to Ph-NH_2 ES1:

Excited State 3: Singlet-?Sym 4.3457 eV 285.30 nm f=0.0398 <S**2>=0.000

51 -> 54 -0.13205

51 -> 65 -0.13115

53 -> 56 0.52415

53 -> 60 -0.37182

© University of Pretoria

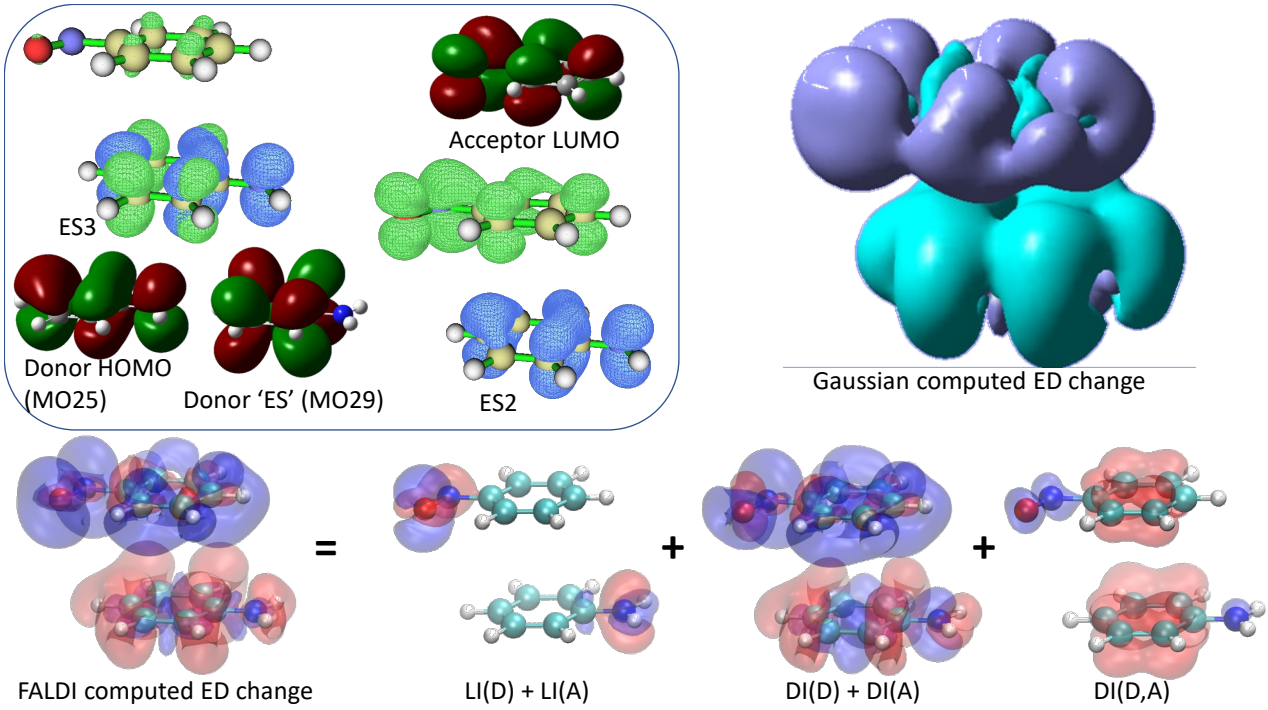

Figure S5.2. Summary of [NH_2-NO] isosurfaces. For isovalues see Chapter 5.

[NH_2-C_2H_4NO]

Ph-NH_2 individually:

Excited State 1: Singlet-A 4.4505 eV 278.58 nm f=0.0501 <S**2>=0.000

24 -> 32 0.18407

25 -> 28 0.27352

25 -> 29 0.61674

[NH_2-NO] ES corresponding to Ph-NH_2 ES1:

Excited State 2: Singlet-?Sym 4.3461 eV 285.28 nm f=0.0312 <S**2>=0.000

61 -> 62 0.13968

61 -> 64 0.34355

61 -> 65 0.34238

61 -> 66 0.30422

61 -> 67 0.14242

61 -> 71 0.22180

61 -> 73 0.11499

© University of Pretoria

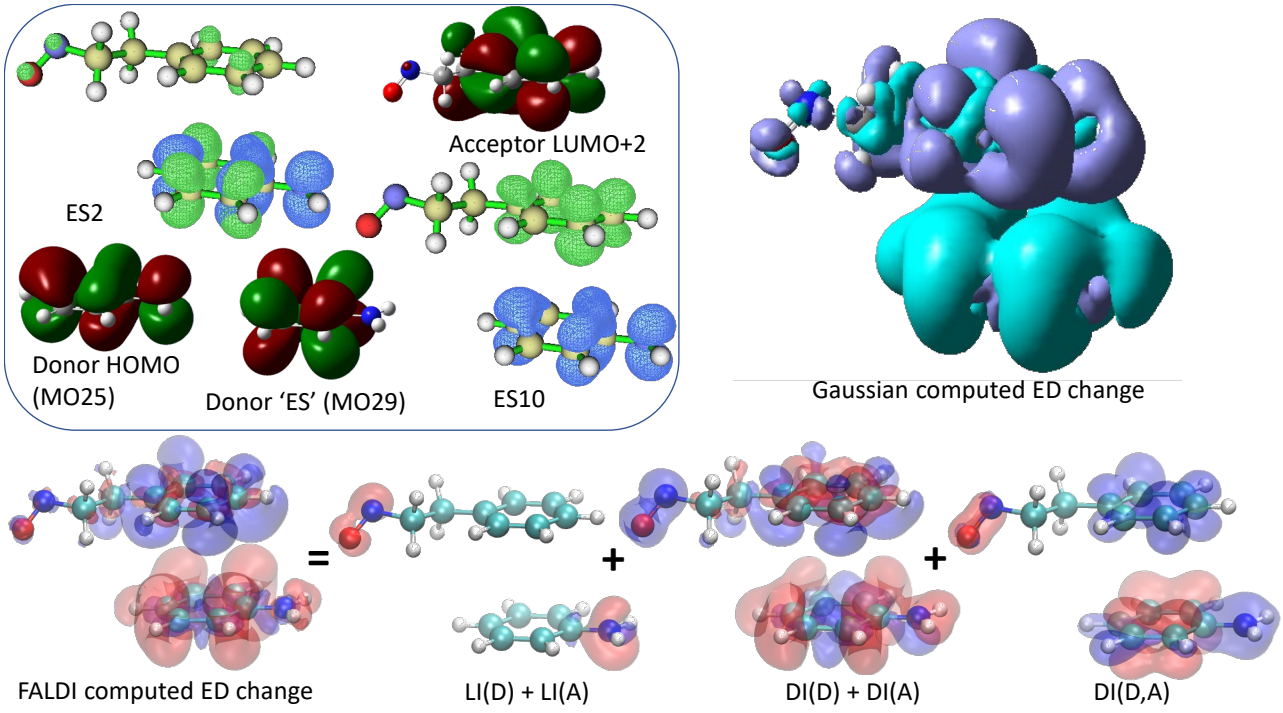

Figure S5.3. Summary of [NH_2-C_2H_4NO] isosurfaces.

[NPr_2-NO]

Ph-NPr_2 individually:

Excited State 1: Singlet-A 4.2636 eV 290.80 nm f=0.0479 <S**2>=0.000

49 -> 54 -0.66396

[NPr_2-NO] ES corresponding to Ph-NPr_2 ES1:

Excited State 3: Singlet-?Sym 4.1738 eV 297.05 nm f=0.0307 <S**2>=0.000

77 -> 80 0.38312

77 -> 81 -0.36837

77 -> 85 -0.13211

77 -> 86 -0.17271

77 -> 87 -0.16174

77 -> 88 -0.19857

77 -> 89 0.23536

© University of Pretoria

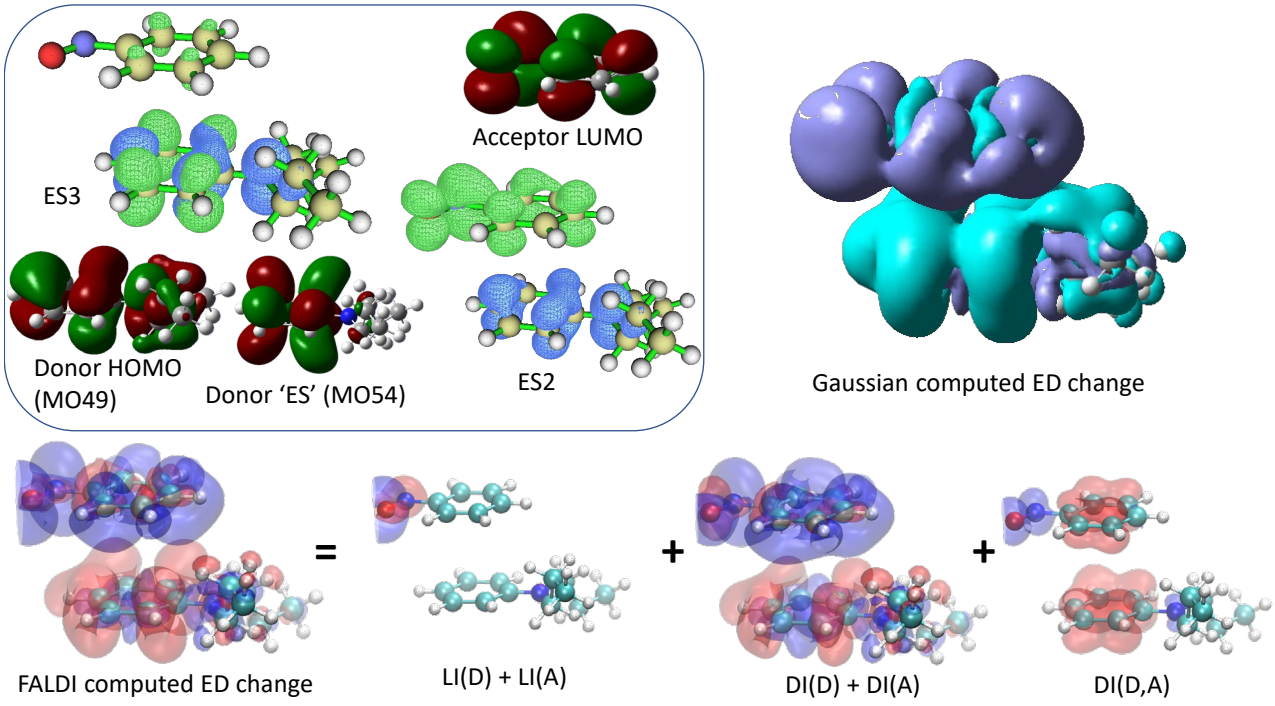

Figure S5.4. Summary of [NPr_2-NO] isosurfaces.

[NPr_2-C_2H_4NO]

Ph-NPr_2 individually:

Excited State 1: Singlet-A 4.2636 eV 290.80 nm f=0.0479 <S**2>=0.000

49 -> 54 -0.66396

[NPr_2-C_2H_4NO] ES corresponding to Ph-NPr_2 ES1:

Excited State 2: Singlet-?Sym 4.1626 eV 297.85 nm f=0.0228 <S**2>=0.000

85 -> 86 -0.34703

85 -> 90 -0.32270

85 -> 91 0.37621

85 -> 92 0.16149

85 -> 96 0.12120

85 -> 98 -0.15185

85 -> 99 -0.16540

© University of Pretoria

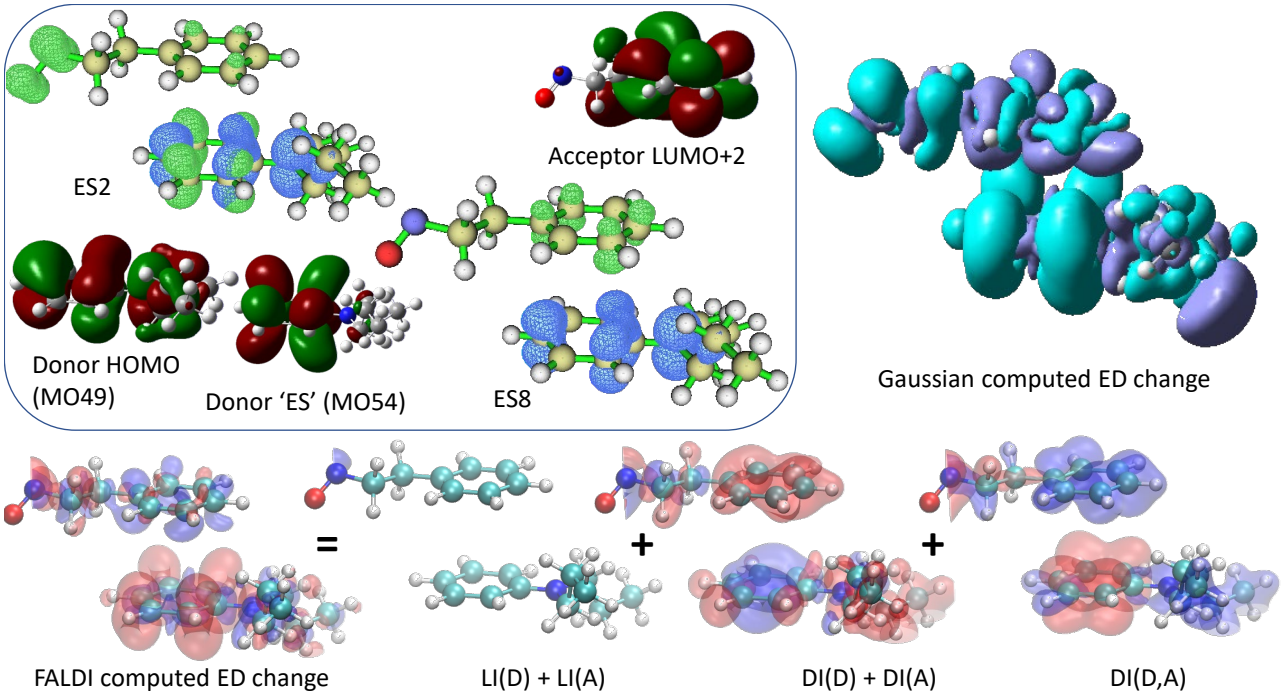

Figure S5.5. Summary of [NPr_2-C_2H_4NO] isosurfaces.

© University of Pretoria